A MULTI-TRANSITION

CO STUDY OF

THE GL 490 OUTFLOW

Siow Wang Lee

A thesis submitted in partial fulfillment of the
requirements for the degree of
Master of Science

Saint Mary's University
Halifax, Nova Scotia
December 1992

Canada

TABLE OF CONTENTS

I. Introduction

II. Observations and Data Reductions

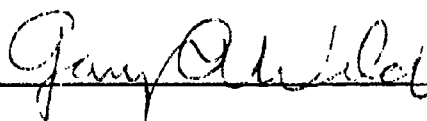## III. Results

The Examining Committee

David G. Turner

Dr. D. G. Turner

Professor and Chairperson of Astronomy

Saint Mary's University

Gary A. Welch

Dr. G. A. Welch

Associate Professor of Astronomy

Saint Mary's University

George F. Mitchell

Dr. G. F. Mitchell

(Thesis Supervisor)

Professor of Astronomy

Saint Mary's University

Acknowledgements

I would like to thank Dr. George Mitchell for introducing me to the subject of star formation. His influence is the sole reason for me to continue working in this area of astronomy when I continue my graduate studies. In addition, I thank him for giving me a chance to experience observing on Mauna Kea, Hawaii. It was a unique and unforgettable trip.

I would also like to thank Dr. Gary Welch for his patience in teaching, he is one of the best professors I have known. Thanks also to Dr. David Turner, for his diligence in lecturing and for what I considered encouragement-in-disguise! To Cameron and Laurie Reed, many thanks for their hospitality as well as the interesting discussions over lunch of such widely differing subjects. A very special thanks goes to Dr. Randall Brooks, for all his help, support and humor. I will never forget the Christmas dinners that he and Diane invited David and me to, it made spending the festive season so far from home that much easier. I am also indebted to Dr. Hasegawa for useful discussion on the subject of temperature distribution.

My appreciation to all the students I have met and gotten to know over the three years in St. Mary's, especially to Virginia MacSwain and her family for introducing me to Eastern Canadians Culture. To Jason Schella, what an interesting character he is, I am glad to have met him. Lifang Ma, thanks for being a good roommate and so tolerant, I wish her and her husband the very best in their future. To my friends and family in Singapore, their letters and phone calls expressing their love and support kept me going when the going got tough.

Finally, to my husband David, obtaining this degree would not be possible without his love, help and encouragement. At times when doubt, fear or depression sets in, he was always there for me. Thanks for believing in me.

List of Figures

List of Tables

ABSTRACT

The high-velocity GL 490 outflow has been observed at high spatial resolution with the JCMT in three rotational transitions (J = 2→1 of HBBW = 21", J = 3→2 of HPBW = 15" and J = 6→5) of ^{12}CO and ^{13}CO. A number of moving clumps can be detected in the channel maps, which indicates that the outflow is bipolarity but complex in structure. The main red wing emission from GL 490 consists of two spatially separate clumps of similar mass. The estimated masses of the clumps are found to be higher (from 0.01 to 0.5 solar mass) than those of previously studied clumps from other outflows.

The moving clumps velocities exceed the estimated escape velocity of the parent molecular cloud. Total clump mass is 0.3% of the cloud mass confined within a radius of 0.4 pc and 15% of the total outflow mass. Therefore, the clumps represent a kinematically insignificant component of the molecular cloud.

The detection of CO J = 6→5 emission shows that warm rest velocity gas exists near GL 490. This warm region is estimated to be about 6000 AU in radius, assuming spherical geometry. Combined with infrared absorption spectroscopy data, the average density of this region is estimated to be ~10^6 cm^{-3}.

The ^{12}CO J = 6 → 5 spectral line map shows that line profiles changes markedly within 20" of GL 490. A strong blue wing emission is seen at the position of the main blue lobe. The line profile displays no emission from the rest velocity gas at this location. This fact, coupled with the derived high temperature and density, is consistent with shocked CO in the blue lobe.

I. Introduction

(A) Current Theory of Star Formation

Stars are born out of molecular gas. Giant Molecular Clouds (GMC's) are some of the largest single complexes observed in the Galaxy, having dimensions up to ~100 pc, masses 10^4 to 10^5 $M_\odot$ and average densities of about 50 cm^{-3} (Blitz and Thaddeus, 1980). These interstellar nurseries contain, as the name implies, mostly molecular materials with molecular hydrogen as their major constituent. Observations of carbon monoxide (CO) emission indicate that these cloud complexes contain clumps of masses ~ 10^3 - 10^4 $M_\odot$, sizes a few pc and temperatures about 10 K (e.g., Blitz and Thaddeus, 1980). Within the clumps are more localized subcondensations called 'cloud cores' which have been mapped with high density tracers like carbon monosulfide (CS) (Linke and Goldsmith, 1980) and ammonia (NH$_3$) (Ho and Townes, 1983). These cloud cores have typical sizes of about 0.1 pc, masses up to a few solar masses and densities greater than 10^4 cm^{-3}. Low mass star formation is thought to occur within these cloud cores.

Cosmic ray events maintain a low level of ionization in the cloud cores, permitting the process of ambipolar diffusion to occur in which neutrals slip past ions along magnetic field lines. An important result is that the magnetic field lines diffuse outward and the core becomes increasingly centrally concentrated. When magnetic support of a core decreases sufficiently, it will collapse dynamically. A protostar will begin to form at the centre of the core accompanied by the infalling envelope around it. This process is believed to form low mass stars. Predominantly low to moderate mass star formation is probably occurring by this mechanism in the Taurus-Auriga complex (e.g., Myers and Benson, 1983 and Fuller and Myers, 1987) and the Ophiuchus complex (e.g., Grasdalen et al., 1973 and Lada and

Wilking, 1984). If the clump mass is greater than a critical mass, which is the mass above which dynamical collapse will be initiated, even with magnetic support taken into consideration the clump will rapidly contract to form relatively high mass stars. An example of a high mass star formation region is the Orion complex (e.g., Genzel and Stutzki, 1989).

(B) OBSERVATIONAL CHARACTERISTICS OF YSOs

Since young stellar objects (YSOs) are located in the densest parts of molecular clouds, it is not surprising that most have no optical counterparts. They are usually observed to be very compact sources in the near- and mid-infrared and may have a surrounding dust shell several thousand astronomical units in dimension. Multiple systems within a molecular cloud are sometimes observed as distinct intensity peaks embedded within the cloud core. Presumably these intensity peaks form an association or a cluster like that seen in the Orion Molecular Cloud (OMC).

The spectra of these objects show strong absorption bands at 9.7 and 3.08 μm which are attributed to silicates and water ices respectively. Other absorption features are seen at 4.6, 6.0, and 6.8 μm, but their identification is still uncertain.

Near-IR polarization is substantial in many YSOs, and two possible mechanisms are thought to be responsible for it. Preferential extinction due to aligned grains may arise from the action of a magnetic field in the cloud causing nonspherical grains to align their major axes perpendicular to the field; alternatively, the polarization may be due to scattering by grains which are located in flattened clouds or biconical nebulae in the vicinity of the YSO.

Many YSOs show lines of the Paschen, Brackett, and Pfund series of hydrogen in emission and/or weak radio continuum emission. Extended wings indicating velocities $\gtrsim$ 1000 km s^{-1} are observed in the Brackett lines, suggesting that the emitting gas is being blown away. The intensity of the lines is best explained by an ionized stellar wind, with mass loss rates estimated to be on the order of 10^{-6} to 10^{-7} $M_{\odot}$/yr (e.g. Simon et al., 1981b).

Water and/or hydroxyl maser sources are often observed around luminous embedded objects, which may indicate that the very dense and compact maser knots are being accelerated to high velocities in a strong stellar wind. The masers often consist of individual spots with diameters of about 10^{14} to 10^{15} cm forming groups that have typical sizes of the order of 10^{16} cm ($\sim$ 1000 AU). Other types of masers such as SiO and CH_3OH have been observed, but these are very rare due to the restrictive range of conditions needed to produce them.

According to Wilking and Lada (1983) and Lada and Wilking (1984), the spectral appearance of these objects can be divided into three classes on the basis of their 1 to 20 micron energy distribution (Fig. 1). Class I young stellar objects shows broad IR emission that does not fall off towards long wavelengths, and hence there are huge IR excesses. This class is considered to contain the youngest protostars, and the large IR excesses are believed to be caused by the infalling envelopes. Class II YSOs show flat or slightly decreasing emission towards long wavelengths. Sources in this class are thought to be at the "T Tauri stage" of evolution, with IR excesses due to emission from the associated accretion disk. Class III YSOs have essentially a blackbody-type energy distribution with little or no IR excess. Objects in this class are presumably pre-main-sequence stars that are about to started their main-sequence life as hydrogen-core-burning stars or have just done so. The fact that the spectra are close to blackbody distributions indicates that somehow
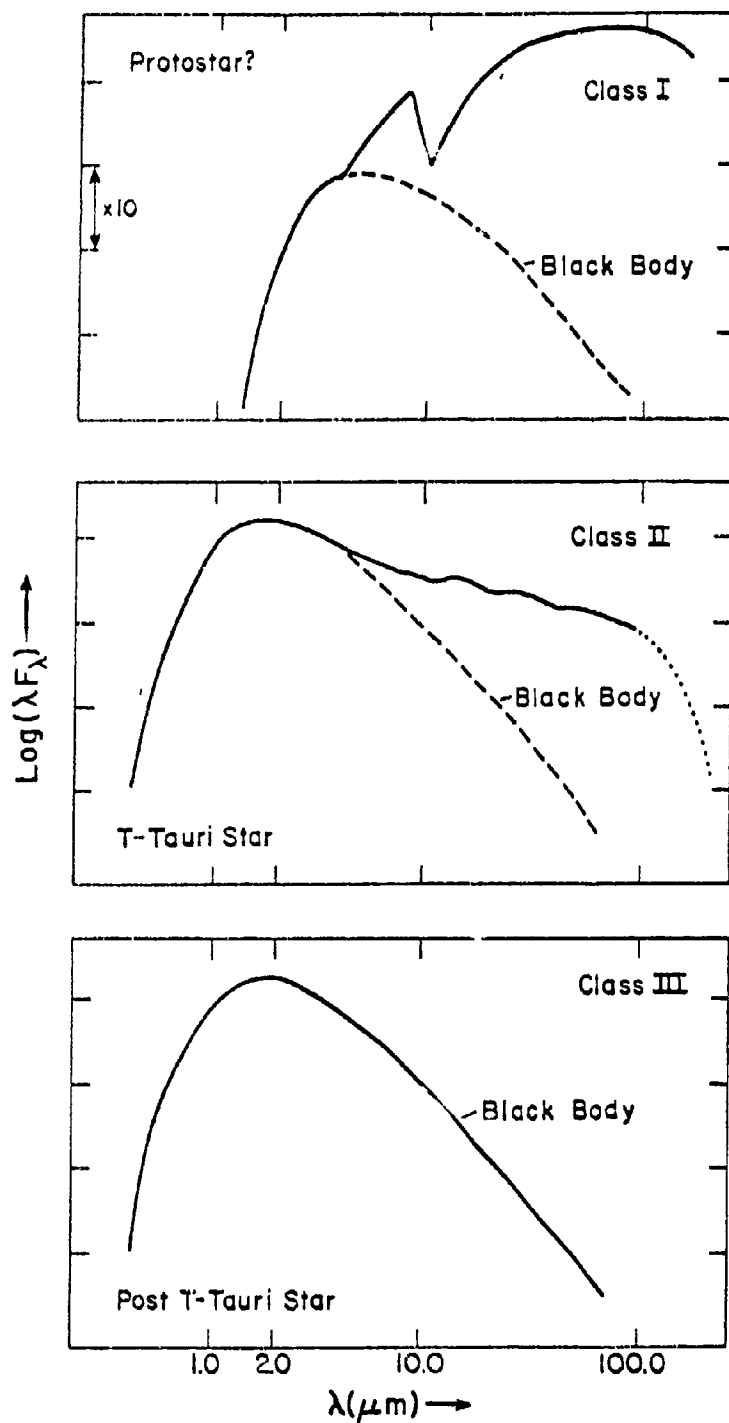
Fig. 1   Energy distributions of the three proposed classes of embedded young stellar objects. Class I objects have positive spectral indices longward of 2 microns wavelength. Class II objects have characteristics of T Tauri stars where slopes are flat or negative longward of 2 microns. Class III distributions are fit well by reddened blackbody curves, these objects represent stars near or on the ZAMS. (From Lada, 1985a)

the stars have shed most of their circumstellar material during the early stages of evolution. In this classification scheme, a YSO is thought to be evolving from a class I object to a class III object by accreting some percentage of the cloud core material and dissipating the rest as it evolves toward the main-sequence.

(C) MOLECULAR OUTFLOWS

After the detection of high-velocity CO in the core of the Orion A molecular cloud by Zuckerman et al.(1976), high-velocity molecular gas has been detected toward many young stellar objects. CO lines towards embedded IR sources can display velocity widths of over 100 km s^{-1} (full width at zero intensity). CO emission are usually found to be highly localized (< 1'). Figure 2 shows a ^{12}CO spectrum of Orion A, where line wings out to $V_{LSR} = \pm 60$ km s^{-1} at an antenna temperature of 100 mK can be seen. Since the sound speed in cold (10 °K) molecular clouds is only a few tenths of a kilometre per second, these observed gas flows are necessarily hypersonic in nature. The morphology of this phenomenon is often bipolar, with blue- and red-shifted emission lying on opposite sides of the central source. Figure 3 shows maps of seven high-velocity molecular flow sources. Some flows show highly collimated lobes while the majority exhibit only moderate collimation.

Lada and Harvey (1981), in a discussion on the nature of the high-velocity flow found in the vicinity of the infrared source GL 490, examined whether rotation, collapse, or expansion can be the cause of the high-velocity flow. They argued that spherically symmetric expansion or collapse can be ruled out by the distinct bipolarity of the flow. Rotation and anisotropic collapse are not feasible because the central mass required to explain the high velocities observed in the line profile is too large. Therefore, they concluded that non-spherically symmetric expansion of the molecular gas is the best
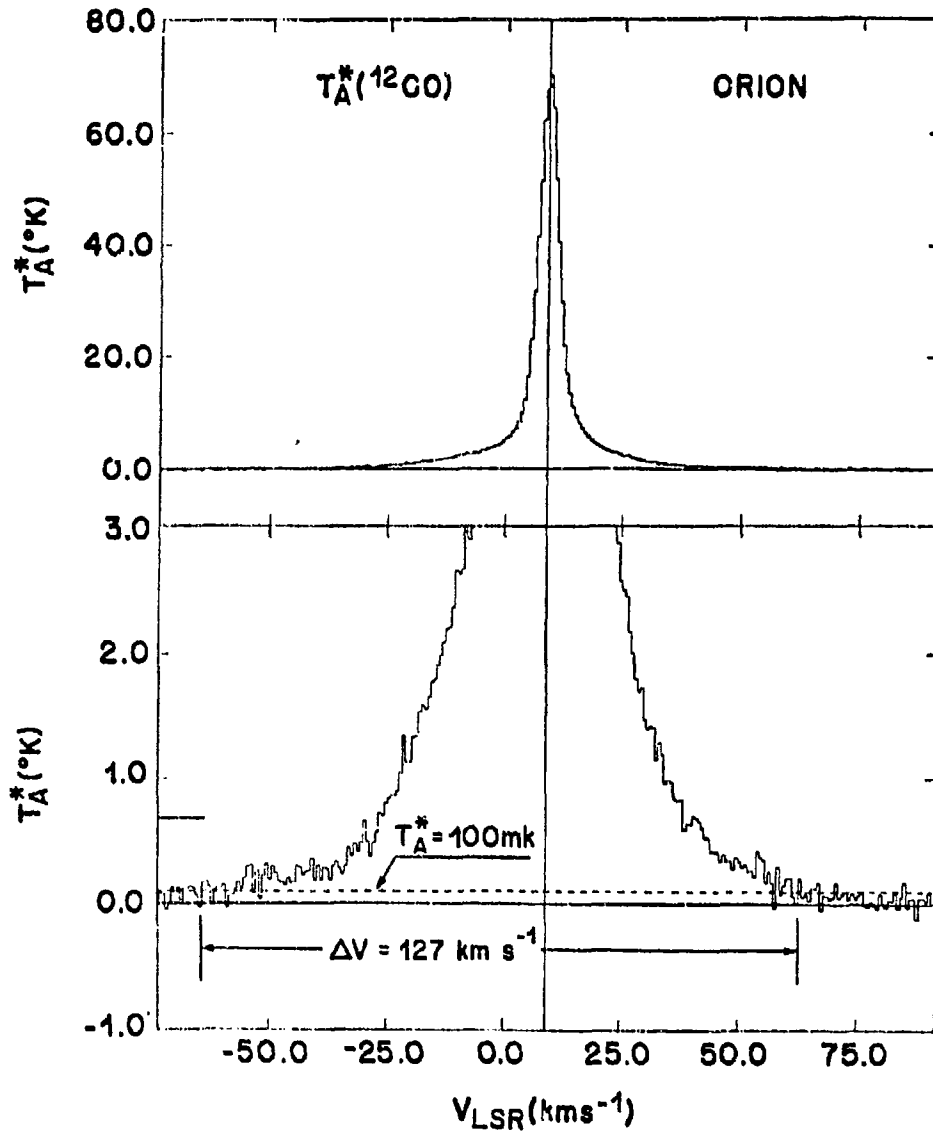
Fig. 2 ^{12}CO spectrum of Orion A. The lower panel covers the same velocity range as the upper panel but has an expanded temperature scale. The dashed line indicates the $T_A^* = 100$ mK level. (From Bally and Lada, 1983.)
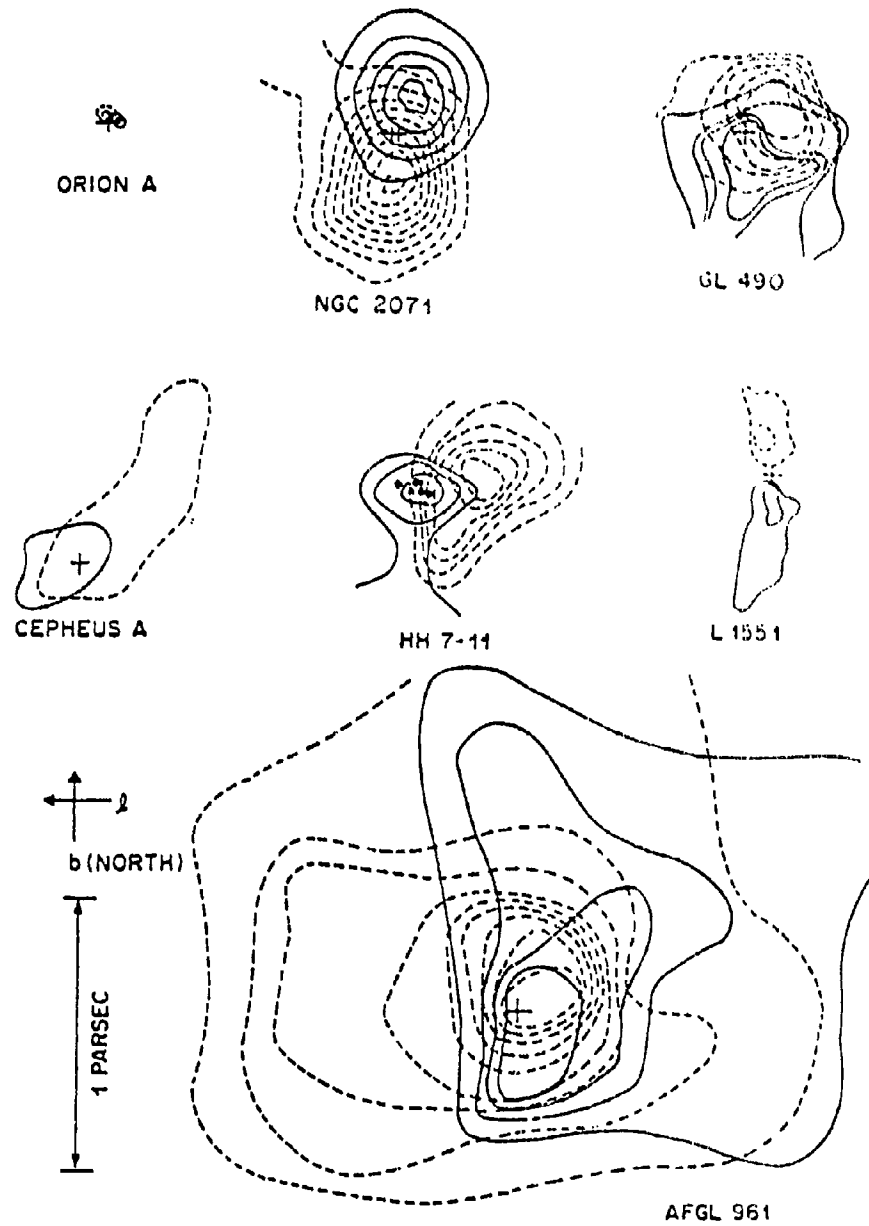
Fig. 3   Maps of seven high-velocity molecular outflow sources in molecular cloud cores taken from Bally and Lada (1983). Solid lines are blueshifted wings, and dashed lines are the redshifted wings. Most outflows shown here are only moderately collimated. All maps are of the same scale.

explanation for the data obtained. This argument seems to be equally valid for most of the other high-velocity flows observed (Lada, 1985b). Hence, the phenomenon that was first detected in the Orion A molecular cloud is now widely accepted as 'Bipolar Molecular Outflow".

Lada (1985b) compiled a list of 67 high-velocity molecular flow sources from the literature and discussed, amongst other things, the energetics of the outflows. In his review article, two plots were displayed in order to delineate any relationship between the driving sources and the outflows. Flow mechanical luminosity, L_{HMF} (i.e., the energy supply rate), and average force required to drive the outflow, $\dot{P}$ (i.e., the momentum supply rate), are plotted against stellar luminosity, L_* (Figs. 4 and 5) (note that the subscript HMF refers to High-Velocity Molecular Flow). As can be seen, there appears to be a weak but nonetheless apparent correlation in the two diagrams in that the higher the luminosity of the infrared source, the larger the flow energy supply rate and the greater the force required to drive the flow. These correlations suggest that it is probably a good assumption that the embedded central object is the driving source of a molecular outflow, and that the mechanism that causes these outflows may be similar for all sources.

The two dashed straight lines representing the relations $L_{HMF} = L_*$ and $\dot{P} = L_*/c$, where c is the speed of light, are also plotted in Figures 4 and 5. The observation that all sources lie in the region $L_{HMF} < L_*$ indicates that the embedded sources are energetically capable of driving the outflows. However, Figure 5 shows that all sources lie in the region $\dot{P} > L_*/c$, indicating that radiation pressure cannot be the driving mechanism.

Shu et al. (1991) presented a model in which a protostar is accreting material from the flattened molecular cloud core, forming a thin rotating equatorial disk. A wind will
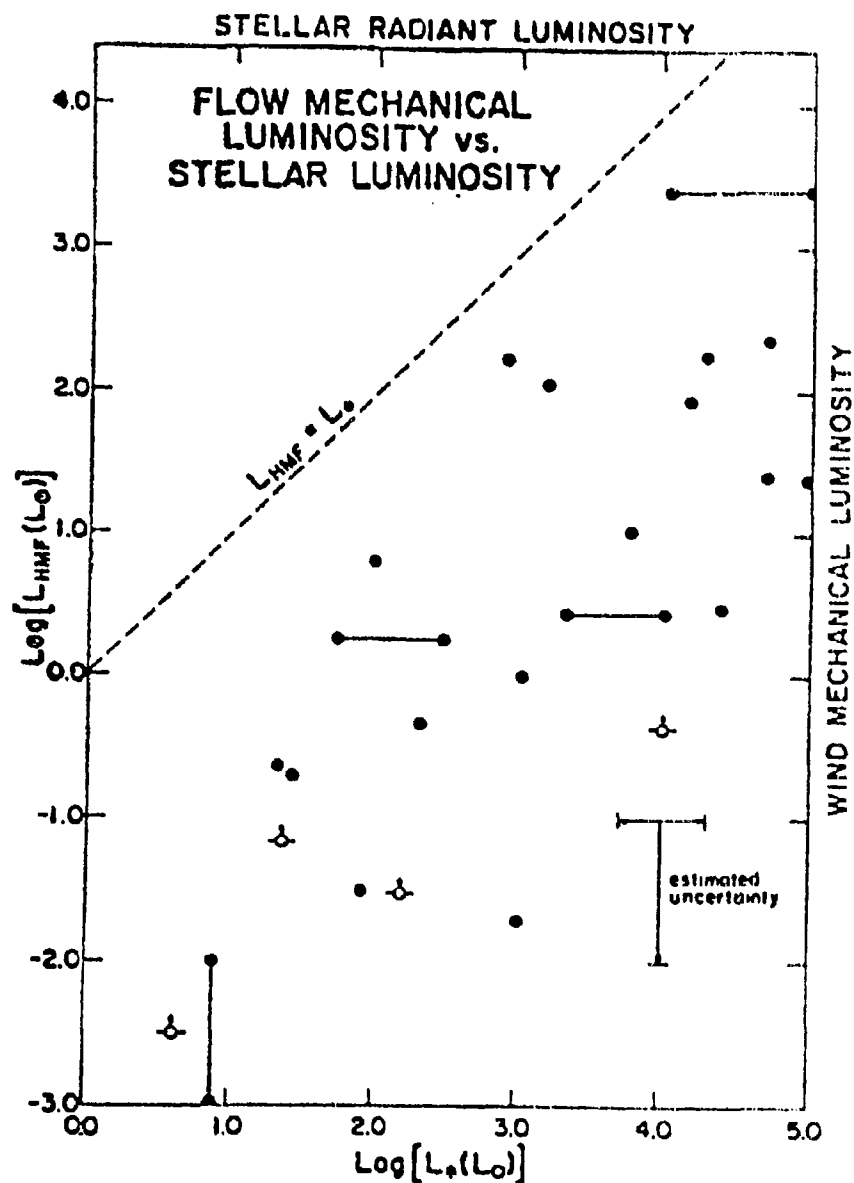
Fig. 4   Mechanical luminosity of high-velocity molecular outflows plotted against the total radiant luminosity of embedded central objects. All sources fall below the relation $L_{HMF} = L_*$. Horizontal and vertical line segments indicate the estimated uncertainties in the determinations of L_{HMF} AND L_*. (From Lada, 1985b.)
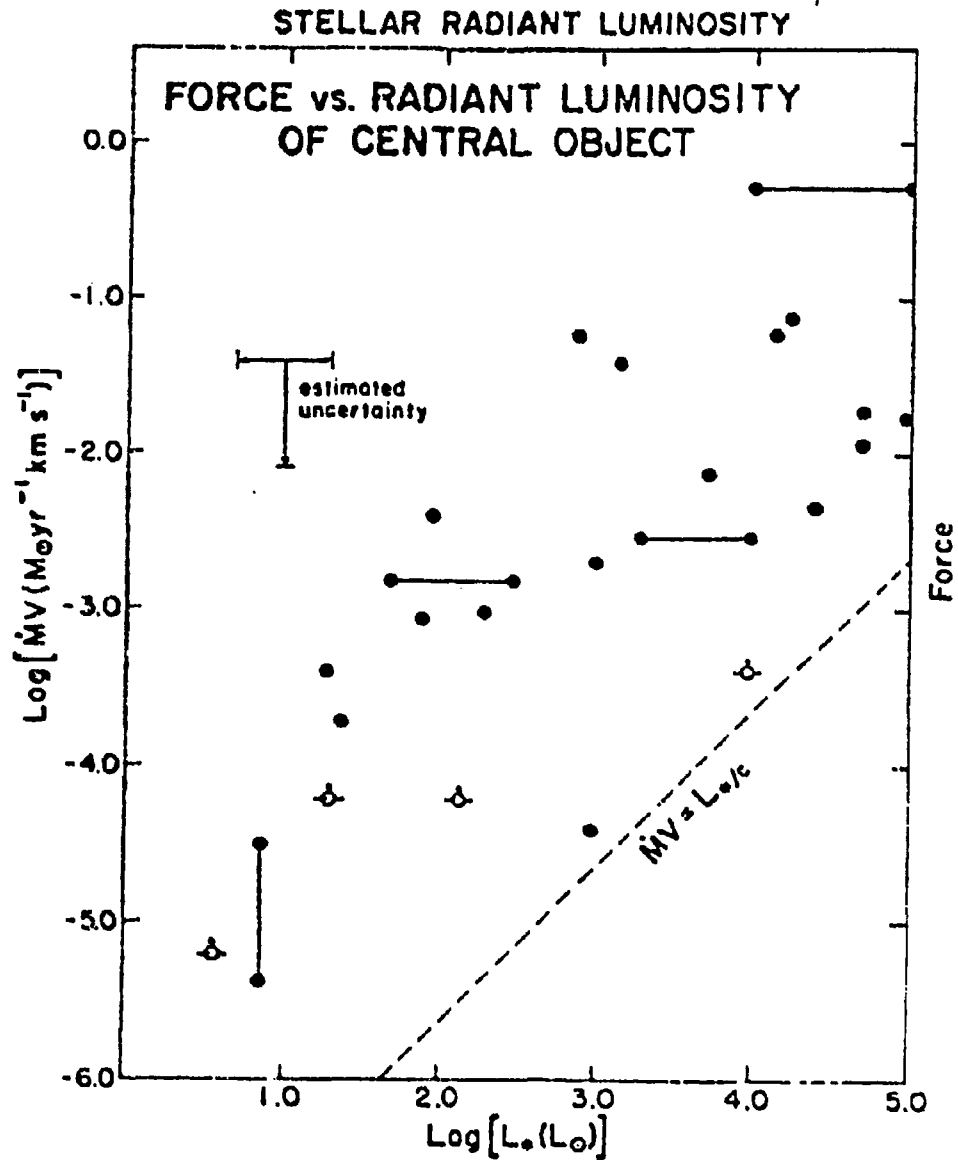
Fig. 5   Average force required to drive the molecular outflows plotted against the total radiant luminosity of the embedded central objects. All sources fall above the

relation $MV = L_*/c$, which suggests that radiation pressure from the central objects is not sufficient to drive the flows. (From Lada, 1985b.)

eventually break out at the poles due to accretion of rapidly rotating material by the protostar. This wind moves into the ambient cloud (with density distribution ∞ 1/r³), sweeping up a shell of molecular material in a momentum conserving interaction. A shock driven into the ambient cloud sets the gas in motion. They found that the molecular shell speed $v_s \propto (av_w)^{1/2}$, where a is the sound speed of the cloud core and v_w is the velocity of the wind. For values of v_w typically a few hundreds of km s^{-1} and a sound speed typically about 1 km s^{-1}, the velocity of the shell is about a few tens of km s^{-1}. This velocity width has been observed in some outflows, e.g., L1551-IRS5, Mon R2 and GL 490 (Bally and Lada, 1983). However, this model cannot explain extremely high velocity outflows like Orion A, which has a full width at 100 mK of 127 km s^{-1} (Bally and Lada, 1983), or NGC 7538 IRS 9, where the CO lines have a full width of 150 km s^{-1} (Mitchell and Hasegawa, 1991). Shu et al. (1991) also predicted that, at a given time, the expansion velocity is highest at points furthest from the source. While some outflows do show this trend, there are many more which display the opposite. That is, the highest velocity moving gas is seen closest to the source.

Draine (1983) proposed a "magnetic bubble" model to explain the origin of the high-velocity outflows in molecular clouds. In his model, a high-mass, slowly rotating, pre-main-sequence star has strong coupling between core and envelope. This causes the star to be in uniform rotation at all times. A magnetic field threading through the protostar has flux lines frozen into the protostar (due to ionized material in its interior). Because the protostar is rotating, it will begin to wind up the magnetic field, producing a twisted magnetic field in the vicinity of the protostar. The magnetic pressure will increase rapidly, driving a shock wave into the ambient cloud and producing an expanding shell of compressed molecular gas. The required magnetic field strength in this model is consistent with what is known about magnetic fields of early-type stars. One of the advantages in using this model is that the shedding of angular momentum by a protostar is a natural

consequence of the coupling of the protostar with its surrounding molecular cloud through magnetic field lines. In explaining the bipolarity of outflows observed, Draine utilized the mechanism proposed by Königl (1982). Königl suggested that there is a tendency for gas to flow along magnetic field lines. Therefore, gas in the vicinity of the protostar will tend to form an enhanced density region along the field lines. In Draine's model, therefore, a pressure-driven disturbance like a magnetic-bubble will tend to expand most rapidly in the orthogonal direction, i.e., in the direction of the magnetic field. The model is successful in explaining the observed high-velocity flow in OMC-1. The bubble's expansion velocity is of the order required to explain the shock speed inferred from the observed line emission from that region. However, the magnetic bubble model seems to work best for more energetic outflows rather than for low-velocity outflows.

Pudritz and Norman (1983) proposed a magneto-hydrodynamic disk wind model. The basic idea is that a massive, rapidly rotating and relatively large, magnetized circumstellar disk centrifugally drives the energetic mass outflow. A flux of ultraviolet photons arising from the accretion shock and is absorbed by the accretion disk surface layers, heating it to form a disk envelope. In the presence of an ionizing protostellar region, Pudritz and Norman find that magnetic flux and ions slowly drift outwards, along the rotational axis, due to ambipolar diffusion. This outward drift becomes more rapid further away from the disk. On encountering the disk envelope, this flux slams into the envelope gas, heating and/or accelerating the gas and thereby feeding the centrifugal drive. One of the advantages of this model is that the outflow properties derived are insensitive to the infrared luminosity of the central source. Therefore the model is able to explain outflows from low to high mass protostars. Also, the disk wind can carry off disk angular momentum, solving the angular momentum problem in star formation.

(D)   CARBON MONOXIDE AS A PROBE OF MOLECULAR CLOUDS

Phenomena pertaining to star formation are difficult to observe. This is because, according to theory, protostars, which are stars not yet burning hydrogen fuel in their centres, are objects in the process of accumulating material from their parent molecular clouds in which they are embedded. The thick gas and dust shells that engulf them extend for several thousand astronomical units causing these young stars to be invisible. However, because these dust shells absorb radiation falling on them and re-emit at infrared wavelengths, it is possible to observe these young stellar objects in wavelengths longer than the visible. In the 1970s, millimetre and submillimetre observations became important probes of the dense regions of molecular clouds. Many molecules that exist in these regions emit at millimetre and submillimetre wavelengths via rotational transitions. These molecules, with assumed abundances relative to hydrogen, i.e., $n(X)/N(H_2)$, can be used to obtain physical properties of the gas, thereby providing useful information on the environment in regions of star formation.

Carbon monoxide (CO) is the most abundant cloud molecule after molecular hydrogen (H_2). It is about an order of magnitude more abundant than the next most abundant species, and is the most commonly used tracer for H_2. In addition, CO is relatively easy to excite with its lowest rotational excitation energy just 5.5 K above ground level and a critical density for excitation $\leq 10^4$ cm^{-3}. Hence, CO can be seen even in very cold molecular clouds (~10 °K). However, there are some drawbacks in using CO, so that other molecules may be more useful for observing under certain conditions. These drawbacks include: CO lines are often saturated in molecular clouds, thereby preventing information on excitation temperature and column densities to be extracted. In this case, other isotopes may be used, such as ^{13}CO, $^{12}C^{18}O$ or $^{13}C^{18}O$. Also, it is difficult to excite CO to higher rotational states in order to probe high density gas. Even if the high-lying

rotational states can be excited, they are very difficult to observe with ground-based equipment because of their high frequencies. Hence, molecules with high critical density must be used (e.g., CS and NH_3) to probe very dense regions.

(E)   AFGL 490

AFGL 490 (or GL 490), located at $\alpha(1950.0) = 03^h23^m38^s.8$, $\delta(1950.0) = 58°36'39"$ (l = 142°, b = 2°), is catalogued in the AFCRL (Air Force-Cambridge Research Laboratories) Infrared Sky Survey (Walker & Price, 1975). This was the first IR all-sky survey accomplished by rocket-borne systems operating at 11 and 20 μm. GL 490 has been well-observed from optical to radio wavelengths. It is believed to be a young stellar object deeply embedded in a dust cloud and evolving towards the main-sequence.

GL 490 is identified with a starlike object on the Palomar sky survey plates, and the surrounding fields are heavily obscured by dust (Cohen, 1975). CCD optical images (Campbell et al., 1986) show that the optical centroid is displaced by about 1".5 to the southwest of the centre of the 2 cm radio continuum emission map taken at the VLA. Campbell et al. suggest that the radio centre is the true source position and the optical image is due entirely to the scattered light from the obscured source.

In the near infrared, ice and silicate absorption features at 3.1 and 10 μm, respectively, are observed, which indicate that the object is embedded in a dense dust cloud. Brγ (Simon et al., 1981a) is found to have broad emission line wings with velocity at full-width-half-intensity of ~150 kms^{-1}. Assuming that the wings are due to gravitationally unbound ionized mass flow, Simon et al. estimate a mass loss rate greater than 3×10^{-7} $M_\odot$ yr^{-1} for GL 490. They note that such a large mass loss rate is similiar to what is found for O and B supergiants, but far exceeds that of main-sequence stars.

Infrared polarization measurements by Hodapp (1984) show a polarization angle of 115° and a degree of polarization in the K band of 6.6%. This angle is almost perpendicular to the observed axis of bipolar outflow from GL 490, as expected if the light is scattered off the bipolar outflow gas. Minchin et al. (1991) confirm the existence of a disc around GL 490 using the fact that the region of low percentage polarization is orthogonal to the outflow direction and parallel to the disc structure seen in CS and NH_3 emission.

Based on the HCN radial velocity measurement of Morris et al. (1974) and the Schmidt galactic rotation model, Harvey et al. (1979) estimated a distance of 900 pc to GL 490. The observed infrared fluxes from 50-200 μm found by Harvey et al. therefore implied an integrated luminosity of ~ 1.4×10^3 $L_\odot$, which corresponds to a zero-age-main-sequence B3 star. Snell et al. (1984), however, pointed out that this distance estimate is very uncertain. They obtained a kinematic distance of 1.0 ± 0.5 kpc assuming a flat galactic rotation curve and a 6 km/s random motion for molecular clouds with diameters greater than 20 pc. Thus, the luminosity derived by Harvey et al. could be uncertain by a factor of at least 3. In the far infrared, the luminosity of GL 490 derived using the IRAS Point Source Catalog and a distance of 900 pc is 2200 $L_\odot$ (Mozurkewich et al., 1986). This value is in good agreement with that found by Harvey et al. (1979). In passing, we note that a better estimate of the distance of GL 490 has been previously found to be 870 ± 40 pc based on photometric and spectroscopic observations of the members of the R association in the vicinity of GL 490 (Racine, 1968).

Mitchell et al. (1988, 1991b) observed GL 490 in the M-band using high resolution IR spectroscopy. They detected absorption in the ^{12}CO fundamental vibrational band v = 1 - 0 at two velocity components, one of which is blueshifted by 13 km s^{-1} relative to GL 490. They suggest that this component is a recently ejected shell and that the extended

outflow results from a series of outburst from the central object. The fact that a 13 km s^{-1} velocity component is not observed in CO emission spectra despite its high column density led them to the conclusion that the absorbing gas must be very close to GL 490.

VLA observations at 6 cm indicated an upper limit of about 1 mJy (Simon et al., 1981a), which in turn leads to a maximum radius for an ionized core of about 40 AU. Simon et al. suggest that this source may have developed an ionized core which is still too compact to be detectable at radio wavelengths.

In the millimetre and submillimetre regime, HCN and CS were detected by Morris et al. (1974), indicating the presence of dense molecular gas around GL 490. Lada and Harvey (1981) found, using a 66" half-power beamwidth, high velocity wings in both ^{12}CO and ^{13}CO emission spectra, and estimated the flow mass and kinetic energy to be about 30 $M_\odot$ and 2×10^{47} ergs, respectively. They also found that the centres of the blue- and red-shifted components are separated spatially by 67", corresponding to 0.29 pc at a distance of 900 pc. This is an indication of the bipolarity of the outflow. Snell et al., however, found, using a 48" half-power beamwidth, a 30" separation between the red and blue emission peaks.

Plambeck et al. (1983) observed GL 490 in CO J = 2→1 and J = 1→0, and indirectly inferred the existence of high density clumps in the molecular outflow. This inference is based on the fact that J = 2→1 data indicated optically thick lines; in order to account for the low CO antenna temperatures observed in the line wings, the filling factor of the high-velocity gas must be small (f < 1).

An elongated structure of CS emission was found around GL 490 by Kawabe et al. (1984). This CS disk of dimensions 0.3×0.13 pc is oriented perpendicular to the direction

of the CO bipolar outflow, and is parallel to the angle of polarization. This is consistent with the picture that the dense outflow gas emerges from the poles of the disk.

Nakamura et al. (1991) used aperture synthesis of the CS $J = 2 \rightarrow 1$ transition, and found dense gas in a disk structure which has a non-circular velocity of ~ 1.5 km s^{-1}. They attributed this motion to mass infall. They estimated the torque required in order for the gas to lose angular momentum and spiral inward, and suggested that magnetic torque could be a candidate.

In this thesis we present high spatial resolution observations of GL 490 in various CO lines. Our purpose is to probe the physical environment around GL 490. The observations confirm the clumpy nature of the GL 490 bipolar outflow inferred indirectly by Plambeck et al. (1983). The detection of the CO $J = 6 \rightarrow 5$ line suggests that warm gas (100 °K) exists in the outflow. Additional IR absorption data indicate both warm and cold components in the rest velocity gas. The present data appear to support the scenario of a wind accelerating a shell of ambient gas near GL 490.

II Observations and Data Reduction

(A) OBSERVATIONS

All line emission spectra from the GL 490 region were obtained with the 15 m James Clerk Maxwell telescope on Mauna Kea, Hawaii. Observations of ^{12}CO J = 2 → 1 and ^{13}CO J = 2 → 1 were carried out by G. F. Mitchell and T. I. Hasegawa in 1989 August. Results of the J = 2 → 1 observations have been published (Mitchell et al. 1992). The ^{12}CO J = 3 → 2 spectra were obtained by G. F. Mitchell and S. W. Lee in August 1991. The ^{13}CO J = 3 → 2 spectra were obtained by G. F. Mitchell in December 1991. The ^{12}CO J = 6 → 5 emission data were obtained by G. F. Mitchell in December 1991 with the technical assistance of A. Harris and A. Russell of the Max-Planck Institute. The J = 6 → 5 data were obtained using receiver G (described below) which is on loan to the JCMT from the group at the Institut für Extraterrestrische Physik in Garching under the direction of Reinhard Genzel.

For the 2 → 1 transition at 230 GHz, the "common-user" receiver A1 was used. Receiver A1 employs a dual-channel Schottky mixer system which uses two mixers that nominally cover the frequency interval 220 - 280 GHz. The acousto-optical spectrometer (AOSC) provided a total bandwidth of 650 km s^{-1} at 230 GHz. The half-power beamwidth (HPBW) at this frequency was 21$^{"}$. The beam efficiency was 0.71, with about 10% uncertainty.

For the 3 → 2 transition at 345 GHz, the "common-user" receiver B2 was used. The AOSC provides a bandwidth equivalent to 435 km s^{-1} at 345 GHz. The half-power beamwidth was 15$^{"}$ and the beam efficiency was 0.55. The observed intensity for the two lower transitions is in the form of antenna temperature T_A^*, which is antenna temperature

corrected for atmospheric and telescope losses and sideband imbalance. The accuracy of the conversion to antenna temperature is estimated to be better than 15%. Observations of CO J = 2 → 1 and J = 3 → 2 were done in a position switching mode in which the telescope is alternatively switched between the source and a nearby reference position.

For the 6 → 5 transition, receiver G was used operating at 690 GHz. This receiver is a high-frequency heterodyne system using liquid nitrogen cooled Schottky mixers. It has its own spectrometer which has a bandwidth of 1100 MHz, equivalent to 470 km s^{-1} at 690 GHz. The telescope beam was well represented by a composite of a diffraction limited beam of 7" FWHM and a pedestal of 30" FWHM.

^{12}CO J = 2 → 1 observations consist of a 9 × 9 map on a 20" grid (see Fig. 6) and an inner 3 × 3 map on a 10" grid. ^{13}CO J = 2 → 1 was only observed at the position of the IR source. ^{12}CO J = 3 → 2 maps were obtained for 106 positions, some 10" apart and others 20" apart (Figs. 7, 8). ^{13}CO J = 3 → 2 maps were obtained for 30 positions on a 10" grid (Fig. 9). ^{12}CO J = 6 → 5 data (Fig. 10) were obtained for 10 positions with 10" spacing. Table 1 contains a list of all the observed positions. In Table 1 and subsequently, positions are given as (ΔRA,ΔDec.) in arcseconds from GL 490 [pointing centre was R.A.(1950) = 03^{h}23^{m}39^{s}21, decl. (1950) = 58°36'35".60]. East and North are positive. The data reduction was carried out using the SPECX package. Only linear baselines were removed from the spectra.

This thesis also makes use of a new high resolution infrared absorption spectrum in the M-band (4.7 µm), obtained by G. F. Mitchell and J.-P. Maillard in October 1991 using the Fourier Transform Spectrometer on the Canada France Hawaii Telescope on Mauna Kea, Hawaii. The spectrum covers the interval from 2080 to 2180 cm^{-1}, thus encompassing the fundamental band lines of ^{12}CO and ^{13}CO. The velocity resolution was
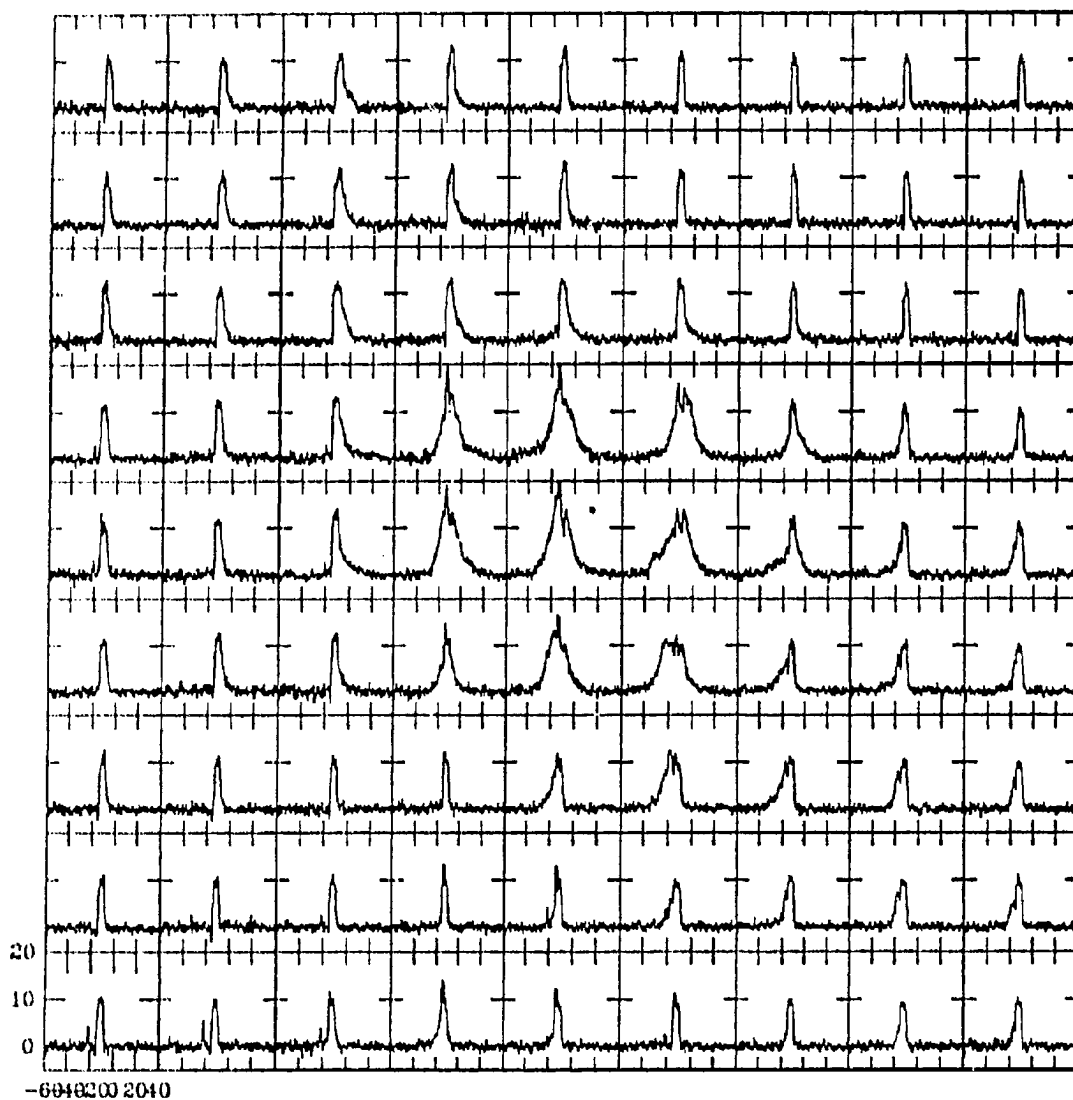
Fig. 6   A ^{12}CO J = 2 → 1 spectral line map centred on GL 490 (R.A. = $3^h23^m39^s21$, decl. = $58°36'35''60$). Each square represents the ^{12}CO J = 2 → 1 spectral line at that position (antenna temperature vs. V_{LSR}). In a given square each division on the x-axis is 20 km s^{-1} while each division on the y-axis is 10 °K. North is at the top and East is to the left. This map uses 20" grid spacing.
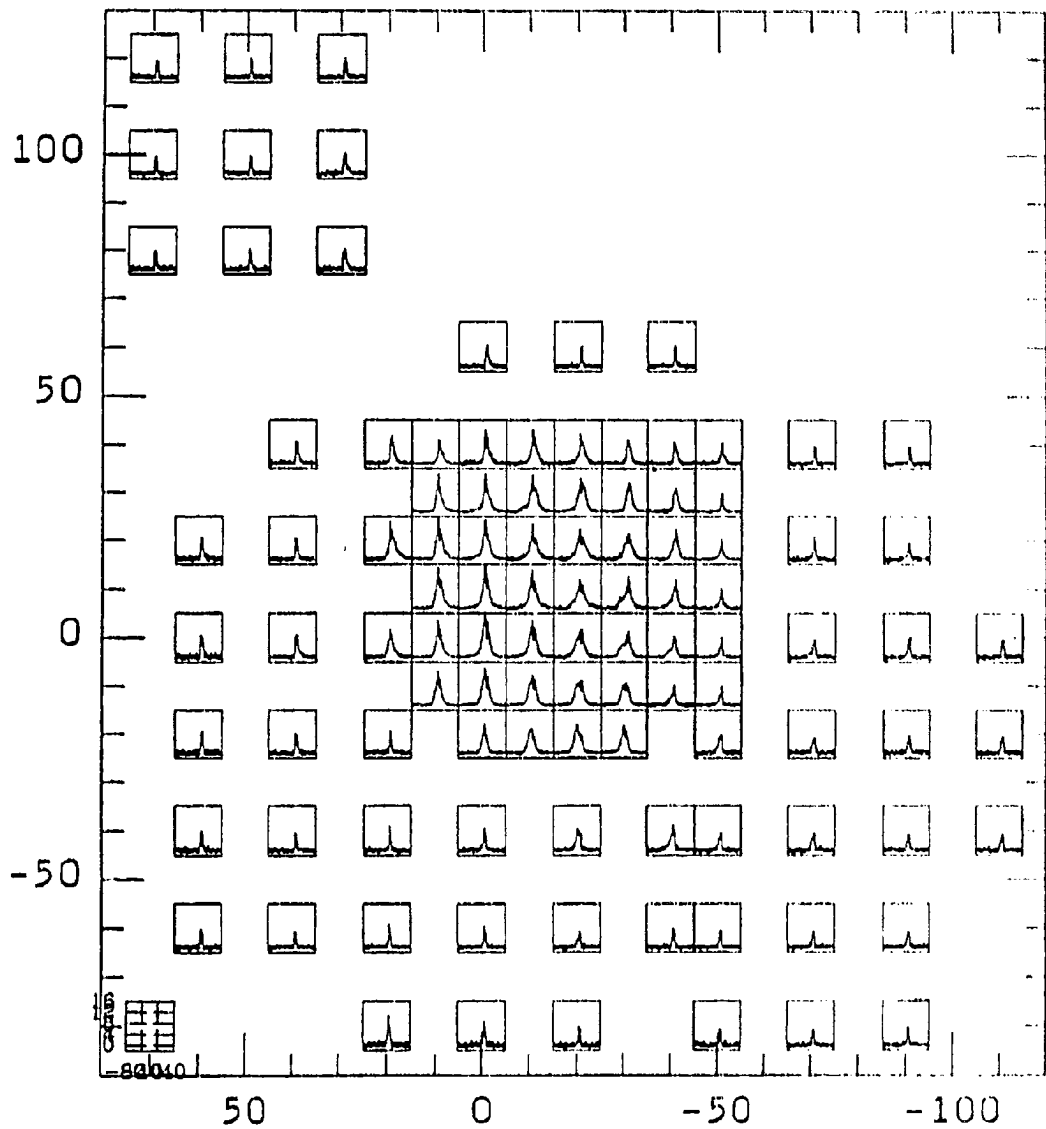
Fig. 7   The ^{12}CO J = 3 → 2 spectral line map centred on GL 490. Each square represents the ^{12}CO J = 3 → 2 spectrum at that position. Broad line wings are observed for the inner region. Inner grids are 10" apart while outer grids are 20" apart.
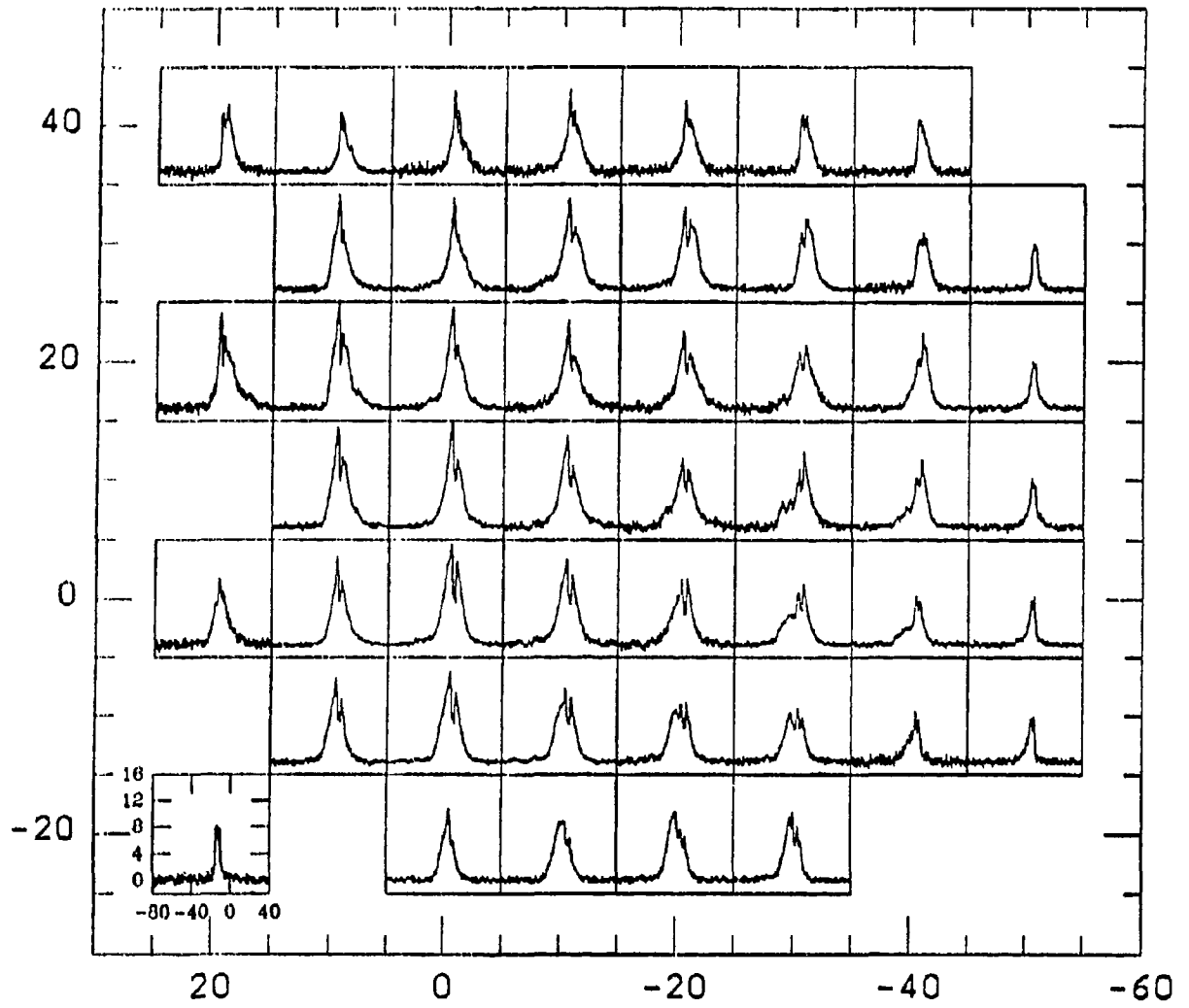
Fig. 8   As in Figure 7, but only the central 50" by 40" from GL 490. Grids are 10" apart.
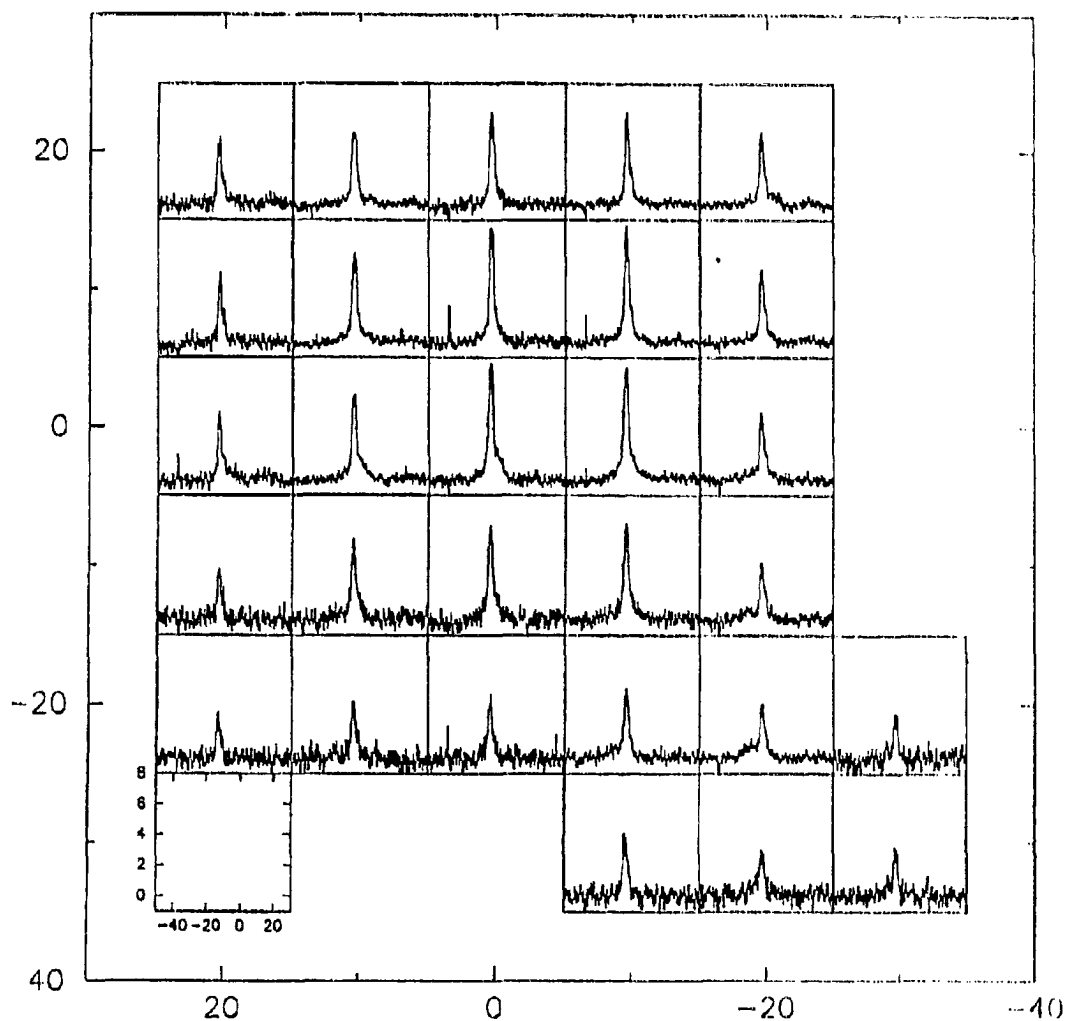
Fig. 9   A ^{13}CO J = 3 → 2 spectral line map centred on GL 490. Grid spacing is 10". In a given square each division on the x-axis is 20 km s^{-1} while each division on the y-axis is 2 °K. A spectrum at position (-30,0) was also obtained, but is not shown in this map.
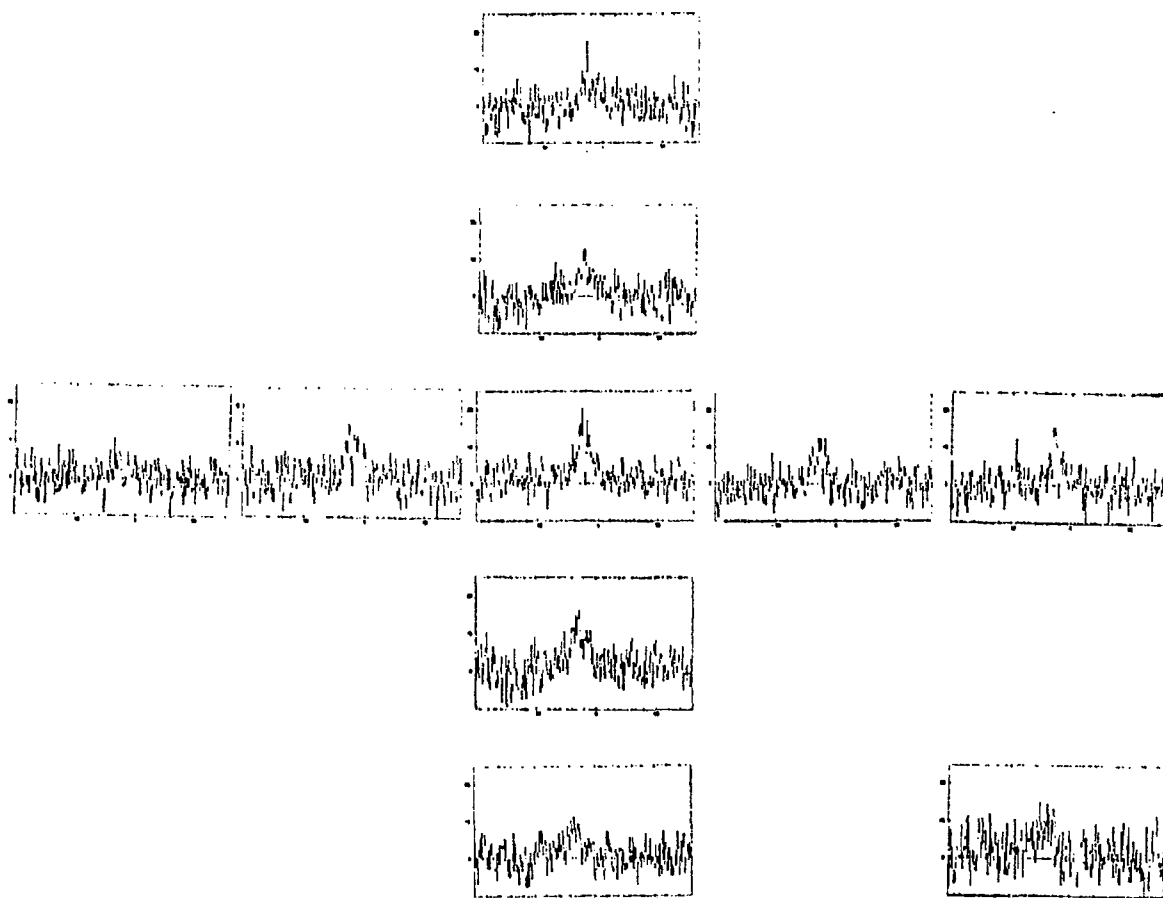
Fig. 10   A ^{12}CO J = 6 → 5 spectral line map centred on GL 490. Each spectrum in the cross is 10" apart and (-20,-20) is at the lower right hand corner of the map. North is at the top and East is to the left.

6.9 km s^{-1}. Data reduction for the infrared absorption spectroscopy was done by G. F. Mitchell and is briefly outlined in § II(B)(b).

TABLE 1

LIST OF OBSERVATIONS

^{12}CO J = 2 → 1	81 positions, 20" spacing 3 × 3 map, 10" spacing
^{13}CO J = 2 → 1	(0,0) only
^{12}CO J = 3 → 2	106 positions, 10" and 20" spacing
^{13}CO J = 3 → 2	5 × 5 map, 10" spacing (-30,0), (-30,-20), (-30,-30), (-20,-30), (-10,-30)
^{12}CO J = 6 → 5	(20,0), (10,0), (0,0), (-10,0), (-20,0), (0,20), (0,10), (0, -10), (0,-20), (-20,-20)

(B) DERIVATION OF PHYSICAL PROPERTIES

(a) CO Millimetre/Submillimetre Emission Lines

The mass contained in high-velocity gas is one of the most important physical parameters for understanding the nature of molecular outflows. It is possible to obtain the gas mass from observations of two isotopic forms. The procedure for obtaining masses is shown in detail below. Optical depths and column densities are calculated for every step (km/s) in the velocity scale of the spectrum and integrals are obtained by summing over the full velocity intervals.

Optical depths can be obtained from the ratio of radiation temperatures for the two isotopes ^{12}CO and ^{13}CO. This is done by using the relation between the radiation temperature, T_R, and the optical depth, τ_v, together with the assumption that both species have the same excitation temperature, T_{ex}. Radiation temperature is defined by

$$I_v \, dv = \frac{2v^2}{c^2} k \, T_R \, dv \, , \tag{1}$$

where I_v is the observed intensity of the source at frequency v,

c is the speed of light,

and k is the Boltzmann constant.

The solution of the transfer equation in a uniform medium is

$$I_v = (1 - e^{-\tau v}) \, B_v(T_{ex}) \, , \tag{2}$$

where τ_v is the optical depth at frequency v and $B_v(T_{ex})$ is the Planck function at the excitation temperature T_{ex} as given by

$$B_\nu(T_{ex}) = \frac{2h\nu^3}{c^2}\left[\exp\left(\frac{h\nu}{kT_{ex}}\right) - 1\right]^{-1}. \tag{3}$$

Equating (1) and (2) and substituting (3), we find

$$T_R = (1 - e^{-\tau_\nu})\frac{h\nu/k}{e^{h\nu/kT_{ex}} - 1}. \tag{4}$$

The radiation temperature is related to the observed antenna temperature by

$$T_R = \frac{T_A^*}{\eta_B f}, \tag{5}$$

where T_A^* is the antenna temperature corrected for atmospheric and telescope losses,

η_B is the beam efficiency which takes the side-lobe losses of the telescope beam

into account

and   f, the beam filling factor, is the fraction of the beam filled by the source.

Substituting equation (5) into equation (4) yields

$$\frac{T_A^*}{\eta_B f} = (1 - e^{-\tau_\nu})\frac{h\nu/k}{e^{h\nu/kT_{ex}} - 1}. \tag{6}$$

Assuming the excitation temperature of each species to be constant, we can apply equation (6) to each of two species, e.g., $^{12}CO\ J = 3 \rightarrow 2$ and $^{13}CO\ J = 3 \rightarrow 2$. If we ignore the small difference in emitting frequencies of the two species, ratioing gives

$$\frac{T_R^{12}}{T_R^{13}} = \frac{T_A^{*12}}{T_A^{*13}} \approx \frac{1-e^{-\tau^{12}}}{1-e^{-\tau^{13}}}, \tag{7}$$

in which Γ (which is unknown) and η_B are eliminated.

If we can further assume an abundance ratio for the two isotopes of $\dfrac{N^{12}}{N^{13}} \approx 60$ (Langer and Penzias, 1990), then

$$\frac{\tau^{12}}{\tau^{13}} \approx 60, \qquad (8)$$

and τ^{12} and τ^{13} can be obtained by substituting equation (8) into equation (7).

The excitation temperature can be found as follows once the optical depth is known. The equation of radiative transfer for a plane-parallel cloud is

$$\begin{aligned}
\frac{dI_\nu}{dz} &= \varepsilon_\nu - \kappa_\nu I_\nu \\
&= \frac{h\nu}{4\pi}\, n_u A_{ul} - \frac{h\nu}{4\pi}\, I_\nu\,(n_u B_{ul} - n_l B_{lu}),
\end{aligned} \qquad (9)$$

where ε_ν and κ_ν are the emission and absorption coefficients, respectively,

n_u and n_l are number densities of the upper and lower level molecular populations, respectively,

$A_{ul} = \dfrac{64\pi^4 \nu^3}{3hc^3}\,\mu^2\,\dfrac{u}{g_u}$ is the rate of spontaneous deexcitation, (10)

u and l are the rotational quantum number of the upper and lower state respectively,

μ is the electric dipole moment of the molecule,

g_u is the statistical weight of the upper level,

$B_{ul} I_\nu$ is the rate of stimulated emission,

and $B_{lu} I_\nu$ is the rate of absorption.

After substitution of the well-known relationships between the Einstein transition probabilities

$$A_{ul} = \frac{2h\nu^3}{c^2} B_{ul} \quad \text{and} \quad \frac{B_{ul}}{g_l} = \frac{B_{lu}}{g_u}, \tag{11}$$

the optical depth becomes

$$\tau_\nu = -\int_0^z \kappa_\nu \, dz$$

$$= -\int_0^z \left[\frac{h\nu}{4\pi} (n_u B_{ul} - n_l B_{lu}) \right] dz$$

$$= -\frac{h\nu}{4\pi} \int_0^z \left[n_u \left(\frac{c^2 A_{ul}}{2h\nu^3} \right) - n_l \left(\frac{g_u}{g_l} B_{ul} \right) \right] dz \qquad \text{using (11)}$$

$$= -\frac{c^2}{8\pi\nu^2} A_{ul} \int_0^z n_u \left(\frac{n_l g_u}{n_u g_l} - 1 \right) dz. \tag{12}$$

In local thermodynamic equilibrium (LTE), the Boltzmann equation is valid, hence

$$\frac{n_l g_u}{n_u g_l} = e^{h\nu/kT_{ex}}. \tag{13}$$

Equation (12) then becomes

$$\tau_\nu = \frac{c^2}{8\pi\nu^2} A_{ul} N_u(\nu) \left(e^{h\nu/kT_{ex}} - 1 \right), \tag{14}$$

where $N_u = n_u z$ = the column density of molecules in the upper level.

Using equation (13) again, equation (14) becomes

$$\tau_\nu = \frac{c^2}{8\pi\nu^2} A_{ul} \frac{g_u}{g_l} N_l(\nu) \left(1 - e^{-h\nu/kT_{ex}} \right). \tag{15}$$

With equation (10) and $g_u = 2u + 1$ (for linear molecules), we have

$$\tau_v = \frac{8\pi^3 v}{3hc} \mu^2 \frac{u}{2\ell+1} N_l(v) \left(1 - e^{-hv/kT_{ex}}\right). \tag{16}$$

Now, let the rotation quantum number of the upper state (u) be J_1 and J_2 for two different transitions of the same isotope. Their corresponding lower states are J_1-1 and J_2-1. The ratio of the optical depth of these two transitions yields the excitation temperature as follows. Using equation (15),

$$\frac{\tau_{J_1 \to J_1-1}(v)}{\tau_{J_2 \to J_2-1}(v)} = \left(\frac{v^2_{J_2 \to J_2-1}}{v^2_{J_1 \to J_1-1}}\right)\left(\frac{g_{J_1} g_{J_2-1}}{g_{J_1-1} g_{J_2}}\right)\left(\frac{A_{J_1 \to J_1-1}}{A_{J_2 \to J_2-1}}\right)\left(\frac{N_{J_1-1}}{N_{J_2-1}}\right)\left(\frac{1 - e^{hv_{J_1 \to J_1-1}/kT_{ex}}}{1 - e^{hv_{J_2 \to J_2-1}/kT_{ex}}}\right). \tag{17}$$

After substitution of $\frac{dv}{v} = \frac{dv}{v}$, equation (17) is applied to the $J = 3 \to 2$ and $J = 2 \to 1$ to obtain

$$\frac{\tau_{3 \to 2}}{\tau_{2 \to 1}} = \left(\frac{3}{2}\right)\left(\frac{1 - e^{hv_{3 \to 2}/kT_{ex}}}{e^{hv_{2 \to 1}/kT_{ex}} - 1}\right), \tag{18}$$

where $\tau_{3 \to 2} = \int \tau_{3 \to 2}(v)\, dv$.

From equations (7) and (8), $\tau_{3 \to 2}$ and $\tau_{2 \to 1}$ can be obtained and hence T_{ex} can be found using equation (18).

The column density can be calculated as follows:

Equation (15) gives the lower state column density in some frequency interval:

$$N_l(v)\, dv = \frac{8\pi v^2}{c^2} \frac{g_l}{g_u} \frac{1}{A_{ul}} \left(1 - e^{-hv/kT_{ex}}\right)^{-1} \tau_v\, dv. \tag{19}$$

It is often preferable to consider velocity intervals rather than frequency intervals. Therefore, using $\dfrac{dv}{v} = \dfrac{dv}{c}$,

$$N_{\ell} = \frac{8\pi v^2}{c^2} \frac{g_{\ell}}{g_u} \frac{1}{A_{u\ell}} \left(1 - e^{-h v/kT_{ex}}\right)^{-1} \int \tau_v \frac{v}{c} \, dv$$

$$= \frac{3h}{8\pi^3 B\mu^2} (\frac{2\ell+1}{u})\left(1 - e^{-hv/kT_{ex}}\right)^{-1} \int \tau_v \, dv. \qquad (20)$$

N_{ℓ} is the column density of molecules in rotational level ℓ integrated over some velocity interval. To find the total column density (i.e. taking all transitional levels into account), the Boltzmann equation has to be used:

$$\frac{N_{\ell}}{N_{tot}} = \frac{g_{\ell}}{U} e^{-E_{\ell}/kT_{ex}}. \qquad (21)$$

For a linear molecule, the partition function, U, is given to good approximation by the expression $\dfrac{k}{hB} (T_{ex} + \dfrac{hB}{3k})$; the energy of the lower state, E_{ℓ}, is equal to $hB\ell(\ell+1)$, and B is the rotational constant of the molecule in question.

Substituting U, E_{ℓ} and equation (20) into equation (21) yields

$$N_{tot} = \frac{3k}{8\pi^3 B\mu^2} \frac{1}{u} (T_{ex} + \frac{hB}{3k}) e^{hB\ell(\ell+1)/kT_{ex}} \left(1 - e^{-hv/kT_{ex}}\right)^{-1} \int \tau_v \, dv. \qquad (22)$$

where v is velocity in km s^{-1} and N_{tot} is in cm^{-2}. In the case of CO, B = 5.75×10^{10} Hz and $\mu = 1.1 \times 10^{-19}$ esu-cm.

For the ^{13}CO J = 3 $\rightarrow$ 2 transition, the total column density is:

$$N_{tot} = 0.80 \times 10^{14} \ (T_{ex} + 0.92) \ e^{16.55/T_{ex}} \ (1 - e^{-15.86/T_{ex}})^{-1} \int \tau_v^{13} \, dv. \tag{23}$$

For the ^{12}CO J = 6 $\rightarrow$ 5 transition, the total column density is:

$$N_{tot} = 4.00 \times 10^{13} \ (T_{ex} + 0.92) \ e^{82.88/T_{ex}} \ (1 - e^{-33.22/T_{ex}})^{-1} \int \tau_v^{12} \, dv. \tag{24}$$

Since the main constituent of the interstellar medium is molecular hydrogen, it is necessary to relate the column density of CO obtained above to the column density of H_2 in order to find the mass. Here, we have used the abundance ratios $\dfrac{N(^{12}CO)}{N(^{13}CO)} = 60$ and $\dfrac{N(^{12}CO)}{N(H_2)} = 1 \times 10^{-4}$ to obtain $\dfrac{N(^{13}CO)}{N(H_2)} = 1.7 \times 10^{-6}$. The relative abundance of ^{13}CO is actually uncertain, but the assumed ratio of 60 will probably not introduce uncertainties much greater than a factor of 2 in the determination of the mass in the high-velocity flow.

Finally, the mass may be found by multiplying the total column density by the assumed area of the clump, A , and the mass of a hydrogen molecule m_H, i.e.

$$M(H_2) = \left(N(H_2) \times [2 \times m_H] \times A \right) / 2 \times 10^{33} \quad \mathcal{M}_\odot. \tag{25}$$

As an example, we evaluate equation (25) for the mass in a single beam. At the distance of GL 490, which is assumed to be 1 kpc, and for a beam size of 15″ HPBW, we find

$$A = \pi r^2$$
$$= \pi \left(\frac{7.5}{206265} \times 10^3 \times 3.09 \times 10^{18} \right)^2$$
$$= 3.96 \times 10^{34} \ cm^2,$$

which yields $M(H_2) = 3.96 \times 10^{-17} \ N(^{13}CO) \ \mathcal{M}_\odot$ from (23). $\tag{26}$

If a distance of 870pc is assumed, then $M(H_2) = 9.58 \times 10^{-18} \, N(^{13}CO) \, \mathcal{M}_\odot$, a factor of 0.76 smaller then in equation (26).

To obtain the total mass of the clump, the fractional helium abundance (10% by number) must also be taken into account. That is

$$M = 1.4 \times M(H_2)$$

$$= 5.55 \times 10^{-17} \, N(^{13}CO) \quad \mathcal{M}_\odot. \tag{27}$$

Note that with the data obtained for this project, $\tau_{2\to1}$, needed for the evaluation of T_{ex} using equation (18), can only be obtained at (0,0) because the $^{13}CO \; J = 2 \to 1$ data are only available at this position. At other positions T_{ex} must be found by introducing an additional assumption, for example that the filling factor is unity.

In the two extreme cases, i.e. optically thin and optically thick gas, the column density can be calculated using the appropriate approximations.

Where $\tau \ll 1$ is applicable, equation (4) becomes

$$T_R = \tau \frac{h\nu/k}{e^{h\nu/kT_{ex}} - 1}, \tag{28}$$

using $e^{-\tau} = 1 - \tau + \frac{\tau^2}{2!} - \cdots$.

Together with equation (16), we find

$$T_R = \frac{8\pi^3\nu}{3hc} \mu^2 \frac{h\nu}{k} \frac{u}{2\ell + 1} N_\ell e^{-h\nu/kT_{ex}}.$$

For two transitions $J_1 \rightarrow J_1 - 1$ and $J_2 \rightarrow J_2 - 1$, the ratio gives

$$\frac{T_R(J_1 \rightarrow J_1-1)}{T_R(J_2 \rightarrow J_2-1)} = \left(\frac{\nu_{J_1 \rightarrow J_1-1}}{\nu_{J_2 \rightarrow J_2-1}}\right)\left(\frac{J_1}{J_2}\right)\left(\frac{2J_2-1}{2J_1-1}\right)\left(\frac{N_{J_1-1}}{N_{J_2-1}}\right)\left(\frac{e^{-h\nu_{J_1 \rightarrow J_1-1}/kT_{ex}}}{e^{-h\nu_{J_2 \rightarrow J_2-1}/kT_{ex}}}\right) \tag{29}$$

Using $h\nu_{J_1 \rightarrow J_2} = hB[J_1(J_1+1) - J_2(J_2+1)]$ and the Boltzmann equation, we have

$$\frac{T_R(J_1 \rightarrow J_1-1)}{T_R(J_2 \rightarrow J_2-1)} = \frac{J_1^2}{J_2^2}\left(e^{-hB[(J_1-1)J_1-(J_2-1)J_2]}\right)\left(\frac{e^{-2hBJ_1/kT_{ex}}}{e^{-2hBJ_2/kT_{ex}}}\right)$$

$$= \frac{J_1^2}{J_2^2}\exp\left[-\frac{hB}{kT_{ex}}[J_1(J_1+1) - J_2(J_2+1)]\right]$$

$$= \frac{J_1^2}{J_2^2}\exp\left[-\frac{2.76}{T_{ex}}[J_1(J_1+1) - J_2(J_2+1)]\right]. \tag{30}$$

From equation (5), T_R can be obtained observationally assuming the filling factor to be unity (to be justified later). Hence, assuming T_{ex} is the same for both transitions, the excitation temperature can be calculated from equation (30).

For the two transitions $J = 3 \rightarrow 2$ and $J = 2 \rightarrow 1$, equation (30) yields

$$\frac{T_R(3 \rightarrow 2)}{T_R(2 \rightarrow 1)} = \frac{9}{4}e^{-16.56/T_{ex}}, \tag{31}$$

and for $J = 6 \rightarrow 5$ and $J = 3 \rightarrow 2$, equation (30) gives

$$\frac{T_R(6 \to 5)}{T_R(3 \to 2)} = 4 e^{-82.80/T_{ex}}. \tag{32}$$

The column density in the optically thin approximation can be derived by substituting equation (16) into equation (28) to yield

$$T_R(v) = \frac{8\pi^3 v \mu^2}{3hc} \frac{hv}{k} \frac{u}{2l+1} N_l(v) e^{-hv/kT_{ex}}. \tag{33}$$

Rearranging, we have

$$N_l(v) \, dv = \frac{3hc}{8\pi^3 v \mu^2} \frac{k}{hv} \frac{2l+1}{u} e^{hv/kT_{ex}} T_R(v). \tag{34}$$

Using $\frac{dv}{v} = \frac{dv}{c}$, equation (34) then becomes

$$N_l = \frac{3k}{8\pi^3 v \mu^2} \frac{2l+1}{u} e^{hv/kT_{ex}} \int T_R(v) \, dv. \tag{35}$$

Using the Boltzmann equation (equation (21)) with the partition function $U \approx \frac{k}{hB} T_{ex}$ in equation (35) yields

$$N_{tot} = \frac{3k^2}{8\pi^3 hB v \mu^2} \frac{1}{u} T_{ex} e^{(u+1)hv/2kT_{ex}} \int T_R(v) \, dv. \tag{36}$$

For the transition $^{12}CO \; J = 3 \to 2$, equation (36) gives

$$N_{tot} = 4.81 \times 10^{12} \, T_{ex} \, e^{33.2/T_{ex}} \int T_R(v) \, dv, \tag{37}$$

and for the transition $^{12}CO \; J = 6 \to 5$, equation (36) gives

$$N_{tot} = 1.20 \times 10^{12} \, T_{ex} \, e^{116.3/T_{ex}} \int T_R(v) \, dv. \tag{38}$$

In the optically thick regime, $e^{-\tau^{12}} \approx 0$, so equation (4) becomes

$$T_R = \frac{hv/k}{e^{hv/kT_{ex}} - 1},$$ (39)

which yields T_{ex} directly.

Evaluating equation (39) for the $^{12}CO\ J = 3 \rightarrow 2$ transition,

$$T_R = \frac{16.59}{e^{16.59/T_{ex}} - 1}.$$ (40)

The column density can be obtained using equation (23) with the optical depth derived from equation (7). It should be noted, however, that the optical depth is poorly determined from equation (7) in the limit $\tau \gg 1$.

In cases where τ is of order unity (i.e., τ does not fit into either the optically thin or the optically thick case), the column density is obtained from equation (22) using an optical depth obtained from equation (7).

(b) CO Infrared Absorption Lines

The first step in the reduction of the infrared absorption spectrum of GL 490 is to ratio it with a reference spectrum to remove telluric absorption. Specifically, the spectrum of GL 490 was divided by the spectrum of the moon. Figure 11 shows a portion of the ratioed spectrum of GL 490. The strongest lines are the ^{12}CO lines at rest velocity, which are clearly saturated. The feature immediately to the blue of the ^{12}CO line is an outflow feature moving at -13 km s^{-1} with respect to the rest velocity gas. There is another marginally detected absorption feature velocity shifted by -33 km s^{-1}.
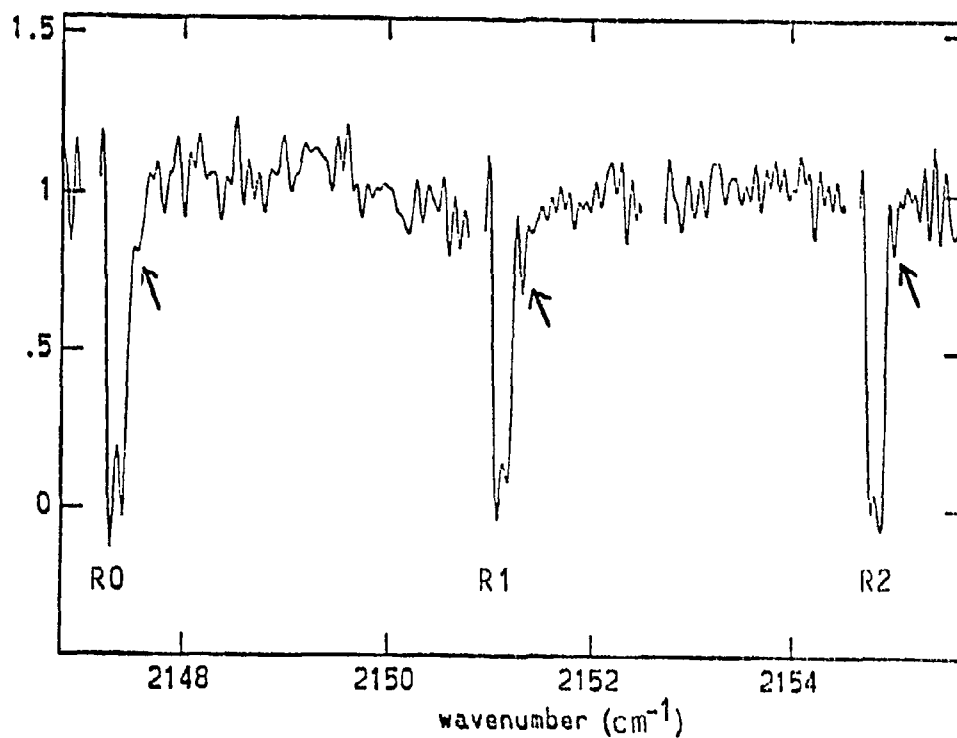
Fig. 11 The spectrum of GL 490 is divided by the spectrum of the Moon to correct for atmospheric absorption. Lines of ^{12}CO v = 0 → 1 at the cloud velocity are labeled. Two strong absorption components are present, one at the cloud velocity, the other blueshifted by 13 km s^{-1}. The weak blueshifted component labeled with arrows has an outflow velocity of 33 km s^{-1}.

Column densities of the absorbing gas can be obtained using the curve-of-growth analysis. By definition, the equivalent width of the line is given by

$$W_\lambda = \int \left(1 - \frac{I_v}{I_c}\right) d\lambda,$$ (41)

where I_v is the intensity at frequency v

and I_c is the intensity of the continuum.

Substituting $d\lambda = \frac{\lambda^2}{c} dv$ and $I_v = I_c e^{-\tau_v}$ (assuming no emission), we have

$$W_\lambda = \frac{\lambda^2}{c} \int (1 - e^{-\tau_v}) \, dv.$$ (42)

If the velocity distribution is Maxwellian, equation (42) can be written in the form

$$\frac{W_\lambda}{\lambda} = \frac{2b}{c} F(\tau_0).$$ (43)

Here $b = \frac{\Delta v_{1/2}}{1.665}$ is the Doppler broadening parameter,

$\Delta v_{1/2}$ is the full width at half intensity level,

τ_0 is the optical depth at line centre given by

$$\tau_0 = \frac{0.015}{b} N_j \, \lambda \, f_{jk};$$ (44)

and $F(\tau_0)$, by definition, is

$$F(\tau_0) \equiv \int_0^\infty [1 - \exp(-\tau_0 \, e^{-x^2})] \, dx,$$ (45)

where N_j is the column density of the absorbing gas in the lower state and f_{jk} is the upward absorption oscillator strength from transition level j to level k.

$\dfrac{W_\lambda}{\lambda}$ and b can be measured from the spectra, $F(\tau_0)$ is calculated using equation (43) and τ_0

is obtained using equation (45). Equation (44) can then be used to derive the column

density of gas in the lower state. If rotational states are thermally populated, the Boltzmann

equation applies. In this case, a plot of $\ln[N_J/(2J+1)]$ versus $\exp(-E_J/kT)$, where E_J is the

energy of the J rotational state above ground level, should yield a straight line with the gas

temperature being simply the inverse of the slope.

III. Results

(A)   THE J = 3 → 2 TRANSITION : CLUMPS IN THE OUTFLOW

The ^{12}CO J = 3 → 2 spectral line map (Fig. 7) shows that broad line wings exist within 40" of GL 490 except towards the south-east, where the line wings have diminished rather abruptly. Specifically, at position (10,-10), strong wings can still be seen but at (20, -20), the wings have almost disappeared [note that the first coordinate in (x,y) refers to the direction east (positive) or west (negative) of GL 490 and the second coordinate refers to the direction north (positive) and south (negative) of GL 490]. This indicates that either the outflow in this direction is somehow obstructed or the high-velocity gas does not flow in this direction. It is instructive to look at the ^{13}CO J = 3 → 2 spectral line map (Fig. 9) as a comparison to the ^{12}CO line. The ^{13}CO displays no sudden change in line shape in the south-east direction. However, the peak emission is significantly lower ($T_A^* < 3.5$ K) than that shown in the spectral line at (-10,10) ($T_A^* \sim 4.8$ K), which is on the north-west side of GL 490. This confirms that the physical environment on the southeastern direction of the source is different from the rest of the molecular cloud, although the implication is not clear. Besides the sharp transition between strong and weak line wings in the SE direction, the spectral line map in Figure 7 also displays rapid changes in the strong wings with position across the map region. Typically, the appearance of the line wings varies noticeably on scales of 10" to 20". Strong blue wings can be seen in the south-west direction near GL 490, while strong red wings are evident generally to the north near the source. This segregation of red and blue wings clearly reveals the bipolar nature of the outflow.

At the position of the source, the total velocity extent at zero intensity of the ^{12}CO J = 3 → 2 line is 74 km s^{-1} and the peak antenna temperature is $T_A^* = 15.3$ K at $V_{LSR} = -14.0$

Fig. 12   Selected ^{12}CO J = 3 → 2 spectra. The map coordinates for each spectrum are given in arcseconds from GL 490. North and East are positive. The straight line drawn through the spectra indicates a velocity of -13.5 km s^{-1}.

km s^{-1} (see Fig.12(a)). This -14.0 km feature can be seen throughout the ^{12}CO J = 3 → 2 line map (Fig. 7) but peaks at the position of the source. Measurements show, however, that this peak varies in velocity by about ±0.5 km s^{-1} in different spectra. Since our spectra have typical velocity resolution of 0.13 km s^{-1}, this observed shift in velocity of peak antenna temperature is significant. There are two possibilities that can explain the variation of velocities for the peak antenna temperature. First, rotation of the molecular cloud may produce the observed velocity shifts. Second, due to the overlapping absorption feature at -11km s^{-1} (to be discussed in the next paragraph), the velocity of the peak seen in each spectrum is not the true velocity of the molecular cloud. The true velocity of the cloud is therefore masked by the absorption feature. To assess the validity of the above two possibilities, we refer to at the ^{13}CO J = 3 → 2 spectra (selected spectra are shown in Figure 13). All the ^{13}CO spectra have a velocity for the peak antenna temperature of -13.5 km s^{-1}. This intensity peak at -13.5 km s^{-1} is identified as the velocity of the molecular cloud core by Lada and Harvey (1981) and Snell et al. (1984), as well as by Mitchell et al (1992). The ^{13}CO spectra do not show any velocity shift of the peak, therefore, we may dismiss the first hypothesis, i.e., the velocity shift is not caused by the rotation of the molecular cloud. In view of the absence of the -11 km s^{-1} absorption feature in the ^{13}CO spectra, we believe that the second hypothesis is more likely. That is, -13.5 km s^{-1} is the true velocity of the molecular cloud, and the velocity shifts seen in the ^{12}CO spectra are the result of the absorption feature at -11 km s^{-1}.

An absorption feature centred at -11 km s^{-1} and about 3 km s^{-1} wide occurs in all ^{12}CO J = 3 → 2 spectra within 40" of GL 490 (Fig. 8). ^{13}CO J = 3 → 2 spectral lines at the source position as well as at all the other mapped positions do not show this absorption feature. However, at the velocity of -11 km s^{-1}, almost all ^{13}CO J = 3 → 2 spectra display a "shoulder" which may correspond to the absorption feature in ^{12}CO. These J = 3 → 2 observations are consistent with the ^{12}CO and ^{13}CO J = 2 → 1 results published by
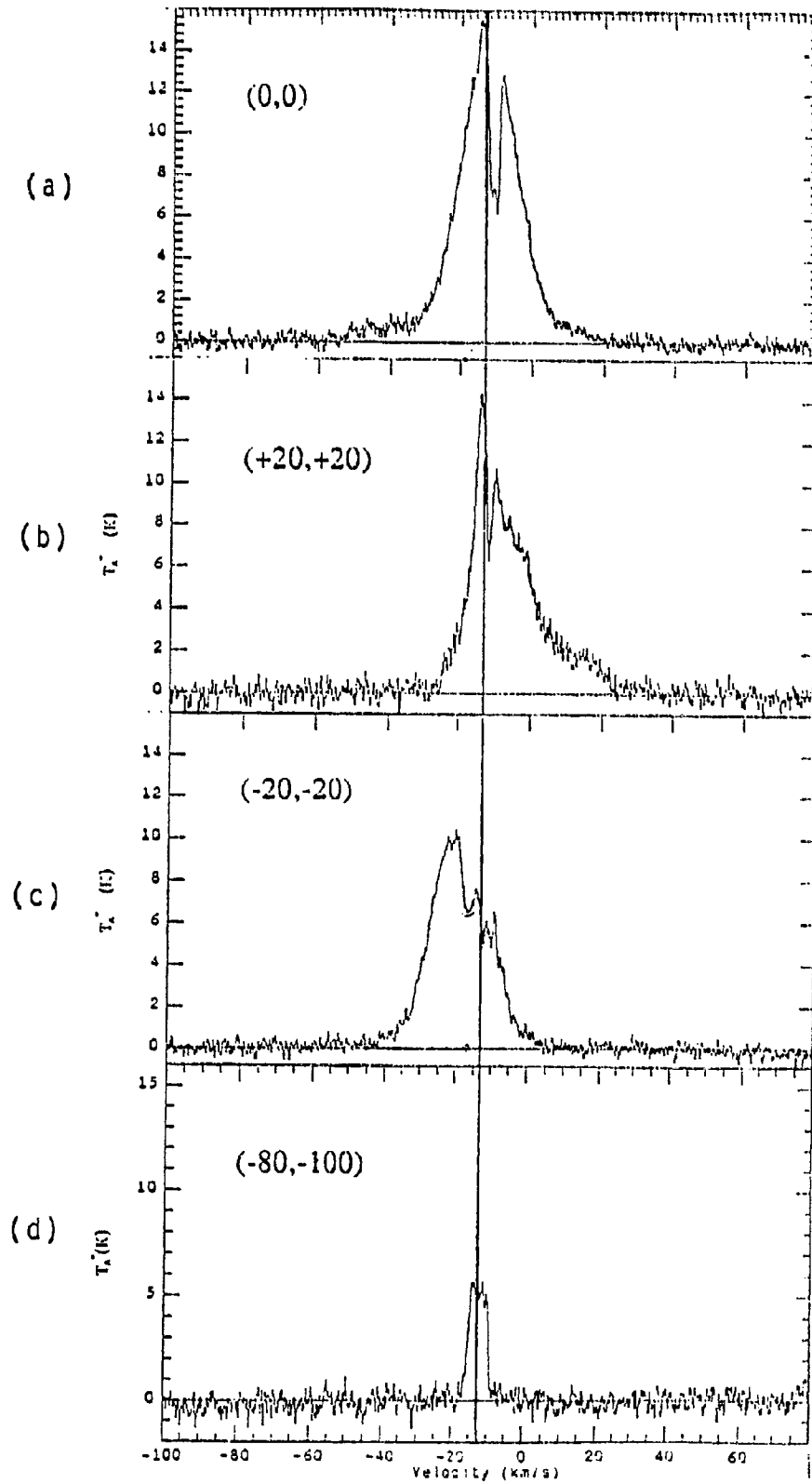
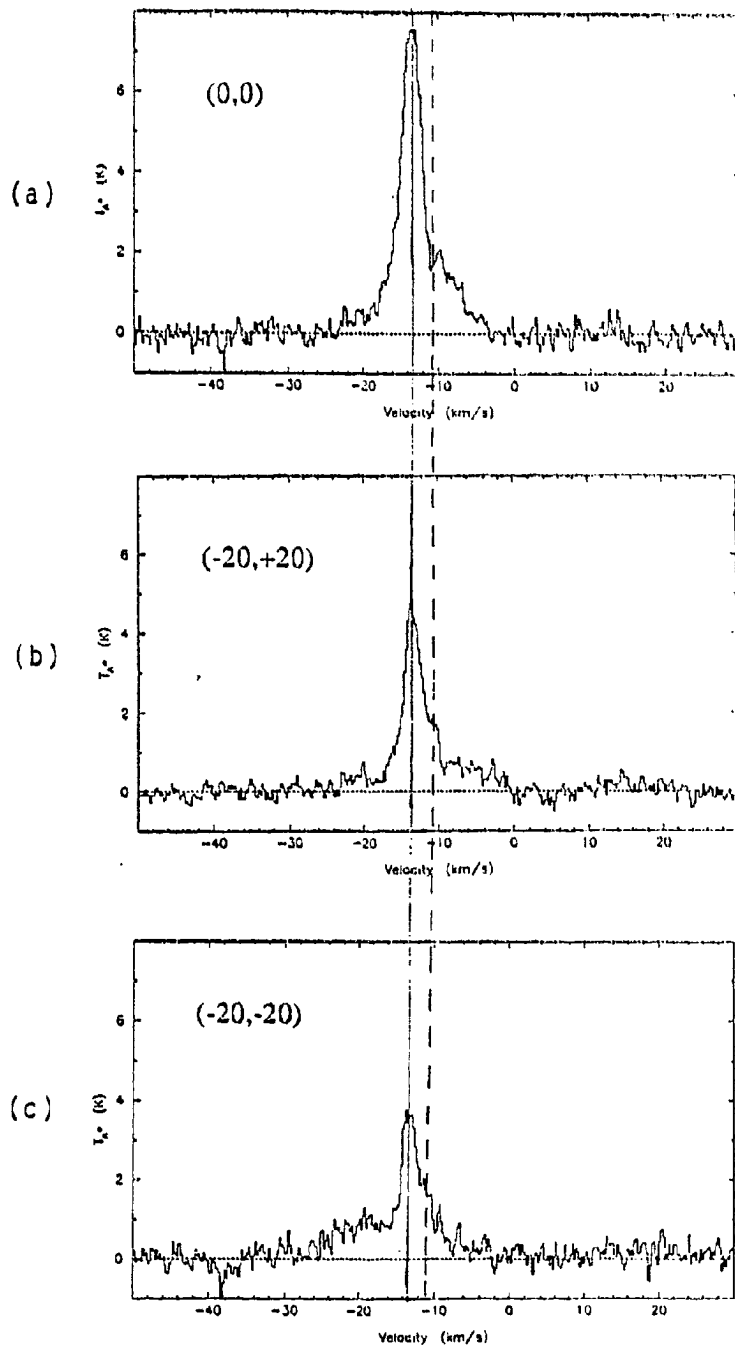Fig. 13   Selected ^{13}CO J = 3 → 2 spectra. The map coordinates for each spectrum are given in arcseconds from GL 490. North and East are positive. The solid straight line indicates a velocity of -13.5km s^{-1} and the dotted line indicates a velocity of -11 km s^{-1}.

Mitchell et al. (1992). In their paper, Mitchell et al. stated that the -11 km s^{-1} feature cannot simply be self-absorption because the ^{13}CO line peaks at the same velocity as the ^{12}CO line, that is -13.5 km s^{-1}. The absorption features in our ^{12}CO spectra at positions far from GL 490 (Fig. 12(d)), as in the Mitchell et al. data, do not show Gaussian line profiles. These spectra are either flat-topped or display multiple peaks, and are consistent with the blending of at least two emission components, one at the cloud's rest velocity and the other at -11 km s^{-1}. Hence, the two interpretations given by Mitchell et al. (1992) are still possible, namely, the dip in the ^{12}CO line at -11 km s^{-1} is caused either by an unrelated foreground cloud or by a colder outer region of the molecular cloud in which GL 490 is embedded.

Inspecting the line shapes in the ^{13}CO J = 3 → 2 map (Fig. 9), we see that, at the position of the source, the peak antenna temperature is 7.6 °K. The spectrum has broad wings with a velocity extent (at zero intensity) of ~ 27 km s^{-1}. At 30" west of GL 490, the peak antenna temperature of the ^{13}CO line drops to 2.8 K, almost three times weaker than the peak antenna temperature at source centre. Towards the southwest (Fig.13(c)), where strong blue wings are seen in the ^{12}CO J = 3 → 2 lines, the ^{13}CO line profile also displays strong blueshifted emission. At (20,20), as well as the general region north of GL 490, the red wing becomes very strong and broad while the blue wing weakens. This trend is consistent with the bipolarity seen in other transitions.

Velocity channel maps (Figs.14, 16) were made from both the ^{12}CO and the ^{13}CO J = 3 → 2 spectral line maps. Contour levels for the ^{12}CO channel maps are listed in Table 2. A number of intensity peaks (hereafter referred to as 'clumps') are distinctly visible in the ^{12}CO channel maps. Positions of the most prominent clumps are listed in Table 3 together with their corresponding velocity ranges. Positions of each clump are also marked on Figure 14 at their respective central velocities. At (-10,0), clump B2 first appears in our

channel maps at -55 km s^{-1} [Fig. 14 (1)] and persists to V$_{LSR}$ = -40 km s^{-1}. It is interesting to note that clump B2 seems to move towards the west as the velocity difference relative to the ambient cloud decreases, possibly indicating a decelerating flow. The transition between clump B3 at (-30,0), which first appears at V$_{LSR}$ = -40 km s^{-1} [Fig. 14(3)] and remains visible to V$_{LSR}$ = -30 km s^{-1}, and clump B2 is so smooth that the two clumps may be components of a larger entity. Clump B1, at (-20,-20), is the main blueshifted outflow gas. It shows a fan-shaped structure with the vertex of the fan pointing away from GL 490, and persists over a velocity range of V$_{LSR}$ = -36 to -18 km s^{-1} [Figs. 14(6) to 14(23)]. At V$_{LSR}$ = -20 km s^{-1}, clump B4 at (0,0) begins to become visible [Fig. 14(22)] with a velocity width of about 5 km s^{-1}. At the velocity interval V$_{LSR}$ = -13 to -9 km s^{-1} [Fig. 14(29) to Fig. 14(32)], emission is dominated by the quiescent molecular cloud gas. In the velocity range -12 to -10 km s^{-1}, CO emission is not a measure of column density because of the absorption feature at -11 km s^{-1}. The chaotic appearance of the velocity channel maps in this velocity range (30 and 31 of Fig. 14) is not physically significant.

The redshifted gas also shows interesting structure in the ^{12}CO J = 3 → 2 channel maps. Mitchell et al. (1992) noted that the redshifted gas displays an elongated structure with the long axis pointing east-west and the centroid roughly 20" north of GL 490. From the present ^{12}CO J = 3 → 2 data, this elongated structure is seen to consist of two distinct yet almost equally intense clumps. Of the two clumps, the eastern one [R1 at (20,20), see Figs. 14(36) to 14(54)] is almost directly on the opposite side of GL 490 relative to the main blue peak (B1). Clump R1 is first seen at V$_{LSR}$ = -5 km s^{-1}, and remains a strong component to V$_{LSR}$ = +20 km s^{-1}. The western clump [R2 at (-20,20)], located about 40" north of the main blue peak (B1), is first seen at V$_{LSR}$ = -10 km s^{-1} [Fig. 14(32)]. It persists strongly to V$_{LSR}$ = +7 km s^{-1}, weakens to become only an extension of clump R1, and then reappears as an intensity peak at velocity V$_{LSR}$ = +16 km s^{-1} [Fig. 14(53)]. The centroid of R2 appears to shift with velocity and describes an arc as the velocity changes
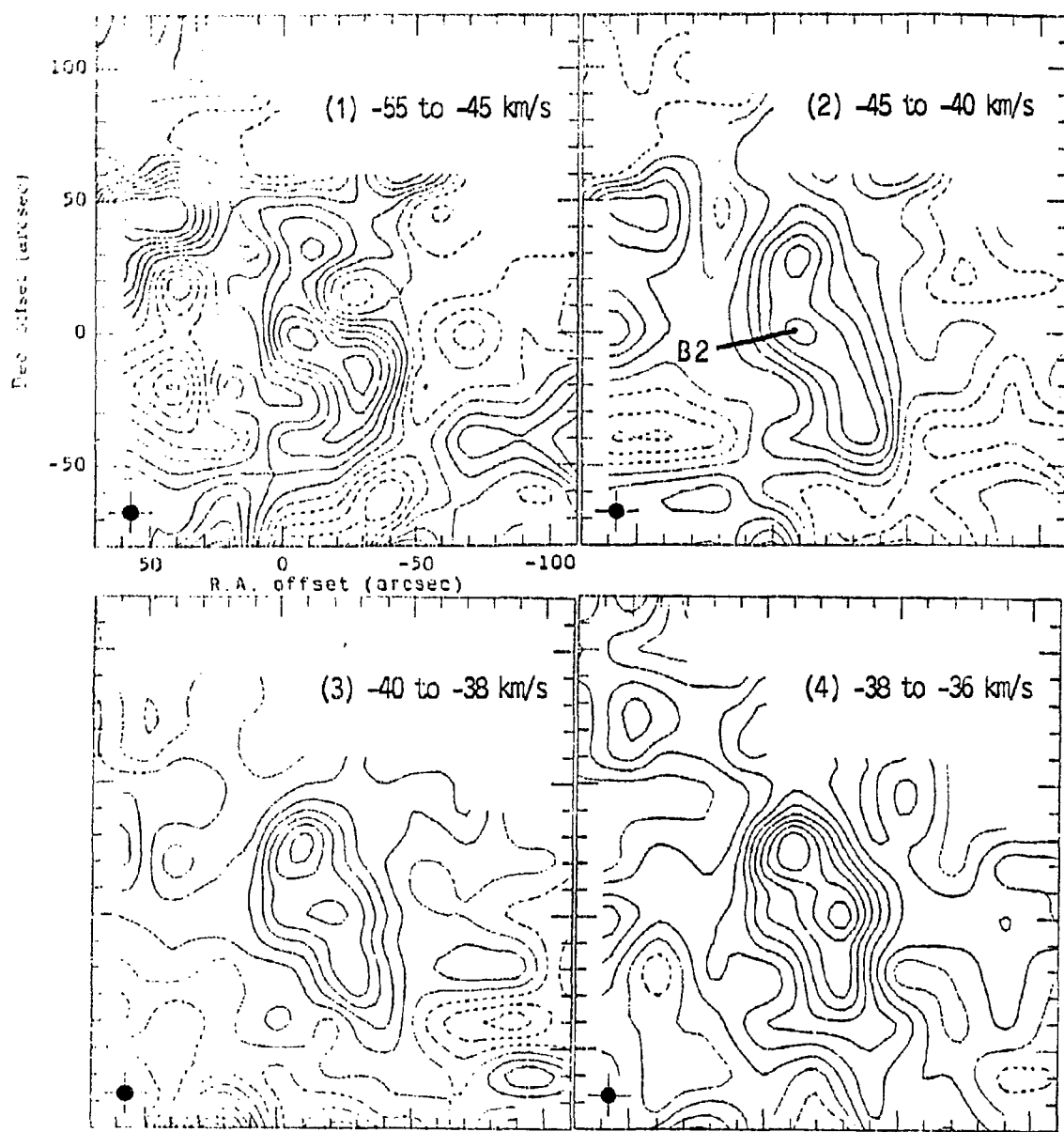
Fig. 14 ^{12}CO J = 3 → 2 channel maps of GL 490 showing the changing spatial distribution of CO emission as a function of velocity. Velocity intervals in km s^{-1} are shown on top of each map, and the contour levels are listed in Table 2. The HPBW (15") is shown as a cross in the lower left hand corner. GL 490 is located at (0,0).
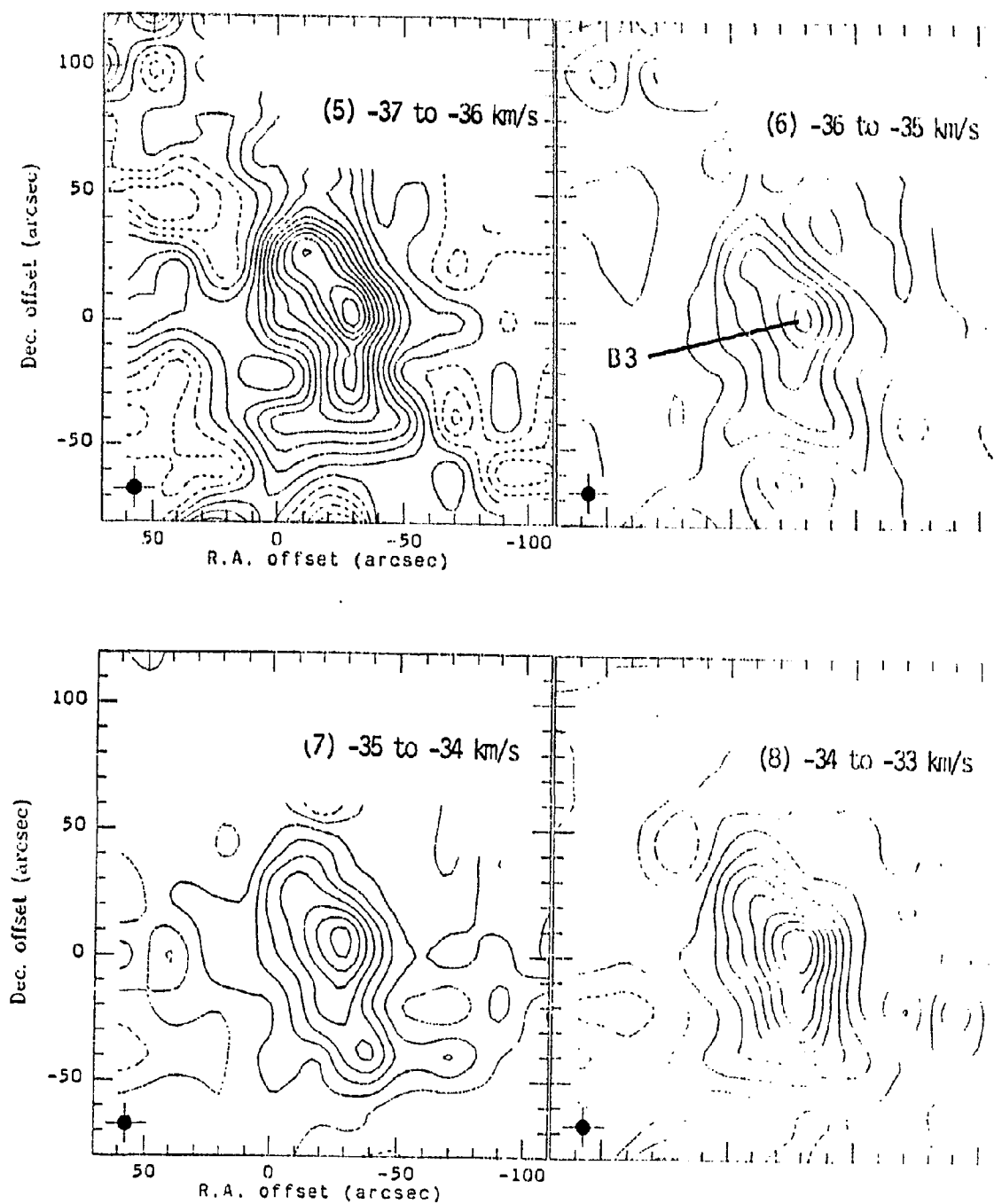
Fig. 14 (Continued)
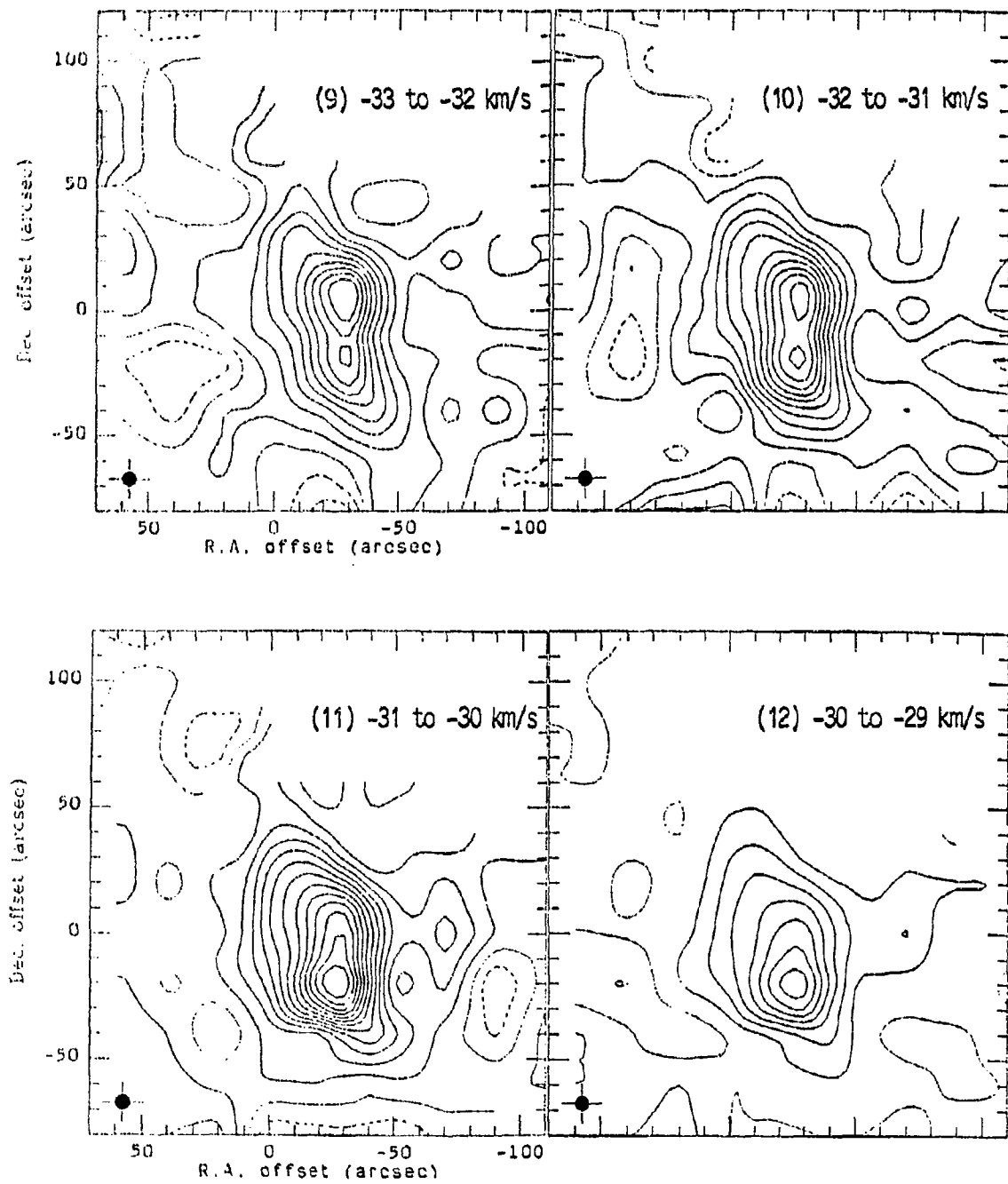
Fig. 14 (Continued)
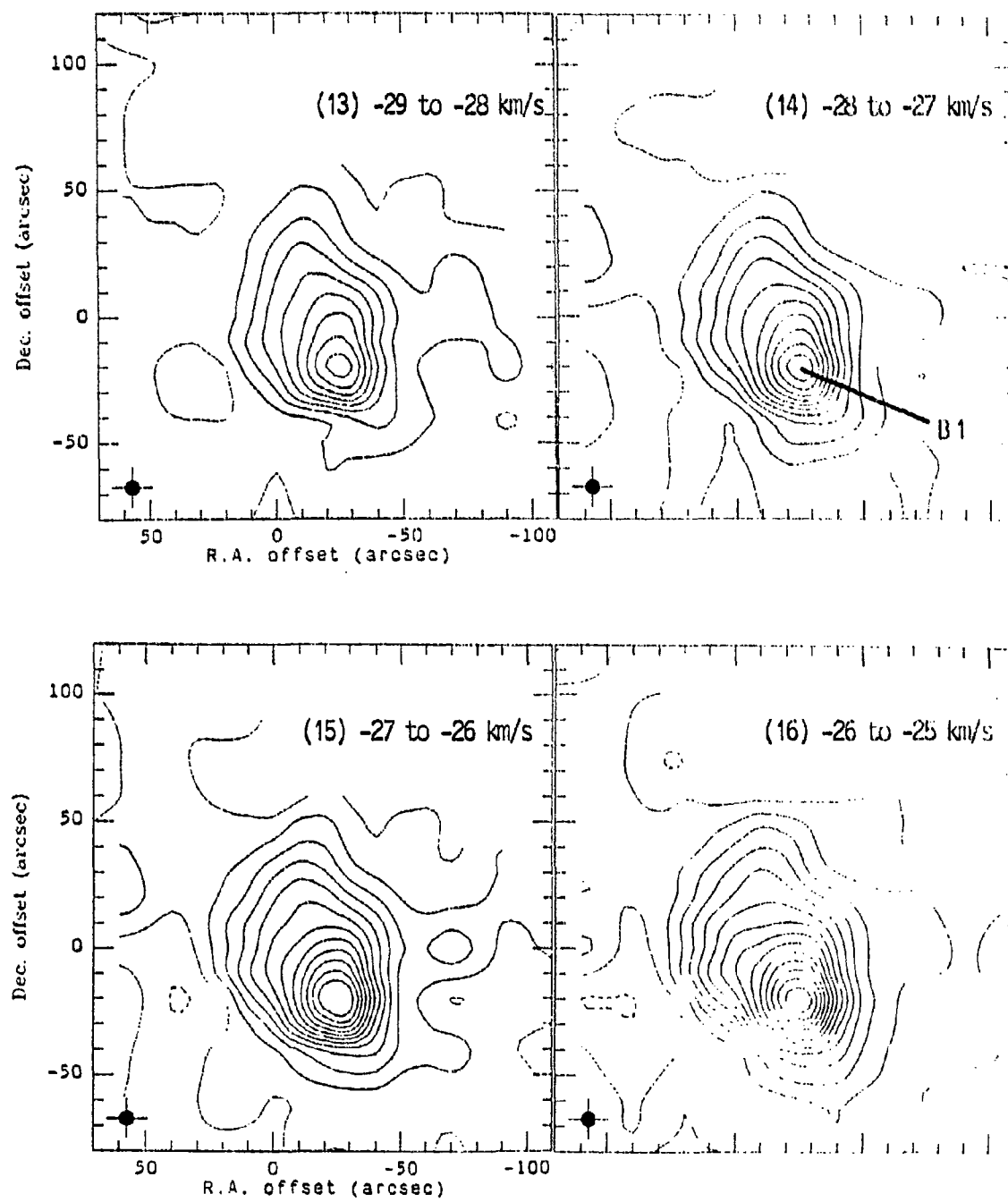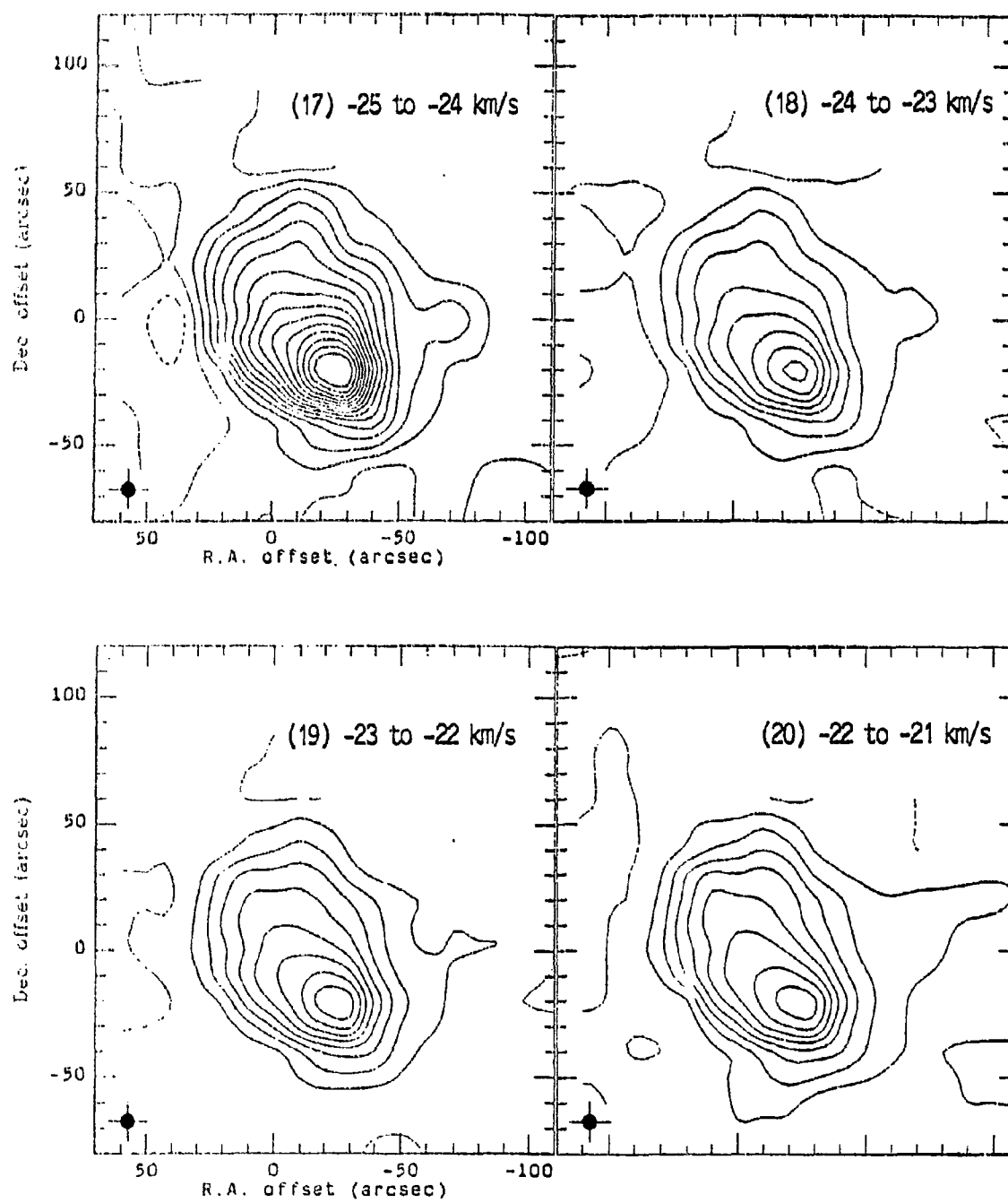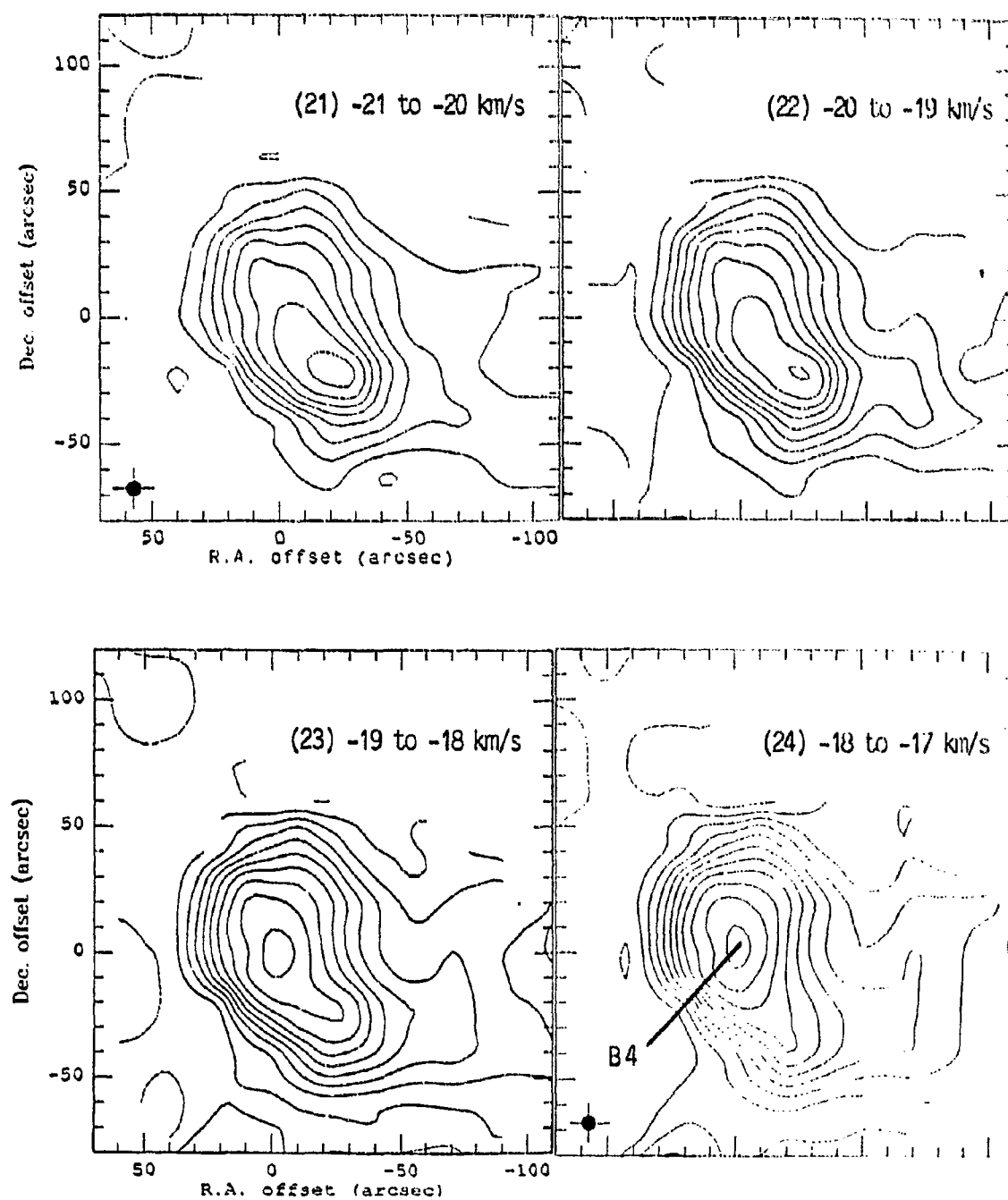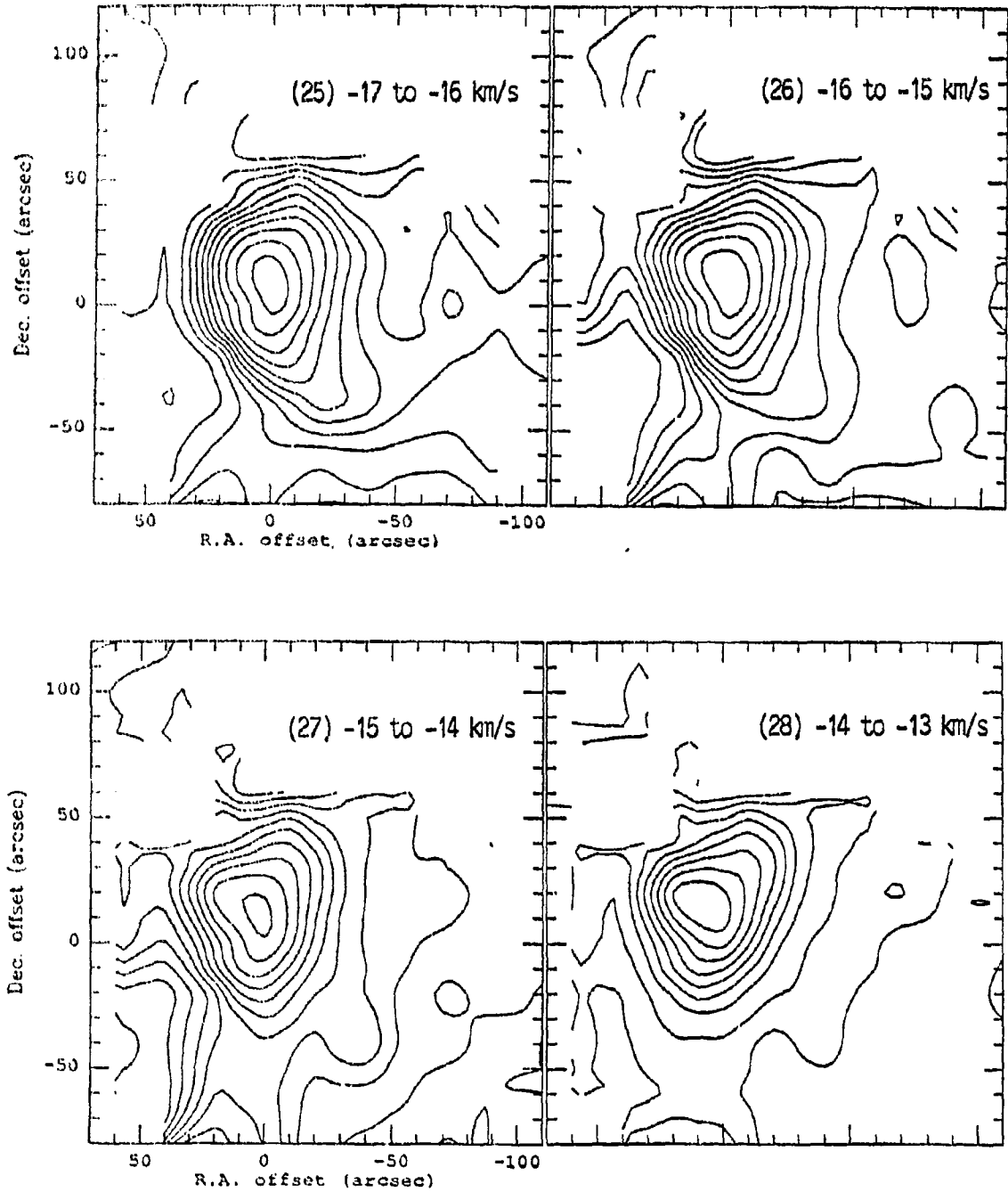
Fig. 14 (Continued)

Fig. 14 (Continued)

Fig. 14 (Continued)
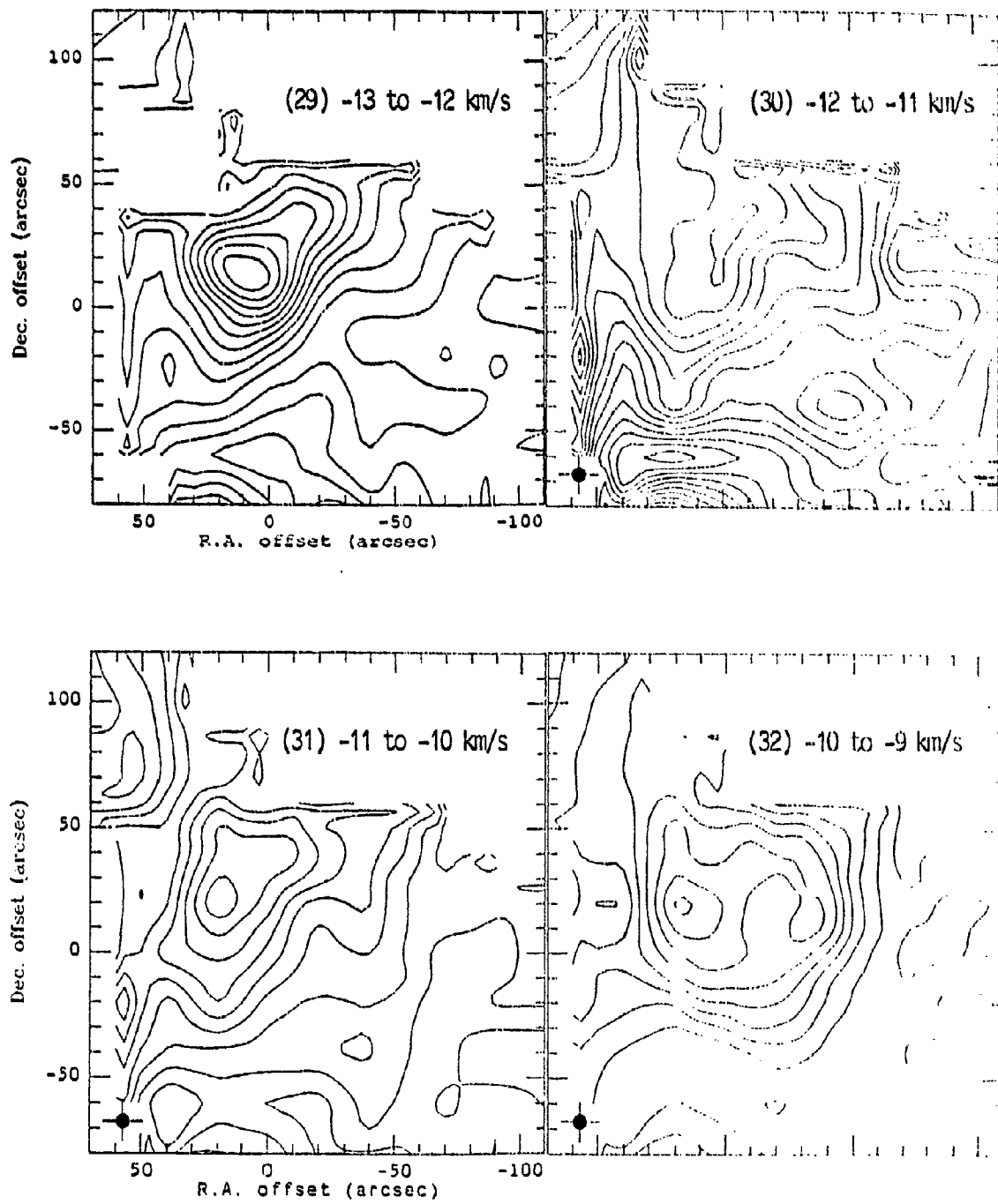
Fig. 14 (Continued)
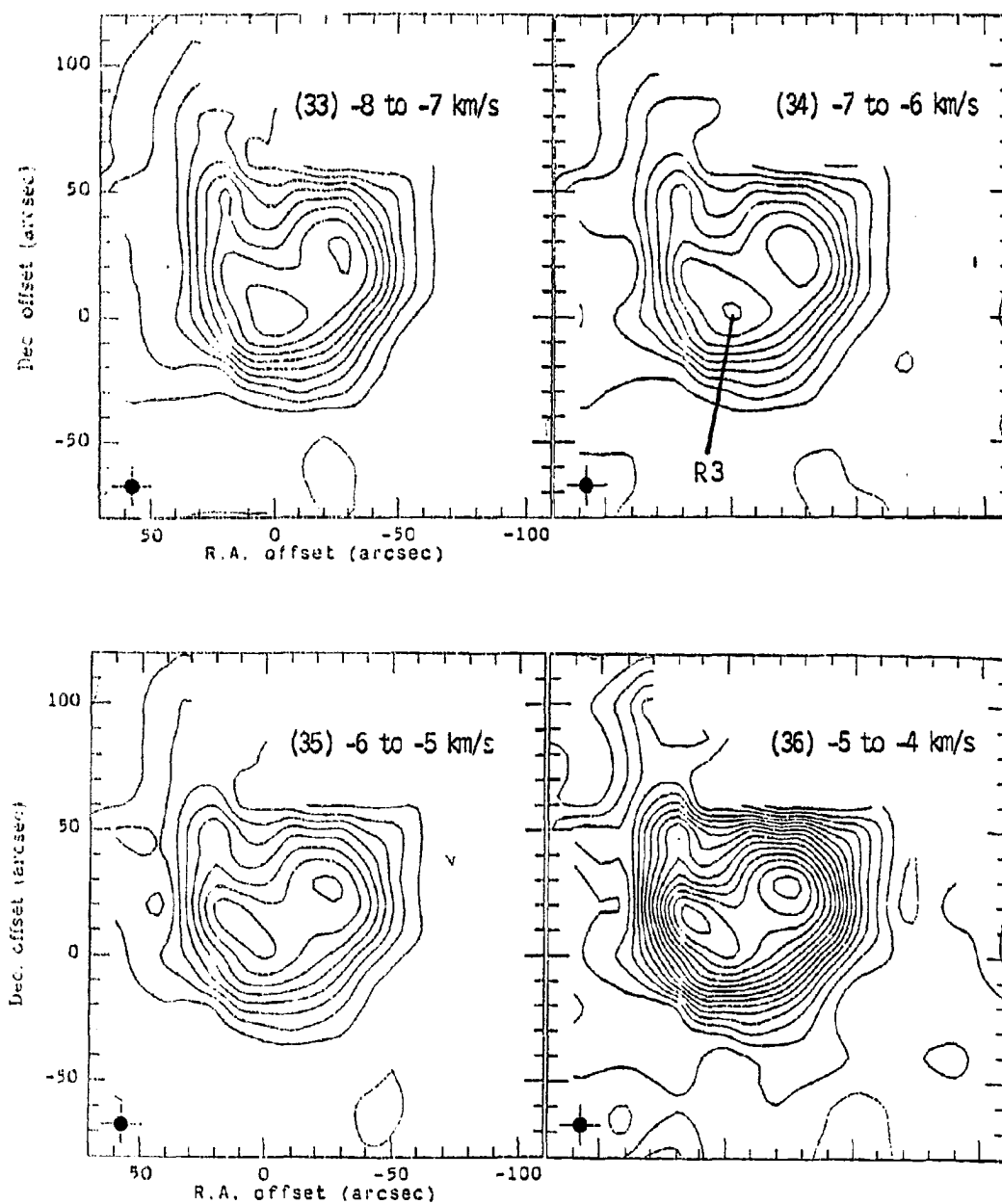
Fig. 14 (Continued)
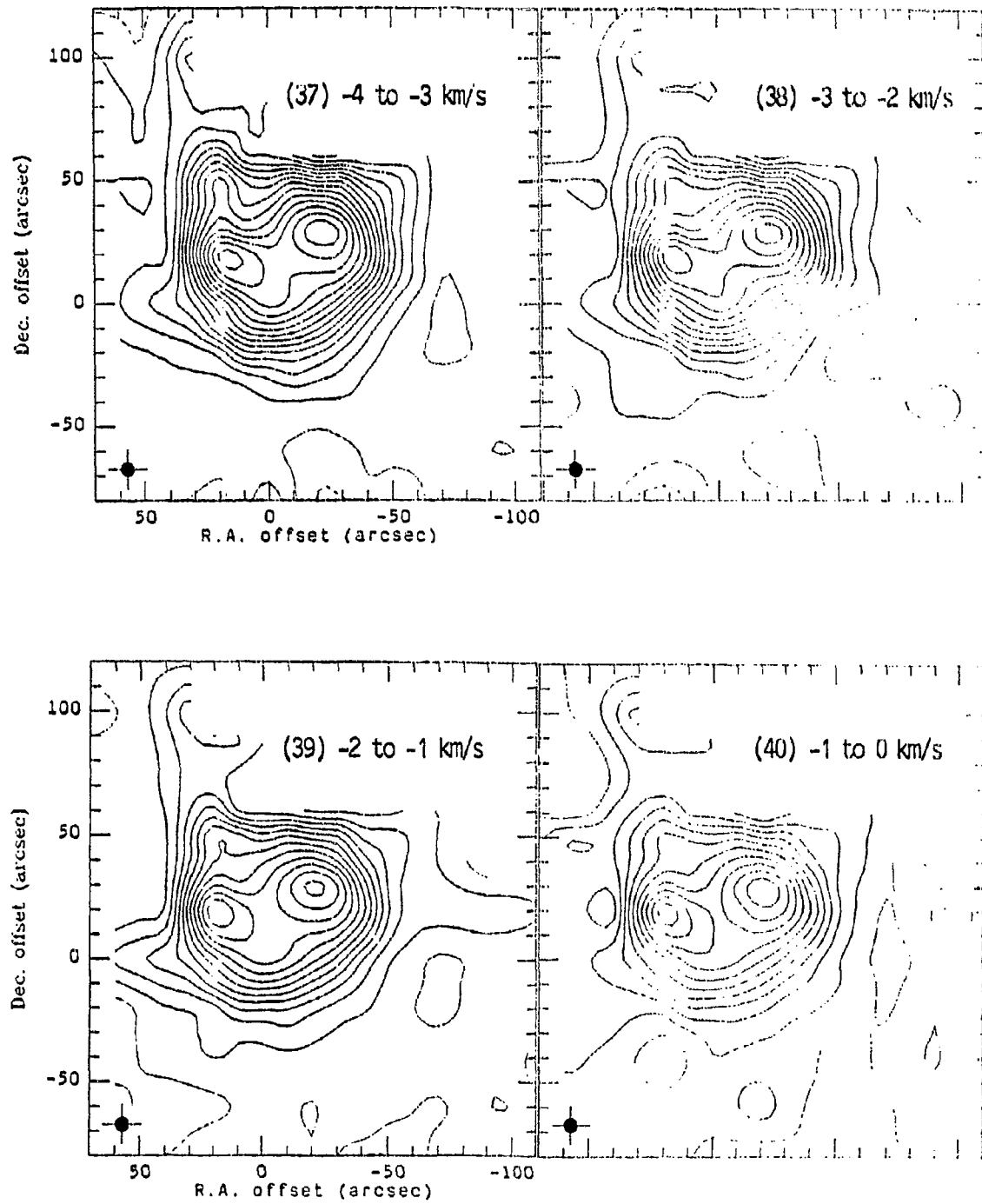
Fig. 14 (Continued)
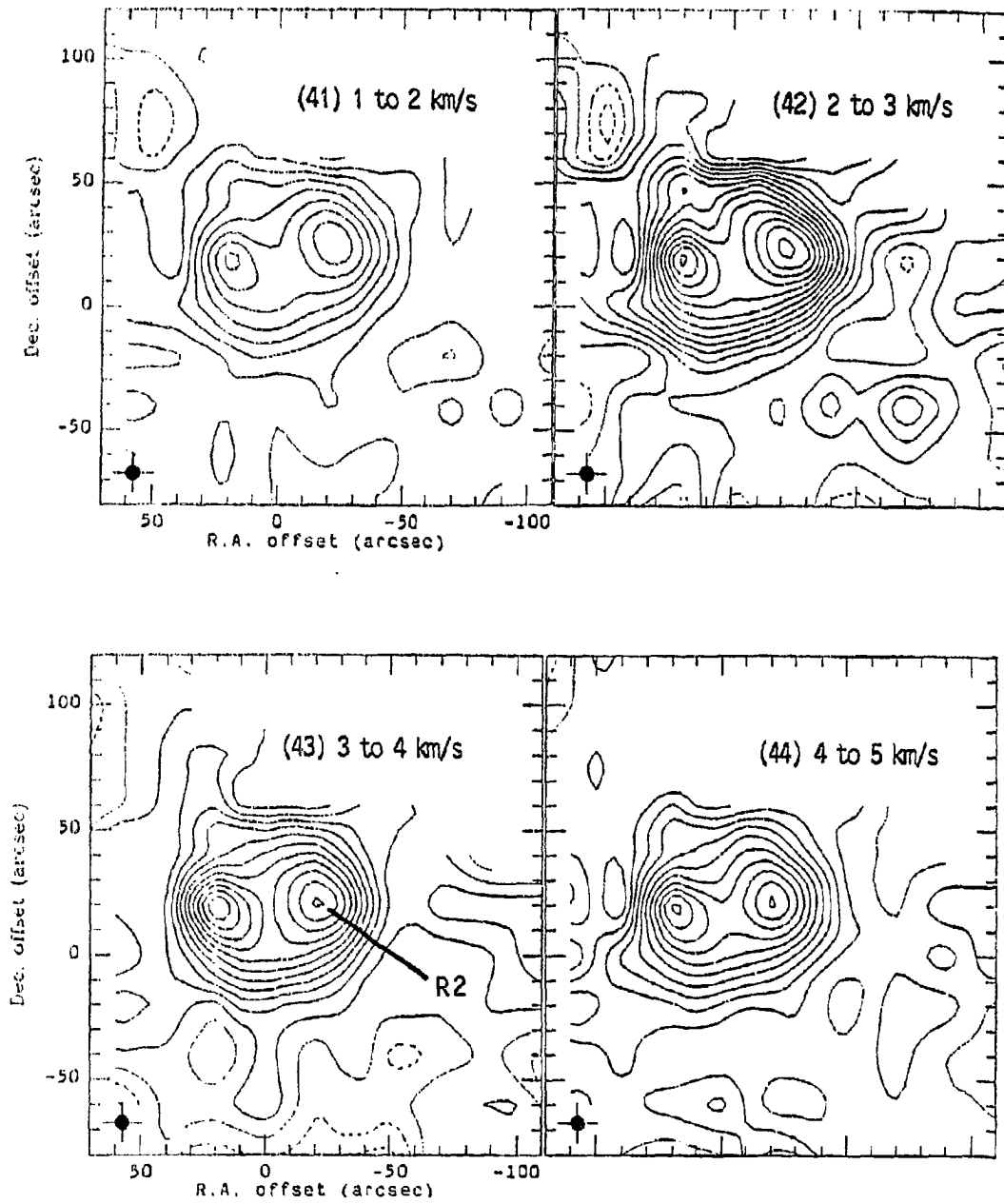
Fig. 14 (Continued)
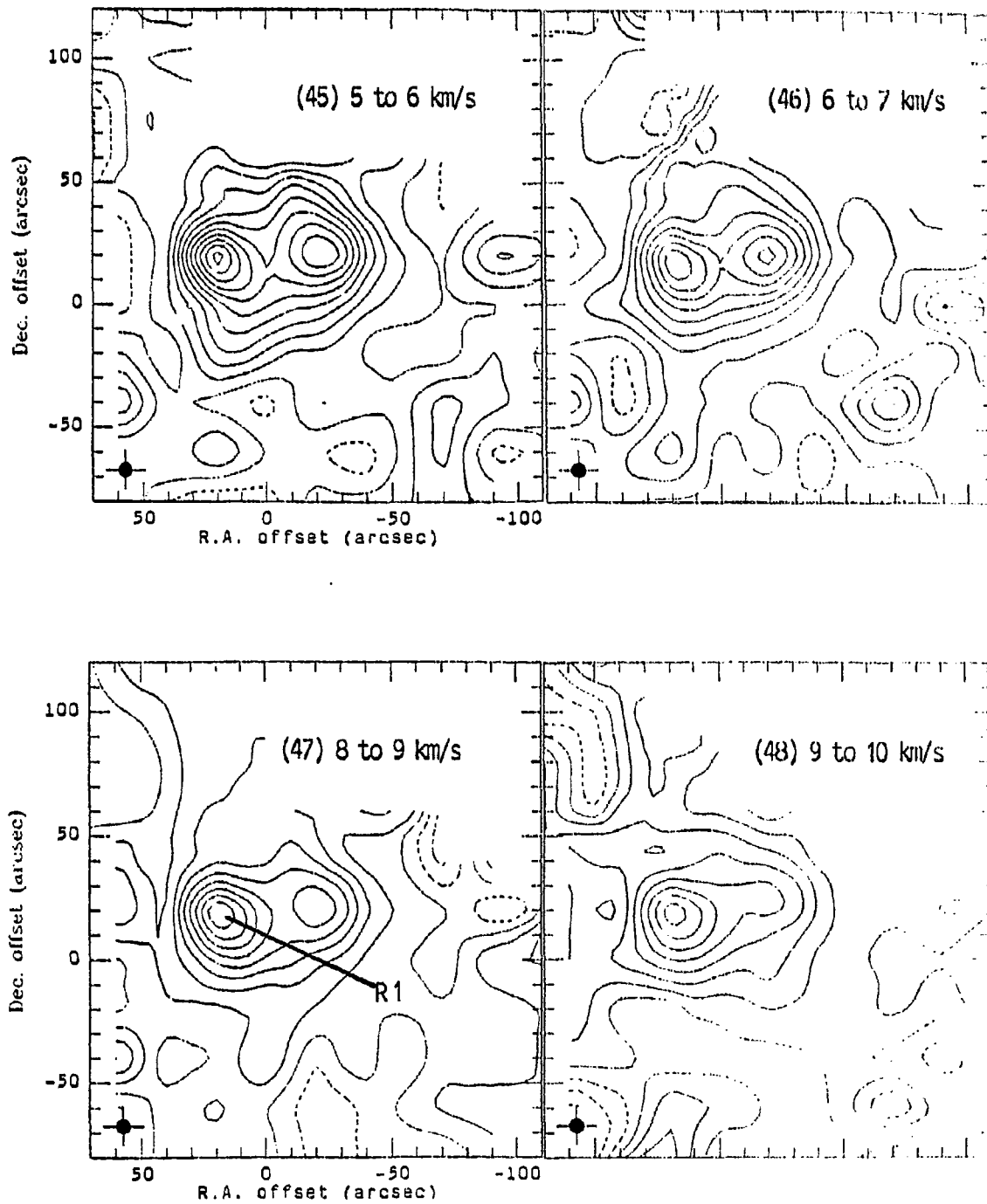
Fig. 14 (Continued)
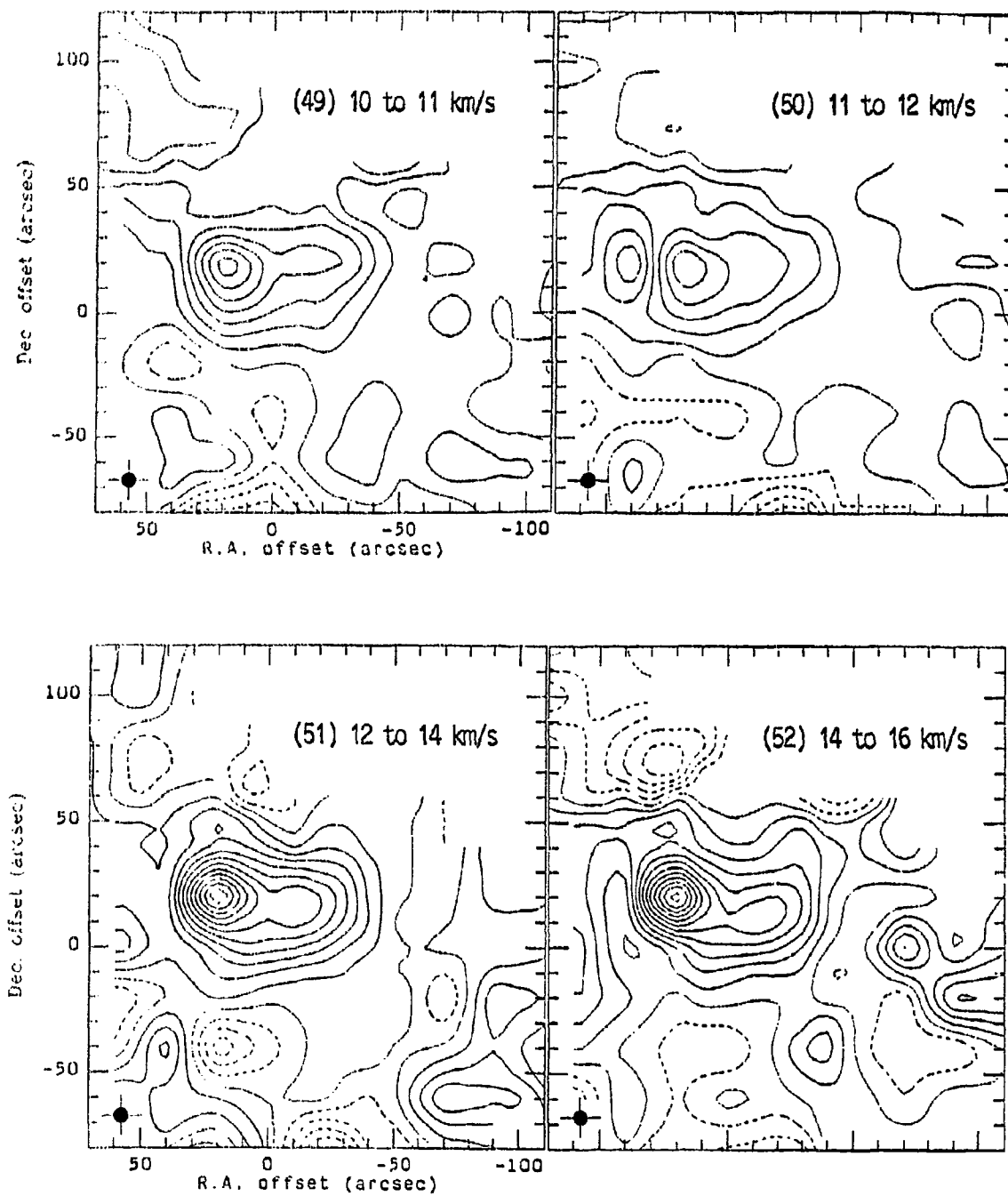
Fig. 14 (Continued)
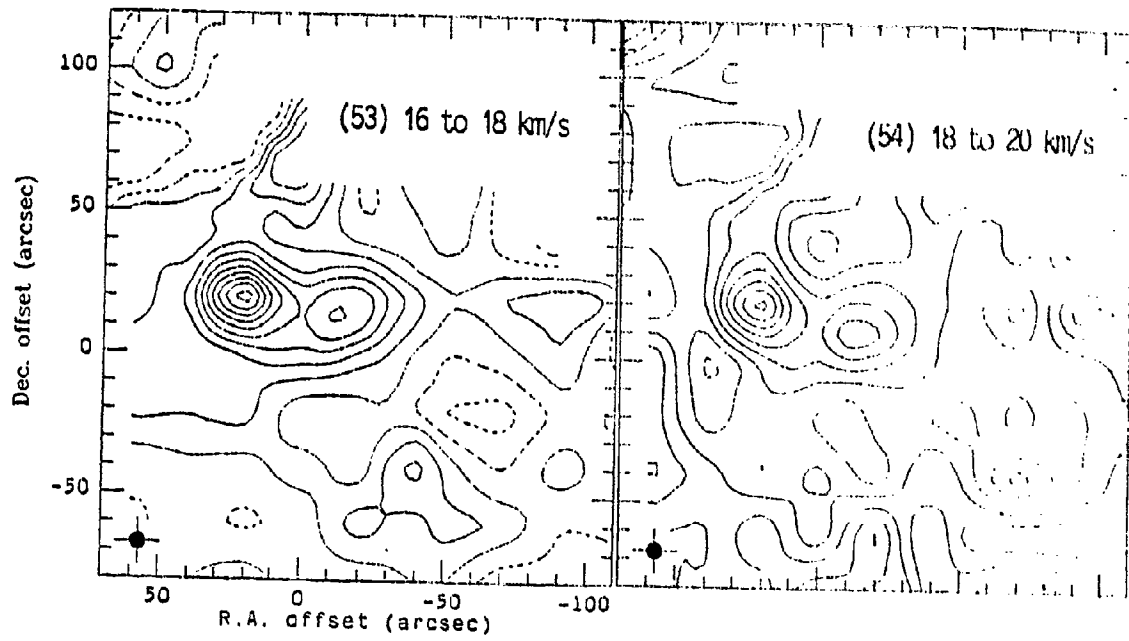
Fig. 14 (Continued)

Fig. 14 (Continued)

TABLE 2

CONTOUR MAP PARAMETERS FOR FIGURE 14

MAP	CONTOURS (K·km s⁻¹)		
	min	max	interval
1	-2.55	3.21	0.50
2	-1.62	2.75	0.50
3	-0.87	1.57	0.25
4	-0.47	2.18	0.25
5	-0.38	1.26	0.10
6	-0.52	1.57	0.25
7	-0.49	1.79	0.25
8	-0.46	2.17	0.25
9	-0.61	2.45	0.25
10	-0.47	2.54	0.25
11	-0.50	3.19	0.25
12	-0.50	3.67	0.50
13	-0.26	4.04	0.50
14	-0.33	5.12	0.50
15	-0.52	5.88	0.50
16	-0.59	6.56	0.50
17	-0.86	7.46	0.50
18	-0.67	8.02	1.00
19	-0.65	8.53	1.00
20	-0.33	8.58	1.00
21	-0.31	8.65	1.00
22	-0.98	9.04	1.00
23	-0.71	9.39	1.00
24	-0.61	10.34	1.00
25	-0.40	11.54	1.00
26	0.02	12.87	1.00
27	2.31	14.24	1.00
28	4.68	14.64	1.00
29	3.93	10.73	0.50
30	4.12	7.32	0.25
31	4.01	8.89	0.50
32	1.46	10.05	1.00
33	-0.42	9.95	1.00
34	-0.30	9.12	1.00
35	-0.21	8.47	1.00
36	-0.39	7.61	0.50
37	-0.54	7.35	0.50
38	-0.77	6.75	0.50
39	-0.51	6.15	0.50
40	-0.61	5.36	0.50
41	-0.77	3.83	0.50
42	-0.56	3.30	0.25
43	-0.57	2.95	0.25
44	-0.39	2.53	0.25

TABLE 2 (Continued)

MAP	min	max	interval
	CONTOURS (K·km s⁻¹)		
45	-0.52	2.59	0.25
46	-0.51	2.14	0.25
47	-0.56	2.19	0.25
48	-0.77	1.86	0.25
49	-0.89	1.85	0.25
50	-1.14	1.50	0.25
51	-1.23	2.94	0.25
52	1.02	2.87	0.25
53	-0.59	2.36	0.25
54	-0.89	1.82	0.25

TABLE 3

VELOCITY EXTENT OF THE CLUMPS

Feature	Position	Velocity Range (in V_{LSR}) km s⁻¹	Red/Blue-Shifted (relative to rest velocity gas)
B1	(-20,-20)	-36 to -18	Blueshifted
B2	(-10,0)	-55 to -40	Blueshifted
B3	(-30,0)	-40 to -30	Blueshifted
B4	(0,0)	-20 to -15	Blueshifted
R1	(20,20)	-5 to +20	Redshifted
R2	(-20,20)	-10 to +20	Redshifted
R3	(0,0)	-8 to -5	Redshifted
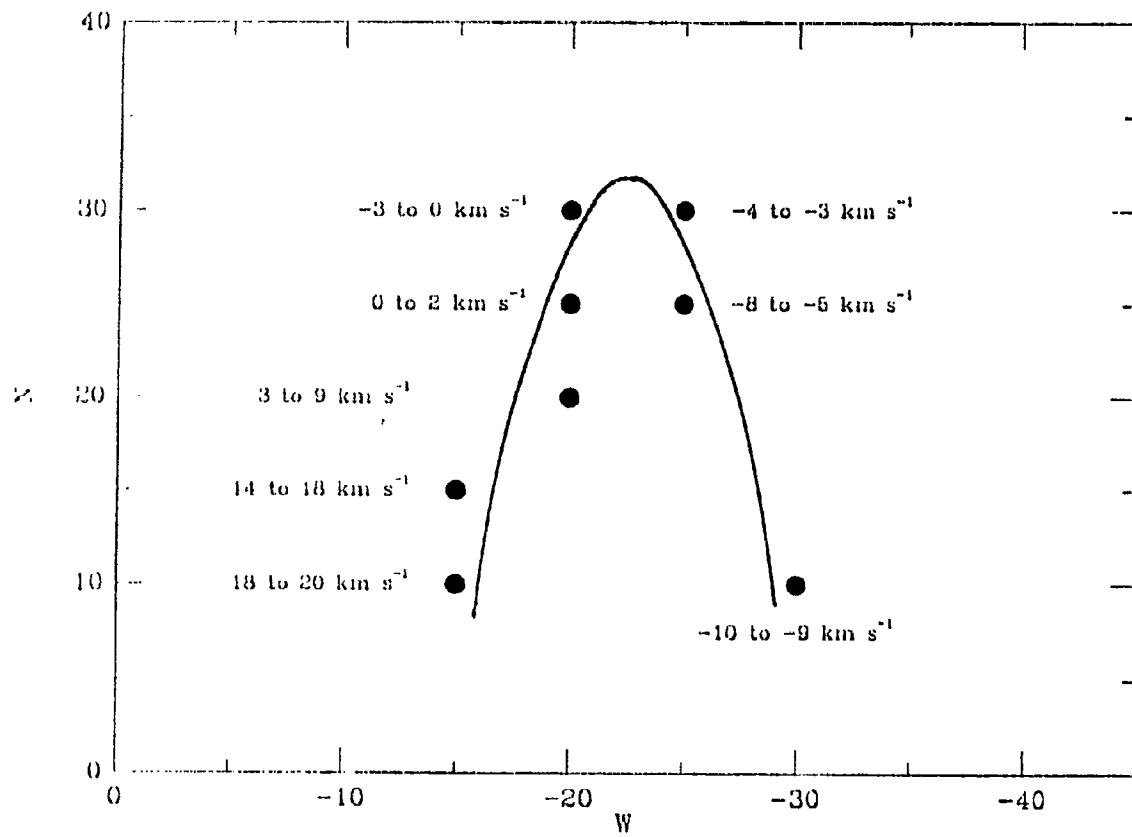
Fig. 15   Positional shift of centroid of the clump R2. The vertical and horizontal axes
are in arcseconds North and West from GL 490 respectively. Velocity intervals
are labeled beside the data points.

(Fig. 15). The peak of R2 first appears at (-30, 10) at V_{LSR} = -10 km s^{-1}, and then shifts roughly northward as velocity decreases. At V_{LSR} = -3 km s^{-1}, the peak is positioned at (-20, 30) and proceeds southward as velocity continues to decrease reaching (-15, 10) at V_{LSR} = 18 km s^{-1} [Fig. 14(54)]. The implication of the movement of this intensity peak is not apparent, since it is neither a case of straightforward acceleration nor deceleration.

It is interesting to compare the ^{13}CO velocity channel maps with the ^{12}CO channel maps described in the preceeding paragraph. Velocity channel maps for ^{13}CO J = 3 → 2 are shown in Figure 16, and corresponding contour levels are listed in Table 4. The area mapped by the ^{13}CO transition is smaller than the area mapped by the main isotope, hence only the inner 50"×50" region centred near GL 490 is displayed in the ^{13}CO J = 3 → 2 velocity channel maps. At velocities between -24 and -19 km s^{-1} [Figs 16(1) and (2)], the same blue lobe at (-20,-20) seen in ^{12}CO is also seen in ^{13}CO. There are differences in the ^{12}CO and the ^{13}CO channel maps at these velocities, however. In the ^{12}CO channel maps [Figs. 14(18) to 14(22)], the blue lobe is seen as a fan shape extending out to (20,40), while in the ^{13}CO channel maps there is essentially no emission from clump B1 near (0,0).

In Figures 16(1) and 16(2) there are two regions, around (0,-20) and (0,-10), respectively, where the emission in velocity channel maps apparently becomes negative. However, the 1σ uncertainty in the antenna temperature for the original spectrum is -±0.1 °K for each frequency channel of 0.25 km s^{-1}, corresponding to -±0.4 °K·km s^{-1} for maps having a 4 km s^{-1} velocity range. Contour levels reaching 0.75 K·km s^{-1} are correspondingly less then 2σ below the null value, which is probably not significant. These areas could therefore be regions of very weak emission, which are lost in the intrinsic noise of the observations.
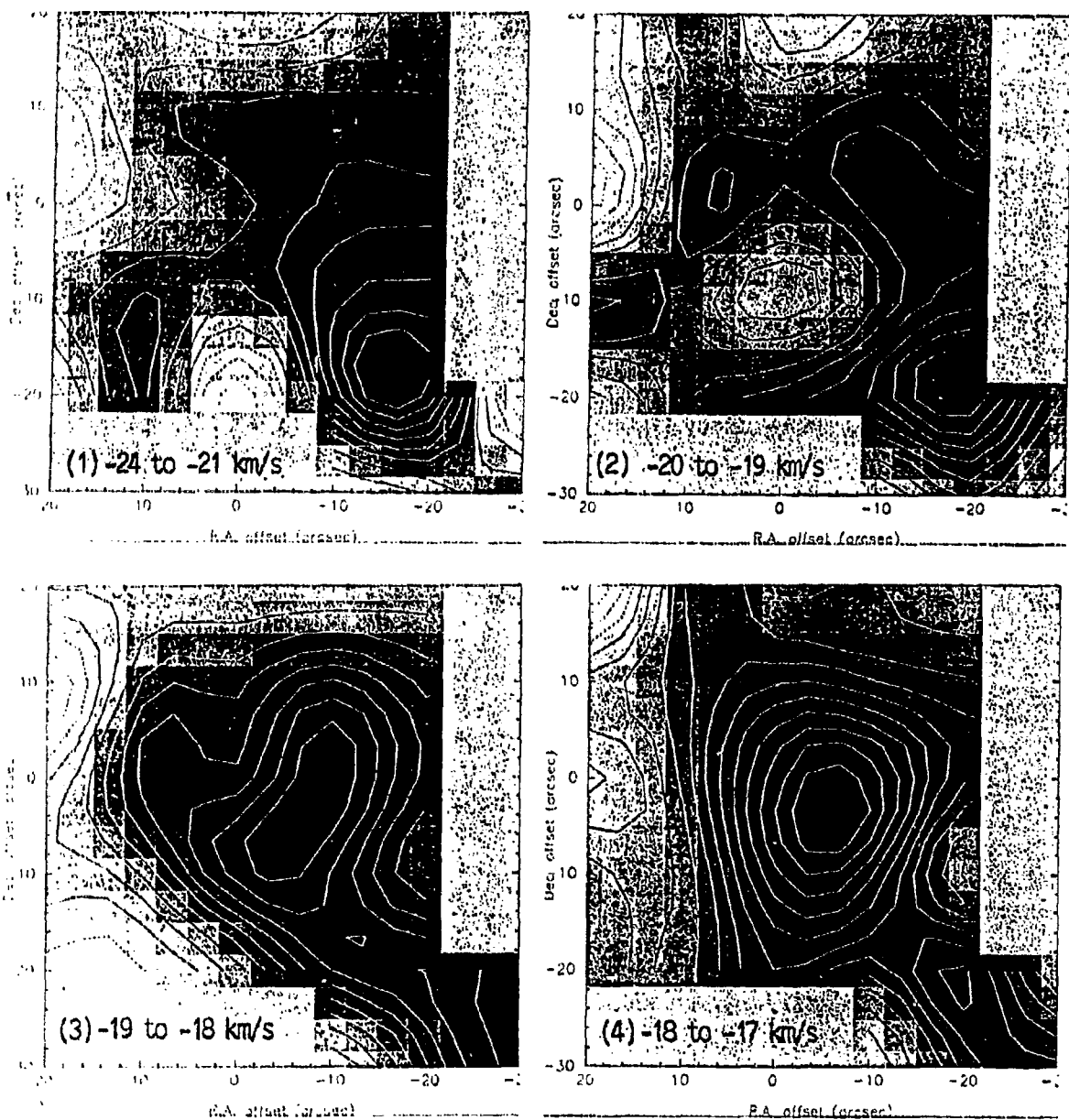
Fig. 16 ^{13}CO J = 3 → 2 channel maps. Velocity intervals in km s^{-1} are shown at the bottom of each map. Contour levels are listed in Table 4. GL 490 is located at (0,0). The rectangular areas represent regions not sampled.

(5) −17 to −16 km/s

(6) −16 to −15 km/s

(7) −15 to −14 km/s

(8) −14 to −13 km/s

Fig. 16 (Continued)

(9) -13 to -12 km/s

(10) -12 to -11 km/s

(11) -11 to -10 km/s

(12) -10 to -9 km/s

Fig. 16 (Continued)

(13) -9 to -6 km/s
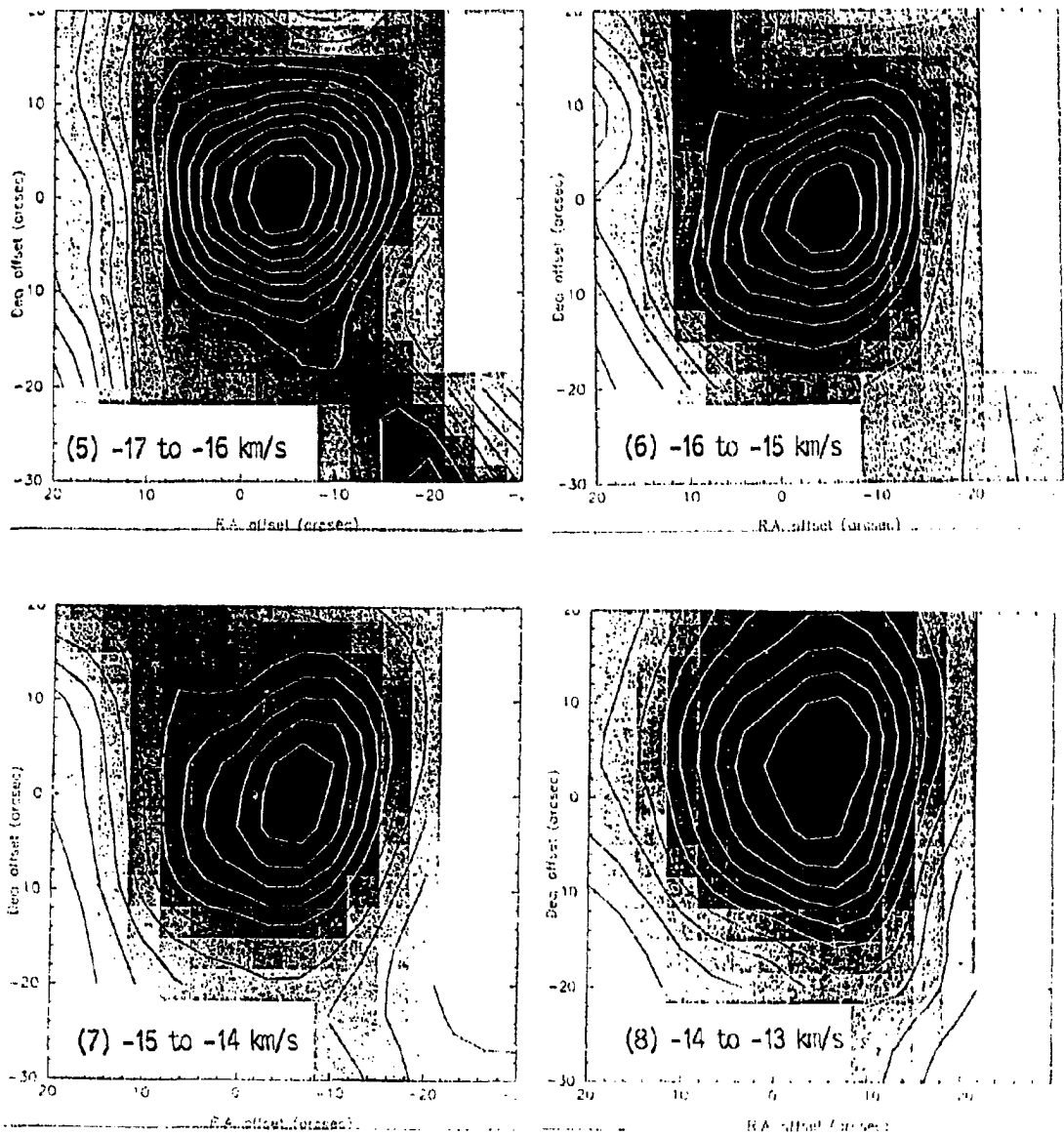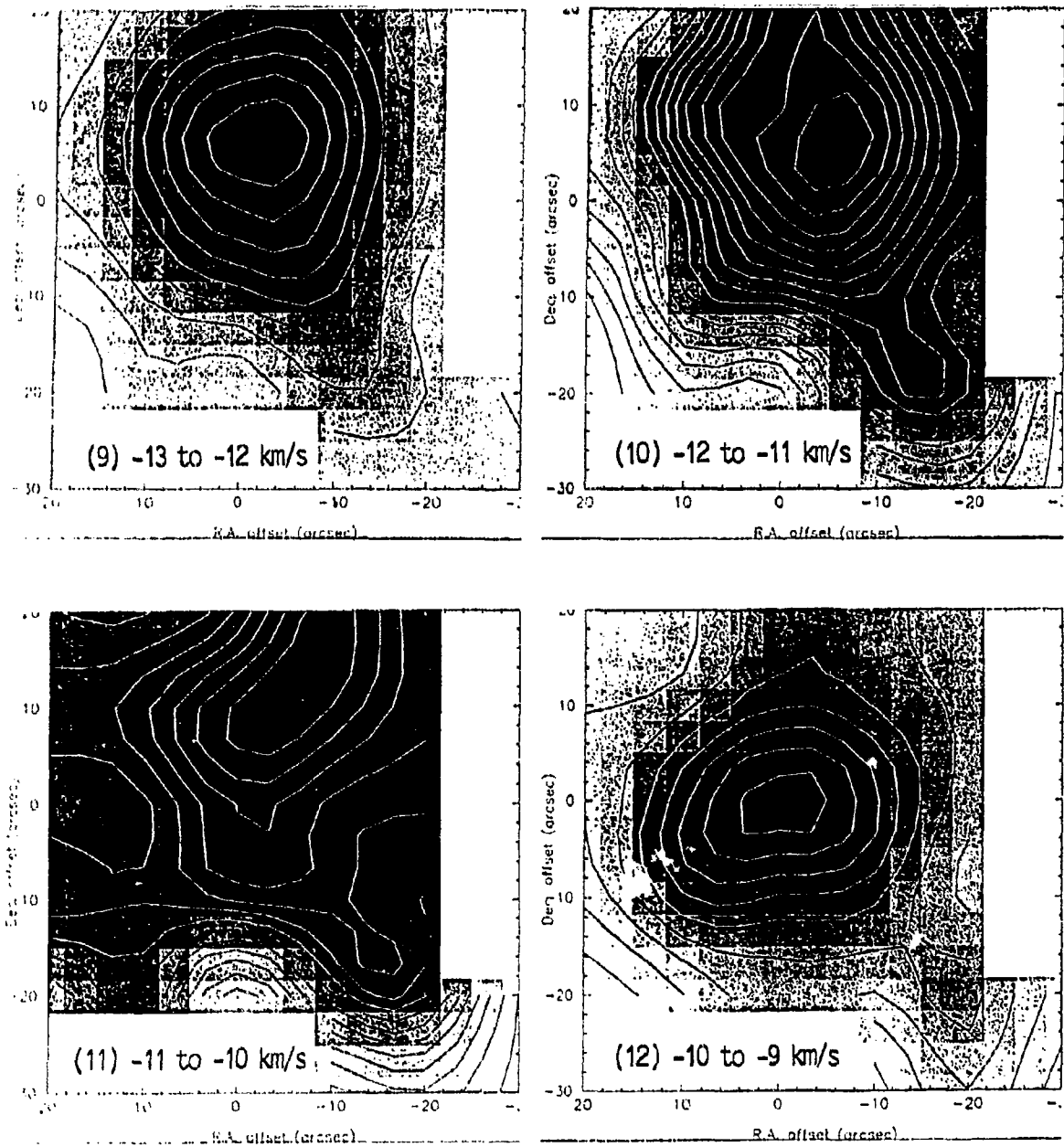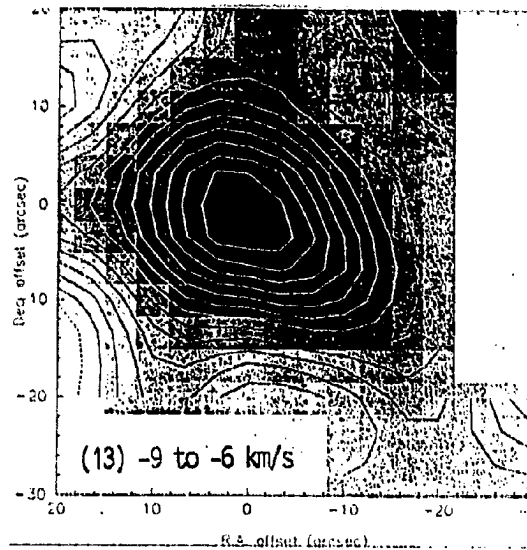
Fig. 16 (Continued)

TABLE 4

CONTOUR MAP PARAMETERS FOR FIGURE 16

MAP	CONTOURS (K·km s^{-1})		
	min	max	interval
1	-0.69	1.91	0.25
2	-0.26	0.98	0.10
3	-0.23	0.97	0.10
4	-0.38	1.16	0.10
5	0.05	1.56	0.10
6	0.19	2.85	0.25
7	1.11	5.90	0.50
8	2.49	7.47	0.50
9	2.00	6.50	0.50
10	1.21	2.84	0.10
11	0.56	2.05	0.10
12	0.07	1.87	0.20
13	-0.21	3.46	0.25

At V_{LSR} = -19 to -18 km s^{-1}, the ^{12}CO and ^{13}CO channel maps have similar appearances [Fig. 14(23) and Fig. 16(3)], both showing an extension towards the southwestern corner of the maps. There is a small displacement of the centroid of emission by about 8" for the ^{12}CO and ^{13}CO channel maps, which is not significant since the beam size is 15", almost twice as large as the displacement. The ^{13}CO channel maps from -18 to -12 km s^{-1} [Fig. 16(4) to Fig. 16(9)] show the emission peaks to be within 7" of (0,0). It is believed to correspond to the clump B4 seen in the ^{12}CO channel maps. However, the centroids of emission in these ^{13}CO channel maps are not coincident with their counterparts in the ^{12}CO channel maps. This difference in peak locations, if real, could be due to gases emitting at different transitions that are segregated spatially. At velocities from -12 to -11 km s^{-1}, Figure 16(10) shows a peak about 9" northwest of (0,0), while the ^{12}CO channel map is severely contaminated by the -11 km s^{-1} absorption feature seen in the spectra. At velocities from -11 to -10 km s^{-1} [Fig. 16(11)], the emission peak moves northward into an elongated feature. However, because of the small region mapped and the likelihood of self absorption near -11 km s^{-1}, the implication of this elongation is not clear. In the redshifted velocities, from -10 to -6 km s^{-1} [Fig. 16(12) and (13)], the intensity peaks at (0,0), which is consistent with the clump R3 seen in ^{12}CO.

(B) THE J = 6 → 5 TRANSITION

Figure 10 shows a spectral line map of the available data in the ^{12}CO J = 6 → 5 transition. The map consists of a nine point cross about (0,0) with 10" spacing, and a single spectrum at (-20,-20). The -13.5 km s^{-1} peak seen in ^{12}CO J = 3 → 2 can be seen throughout the J = 6 → 5 map, although in some lines the peaks are at -14 km s^{-1}, while at (0,-20) the peak is at -16.5 km s^{-1}. The -11 km s^{-1} absorption feature can also be seen in all spectra except at (-20,-20), where there is no emission detected at velocities greater than -12 km s^{-1} [Fig. 17(b)]. Similarly, the -11 km s^{-1} absorption feature is seen at a slightly

different velocity in each spectrum. The greatest difference is that the absorption is redshifted by 1.5 km s^{-1} at (-20,0) and (0,10), i.e. the absorption is located at -9.5 km s^{-1} instead of -11 km s^{-1}. Since observations for the J = 6 → 5 transition were done using chopping relative to a position 30" from the source, there is a possibility that self-chopping may have occurred causing the velocity variation described above. Therefore, the velocity shift may not be physically meaningful. At the position of GL 490, the total velocity extent of the J = 6 → 5 line, at zero intensity, is about 30 km s^{-1} [Fig. 17(a)]. The peak intensity across the ^{12}CO J = 6 → 5 spectral line map does not drop monotonically within 20" west and north of GL 490. For example, the peak antenna temperature first drops from 15.3 °K at the position of the source to 8.5 °K 10" west of the source and then rises again to 12 °K 20" west of the source.

A CO J = 6 → 5 spectrum was obtained at the centroid of the main blue clump B1 at (-20, -20). Only the strong blue wing exists in this spectrum. There is little emission in the J = 6 → 5 transition from the quiescent molecular gas. The remarkable shape of the CO J = 6 → 5 line at (-20,-20) is shown in Figure 17. The central spectrum is also shown for comparison. The quiescent gas (centred at -13 km s^{-1}) does not emit in the J = 6 → 5 transition at B1 either due to a drop in density below the critical density needed to excite the J = 6 → 5 transition or due to a drop in temperature. The presence of strong blueshifted emission in CO J = 6 → 5 implies that the outflowing gas is both very warm (T~100 °K) and very dense ($n_{crit} \geq 10^6$ cm^{-3}). A plausible mechanism is compression and heating of the gas by a shock.
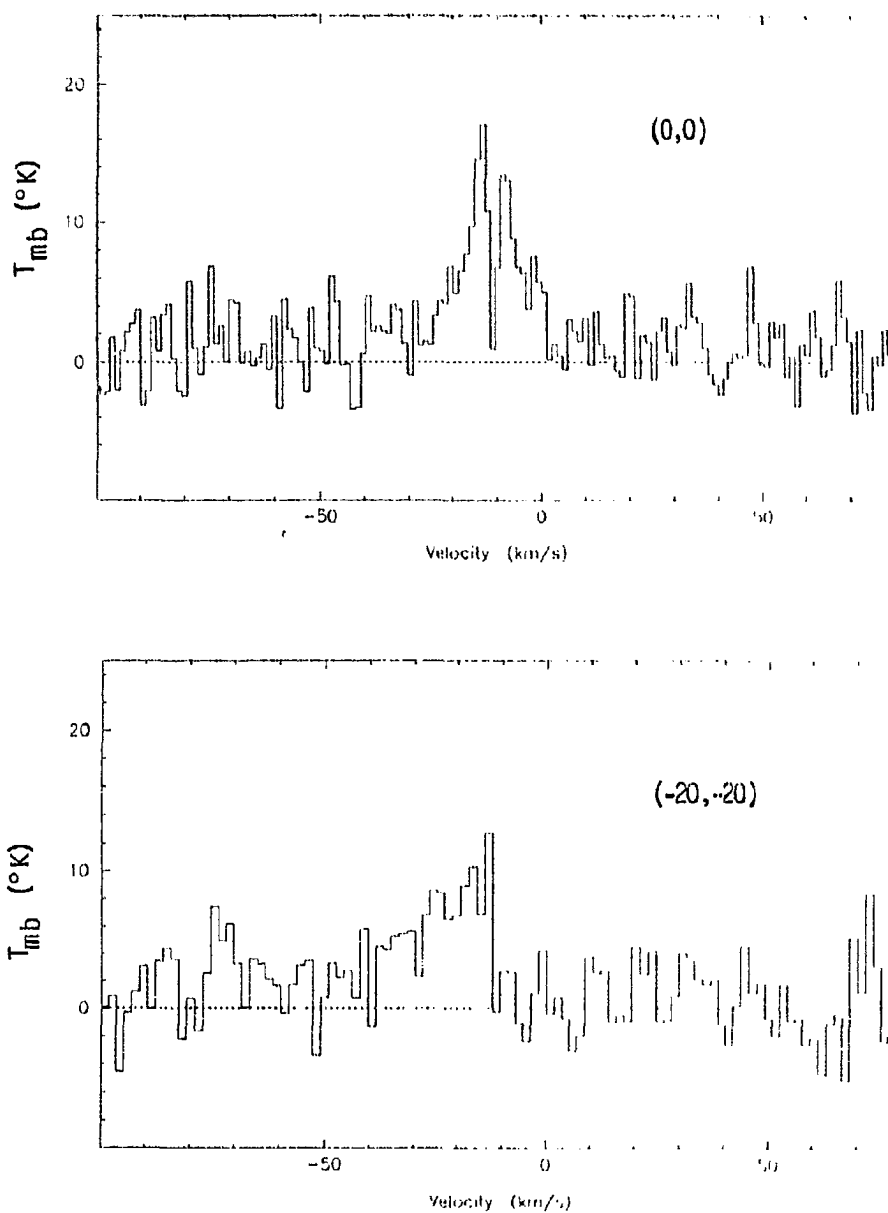
Fig. 17   Selected ^{12}CO J = 6 → 5 spectra. The map coordinates for each spectrum are given in arcseconds from GL 490. North and East are positive.

IV   Discussion

(A)   EXCITATION TEMPERATURES OF THE HIGH-VELOCITY GAS

(a)   The J = 3 → 2 Lines

The excitation temperatures for the $J = 3 \rightarrow 2$ emitting gas can be obtained by one of the two equations given in § IIB(a). Where the ^{13}CO line is not visible, the gas is assumed to be optically thin and the approximation that $\tau \ll 1$ is used, i.e., equation (31). Wherever ^{13}CO is detected (inner part of the line), the optical depth τ can be found using the line ratio $^{13}CO/^{12}CO$, and equation (18) can then be used to obtain the excitation temperature. It should be pointed out that when τ is large, the ratio $^{13}CO/^{12}CO$ approaches 1 and hence τ is poorly determined at the $\tau \gg 1$ limit.

Excitation temperatures calculated at the source position, (0,0), are shown plotted with respect to gas velocities in Figure 18. Since the equations derived in § IIB(a) are based on the assumption that excitation temperature is constant throughout the line, this plot allows us to assess the validity of the assumption. The dots in Figure 18 represent T_{ex} calculated using the $\tau \ll 1$ approximation and the crosses represent T_{ex} calculated using equation (18). The gap from -8 to -15 km s^{-1} is due to the self-absorption feature in the line, where excitation temperatures for the quiescent cloud cannot be obtained reliably. The error bars take into account the two uncertainties in obtaining T_{ex}, the noise in the spectra and the uncertainties in measuring the antenna temperatures. The 1 σ uncertainty in a spectrum is measured using one fifth of the peak-to-peak noise at the baseline of the spectrum. The noise in the spectrum and the measuring uncertainty are combined using the square root of the sum of their squares. The combined uncertainty is then used to find the uncertainties in T_{ex} contributed by the two error sources. As can be seen in Figure 18, the
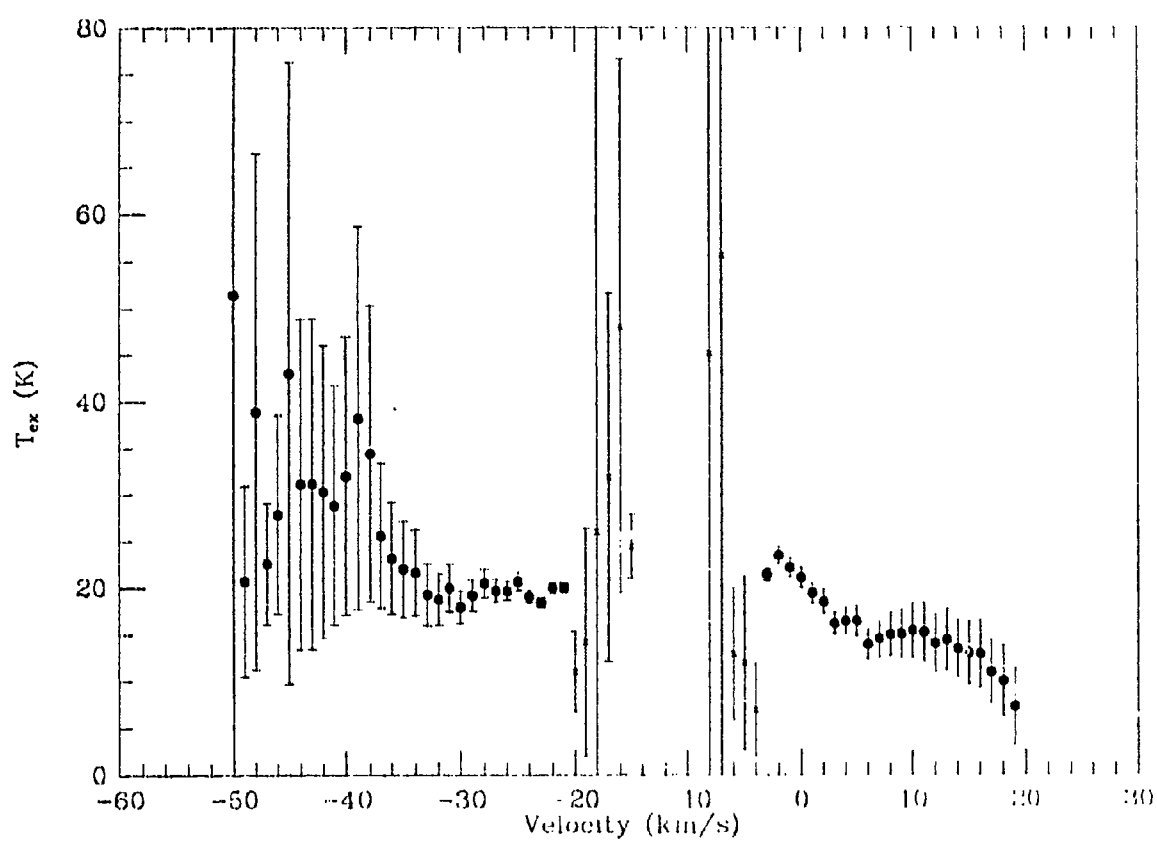
Fig. 18   Variation of excitation temperatures with V(lsr) for the CO J = 3 → 2 line at the position (0,0). Dots are temperatures calculated with the $\tau \ll 1$ approximation and crosses are temperatures calculated using the $^{12}CO/^{13}CO$ line ratio.

uncertainties in T_{ex} at the highest velocities are large. This is due to the low signal-to-noise ratio (S/N) at high velocities. The error bars for data points near the line centre are large as well, because the S/N ratios for the ^{13}CO spectra are low.

For (0,0) (Fig. 18), taking the uncertainties into account, we can see that T_{ex} at the blue wing is roughly constant around 20 °K. This excitation temperature agrees quite well with T_{ex} = 15 °K used by Snell et al. (1984) and T_{ex} found by Schella (1991). The red wing, however, shows a negative temperature gradient. The temperature in the red wing decreases from about 22 °K at -2 km s^{-1} to about 10 °K at +19 km s^{-1}. At an adjacent position, (-10,0), data at the high velocity end of the blue wing have large uncertainties which cause the excitation temperature to be poorly defined. At lower velocities, there is a possibility that T_{ex} decreases from ~35 °K to ~15 °K as velocity decreases. The temperature of the red wing shows a dip to ~15 °K and then a rise to ~27 °K, after which it gradually decreases to ~10 °K.

At the centre of clump B1, (-20,-20), the blue wing clearly shows a decreasing temperature towards higher velocities gas. The temperature ranges from about 30 °K to about 10 °K. The red wing shows that the temperature decreases from 12 °K to 6 °K towards higher velocities. At the centre of clump R1, (20,20), temperatures in the blue wing decrease from 15 °K to 10 °K as the velocity increases. The red wing temperature first increases from 20 °K to about 40 °K, then stays roughly constant at around 30 °K before finally dropping to 10 °K at higher velocities. At the centre of clump R2, (-20,20), the red wing shows a peak in temperature (~30 °K), and then drops to 12 °K for both higher and lower velocity gas. The blue wing does not show any clear trend due to the large uncertainties. There is a possibility that temperature decreases with increasing velocities here. From the above discussion, we conclude, therefore, that a uniform temperature gas is probably not strictly valid. However, this does not pose a significant

problem since the dependence of column density on excitation temperature is small for T_{ex} = 20 to 50 °K.

(b) The J = 6 → 5 Line.

Excitation temperatures for the J = 6 → 5 line at (0,0) are plotted against velocity in Figure 19. For this transition, the excitation temperatures are calculated using the optically thin case for the line ratio T(65)/T(32) (equation (32)). This procedure assumes that the gas has a uniform temperature. The error bars for the J = 6 → 5 data are typically larger than those for the J = 3 → 2 data due to a lower S/N (see Fig. 17). In the blue wing, the excitation temperature increases from 27 °K at -41 km s\u0001psi 1) to a peak of ~55 °K at -33 km s⁻¹, then decreases to ~35 °K near -22 km s⁻¹. There are only 4 data points on the red wing. They suggest that the temperature increases from 40 °K to ~50 °K towards high velocities. At (0,10), the excitation temperatures suggest that the temperature of the blue wing is about 55 °K. Due to the low S/N, no clear temperature gradient can be seen.

At (-20,-20), the blue wing suggests a possible increase in temperature from 50 °K to 100 °K towards higher velocities. This trend is opposite to that seen in the J = 3 → 2 line at the same position. The fact that higher temperatures are found for the J = 6 → 5 line while lower temperatures are found for the J = 3 → 2 lines indicates that the two different transitions sample different gas. Thus, the assumption of uniform temperature is not valid.

At (-20,0), the red wing is consistent with a constant temperature of ~40 °K. At (0,-20), the temperatures dervied for both red and blue wings increase towards higher velocities. The temperature range is ~50 °K to ~110 °K for the blue wing, and 35 °K to ≥ 80 °K for the red wing.
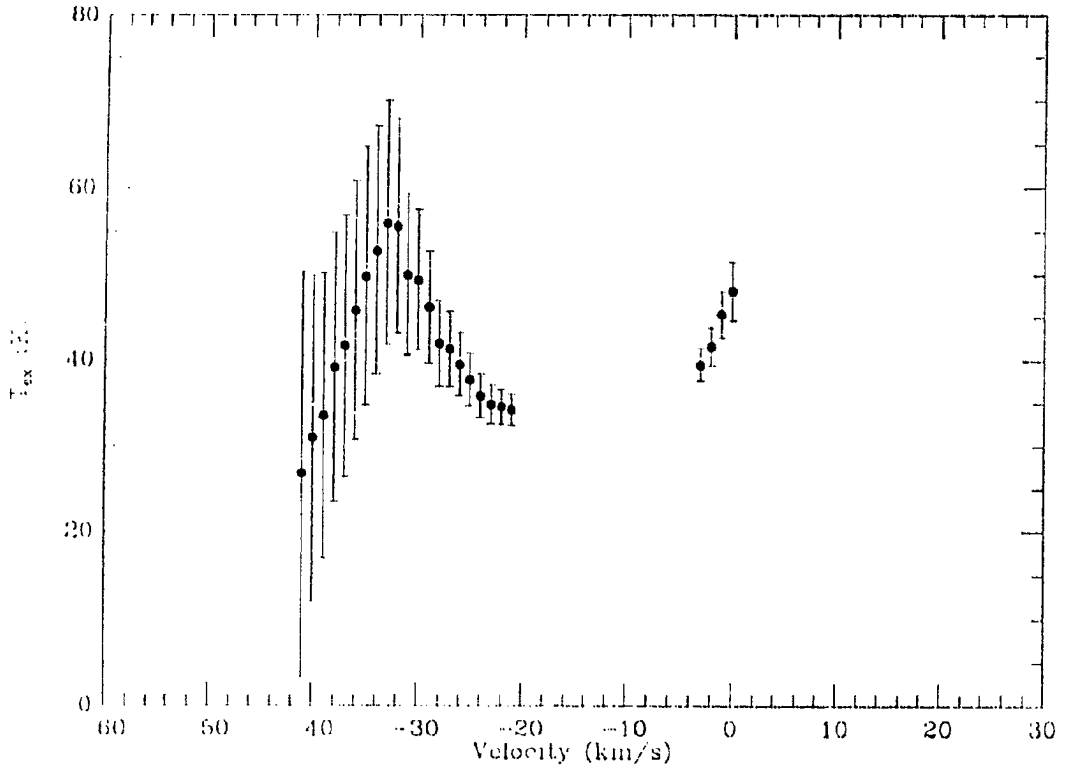
Fig. 19   Variation of excitation temperatures with V(lsr) for the CO J = 6 → 5 line at (0,0). T_{ex} is calculated using the line ratio of optically thin J = 6 → 5 to J = 3 → 2. The gap between V = -20 to +3 km s^{-1} is where the J = 3 → 2 line is optically thick and T_{ex} cannot be calculated.

Excitation temperatures for the $J = 6 \rightarrow 5$ lines may be indicating that T_{ex} near the main blue clump consisting of (-20,20) and (0,-20) are higher than temperatures near GL 490. This can be understood if the main blue clump consists of shocked gas and the high temperature results from a wind encountering the ambient gas.

(B)   MASSES OF THE MOVING CLUMPS

In calculating column densities (and masses), each spectrum at the positions listed in Table 3 is divided into 3 regimes: (1) when the optical depth cannot be obtained (i.e., the ^{13}CO line is not visible), T_{ex} is found by the $\tau \ll 1$ approximation and column densities are calculated with equation (37), (2) for the inner wings (i.e. low velocity emission), where the optical depths can be obtained but not the excitation temperatures (due to the lack of ^{13}CO $J = 2 \rightarrow 1$ data), T_{ex} has to be assumed [Equation (23) is used to find the column densities. Excitation temperatures can be calculated in this regime only at the position (0,0), where spectral coverage of the ^{13}CO $J = 2 \rightarrow 1$ line is available], (3) where optical depths are found to be so large that $e^{-\tau}$ is essentially negligible, T_{ex} can be found using the optically thick approximation, with equation (23) again used to find the column densities. (As mentioned before, τ in this regime is poorly determined because the line ratio approaches unity as τ becomes very large.)

When T_{ex} has to be assumed for the inner wing, a value of 20 °K is used. This value is consistent with the excitation temperature found by Snell et al. (1984) and Schella (1991). Although temperature gradients are found in the line wings, an accurate relation between T_{ex} and velocity cannot be predicted without higher S/N spectra. Here, we can estimate the error in column densities that an error in T_{ex} would produce. If the temperature decreases linearly from 20 °K to 10 °K over a 20 km s^{-1} interval, then,

assuming a constant temperature of 20 °K, we underestimate the column density by a factor of about 1.5.

At the position of GL 490, filling factors can be calculated explicitly. This is done by first obtaining the optical depths for the two transitions $J = 3 \rightarrow 2$ and $J = 2 \rightarrow 1$ using equation (7), then substituting the optical depths for the two transitions into equation (18) to obtain an excitation temperature. Finally, putting the optical depth of the $J = 3 \rightarrow 2$ transition and the excitation temperature into equation (6) yields the filling factor, f. Values of f are found to be between 0.6 to 3.5 at velocities from -20 km s^{-1} to -3 km s^{-1}, excluding velocities between -9 km s^{-1} and -15 km s^{-1} where the line core is located. The mean value is f = 1.5. Filling factors greater than 1 are not physically meaningful for a uniform temperature gas. We assume that, for the velocities stated above, f = 1. It should be noted, however, that filling factors greater than unity can be found from our formalism if there exists a spatial temperature gradient in the cloud (Cantó et al. 1987).

The masses of the high-velocity clumps given in Table 5 are calculated using the velocity intervals listed in Table 3. These masses are strictly lower limits for the following reasons: (1) due to contamination by the ambient molecular cloud emission and the absorption at -11 km s^{-1}, velocities near the line centre (from -15 to -8 km s^{-1}) are not included in the calculation of masses whenever encountered. This implies that the calculated masses are lower limits if the clump velocities overlapped with velocities near the line centre. For higher-velocity clumps, however, this contamination does not pose a problem; (2) the projected area of the clumps is usually taken to be the area of the beam (HPBW = 15" for the $J = 3 \rightarrow 2$ transition) for simplicity. The true extent of the clumps is larger than the beam area as seen from the velocity channel maps (Fig. 14), causing our mass estimates to be low. However, the velocity channel maps also show a rapid decrease in intensity away from the peak, which implies a density drop-off. Therefore, much of the

mass should be encompassed in the beam width. In order to estimate the fraction of mass of a clump outside the beam area, the column densities of the main blue clump (B1) are found at two positions 20" from the peak, at (-20,0) and (0,-20). The column density for only one velocity (at V_{LSR} = -25 km s^{-1}) is calculated for each of these positions. It is found that, at both positions, the column densities are less than half the column density obtained at the peak, (-20,-20), for the same velocity. Therefore, the mass calculated using the beam area is underestimated by at least a factor of 2. This uncertainty can be up to a factor of 7 if we assume a factor of 2 drop off in column density within the beam area and estimate the amount of beam area 'missed' in calculating the mass of the main blue clump.

The uncertainty in the calculation of masses depends on the column density-excitation temperature relation. In the optically thin regime, an increase of a factor of 3 in T_{ex} causes the column density to increase by only 1% if T_{ex} = 20 °K. In the $\tau \sim 1$ regime, however, a factor of 3 increase in T_{ex} leads to a factor of 4 increase in the column density, if T_{ex} = 20 °K. One of the largest uncertainties in the calculation of masses is in choosing the boundary velocities, which are somewhat arbitrary. All possibilities included, the true masses of these clumps should be within a factor of 10 of the estimates given in Table 5.

Clumpy bipolar outflows have been observed in several other sources, e.g. IRAS 16293 (Walker et al. 1988), Orion B (Richer et al., 1992), L1448 (Bachiller et al., 1990 and Bachiller et al., 1991a) and IRAS 03282+3035 (Bachiller et al., 1991b). Their masses and characteristics are listed in Table 6. In addition, Martín-Pintado et al. (1992) observed SiO emission and other high density tracers towards the molecular outflows in L1448, Bernard 1, NGC 2071 and Cepheus A. They found that the gas density in the shocked regions (from observations of SiO and SO) is typically a few times larger than that derived for the quiescent gas, indicating enhanced-density, shocked clumps in these molecular outflows. It is interesting to note that our CO J = 6 → 5 line profile at the main

TABLE 5

MASSES OF HIGH-VELOCITY CLUMPS

Clump	Mass ($\mathcal{M}_\odot$)
B1	0.2
B2	0.01
B3	0.02
B4	0.5
R1	0.08
R2	0.2
R3	0.3

blue clump, (-20,-20), is similar to the SiO line profiles found by Bachiller et al. (1991a) (see their Figure 1) and Martín-Pintado et al. (1992) (see also their Figure 1). Both line profiles show no emission arising in the ambient cloud. The emission stops sharply at the ambient cloud velocity. Bachiller et al. suggest that such a line profile is expected if the emission were generated in a strongly shocked gas. Therefore, it is possible that our clump B1 is also a shocked clump.

The origin of the high-velocity CO clumps (or bullets) is discussed in Bachiller et al. (1990). These authors suggest that the bullets have been ejected from the vicinity of the outflow source. Bachiller et al. propose that their observations can be explained by models of bipolar flows in which the wind originated from two sides of an accretion disk (Pudritz, 1985). This model can explain the ejection of two oppositely directed masses due to the instability of the accretion disk, which is tightly coupled across the width of the disk. Richer et al. (1992), however, propose that the clumps seen in the Orion B outflow may be formed locally from ambient molecular gas. After a radiative jet enters a cool molecular cloud, the shocked, swept-up gas cools rapidly forming a dense shell, which breaks up into clumps due to local hydrodynamic instabilities.

In the case of GL 490, the clumps seen in the $J = 3 \rightarrow 2$ channel maps are found to be more massive than clumps (or bullets) listed in other sources (Table 6). The clumps observed in GL 490 are clearly not well aligned. There appear to be two red-blue pairs in the outflow, the main blue clump (B1) and the eastern clump in the main red lobe (R1) and the clumps B4 and R3 at the position of GL 490. B1 and R1 are located almost symmetrically opposite of GL 490, confirming it to be the source of the outflow. The other clumps however, are scattered around GL 490. The spatial distribution of clumps in GL 490 is difficult to understand with the ejected bullet model. A disk-like structure may exist around GL 490, as has been seen in observations of CS, and this implies a possible

TABLE 6

MASSES AND CHARACTERISTICS OF CLUMPS

IN OTHER BIPOLAR OUTFLOWS

Source	No. of Clumps	Alignment of Clumps	Masses of clumps $(\mathcal{M}_\odot)$	Red/Blue Pair	Collimation of Outflow
L1448/IRS3	8	Well-aligned	a few$\times10^{-3}$	Yes	Well-collimated
IRAS 03282 +3035	7	Not Perfect alignment	a few$\times10^{-4}$	Yes, except for 1 clump	Highly-collimated
Orion B	≥4	Well-aligned	≤ 0.01	No	Highly-collimated
ρ Oph A	≥ 6	Well-aligned	$\sim 10^{-3}$	Yes	Highly-collimated
IRAS 16293	9	Not aligned	10^{-3} to 3×10^{-2}	Not Apparent	-
GL 490	>7	Not aligned	0.01 to 0.5	B1 and R1 only	Low collimation

accretion disk as needed in the ejected bullet model. However, according to Kawabe et al. (1984), this disk cannot be collimating the bipolar outflow because the expanding momentum of the CS cloud is less than the outward momentum of the CO bipolar outflow. It is not clear whether the model proposed by Richer et al. (1992) can be applied to the observations here without a more detailed investigation. The lack of alignment for all the clumps may imply, for example, a precessing disk.

In order to estimate the relative density of clumps with respect to the surrounding molecular cloud region, column densities of regions outside clumps R1, B1 and B3 have been estimated. If the projected area of these regions are chosen to be one beam width, then the relative number density is simply the quotient of the column density of the clumps and the column density of the surrounding region. For clumps R1, B1 and B3, at positions (-20,20), (20,20) and (0,0), their respective velocity ranges were used to find the column densities. Relative densities were found to be 5, 7 and 2, respectively. The assumption made here is that the excitation temperature remains constant in the region mapped with the J = 3 → 2 transition. Although warmer postshock gas is certainly present, as shown by the CO J = 6 → 5 emission at (-20,-20), the bulk of the gas is probably cool, as shown by CO J = 3 → 2 and J = 2 → 1. In other words, the intensity peaks seen are not due to a temperature effect, but are a density effect. With the average of the relative densities calculated above, it seems that the clumps observed in GL 490 are about a factor of 5 denser than the surrounding molecular cloud region. This density enhancement of the clumps relative to the surrounding regions probably represents the true "clumpiness" of the outflow. Although the excitation temperatures calculated suggest a temperature gradient dependent upon gas velocity, the range in temperature of 20 to 50 °K affects the column density by only 8%, which is insufficient to explain the high contrast in column density between the clumps and the surrounding regions.

In order to assess the dynamical importance of the clumps to the molecular cloud core, the mass of the molecular cloud core within the region mapped by our ^{12}CO J = 3 → 2 observations has to be estimated. For simplicity, an average number density, ñ, of the cloud is assumed. A power law (e.g., n(r) ∝ $1/r^2$) is also physically reasonable, but will lead to a singularity when integrated from the centre of the cloud. The average number density is given by ñ = N/R, where N is the column density of the cloud and R is the assumed radius of the cloud. The region around GL 490 mapped by us is about 1.4 (0.4 pc at a distance of 1 kpc) in radius. Higher angular resolution CS observations of GL 490 by Kawabe et al. (1984) indicated that the size of the compact CS cloud is about 60"×30", which implies that the higher density gas is encompassed in the region mapped by us.

Estimates of total cloud mass were obtained using column densities derived from various studies. From infrared absorption spectroscopy by G. F. Mitchell, the column density can be derived using the curve-of-growth analysis outlined in § II(B)b. The result is N(^{13}CO) = 5.6×10^{16} cm^{-2} [for the low temperature component, T = 24 °K - see (b) below]. This value reflects only the foreground absorbing gas, so if a spherical geometry is assumed, the total ^{13}CO column density should be doubled. For a ^{13}CO to H_2 abundance ratio of N(^{13}CO) = 1.7×10^{-6} N(H_2) cm^{-2}, the total H_2 column density is found to be 4.5×10^{22} cm^{-2}. This column density, together with the assumed radius of 0.4 pc, gives a mean gas density of 3.8×10^4 cm^{-3} and a cloud mass of 450 $\mathcal{M}_\odot$.

Kawabe et al. (1984) obtained an estimate for the hydrogen density in the CS cloud using the large velocity gradient (LVG) approximation. They found the hydrogen density towards GL 490 to be in the range 3×10^4 to 3×10^5 cm^{-3}. Although the derived density is for a region smaller than that adopted here, it is nevertheless instructive to apply it here to gain a feeling for the lower limit to the cloud mass within 0.4 pc of GL 490. With ñ =

3.5×10^4 cm^{-3}, the dervied mass of the cloud is 420 $\mathcal{M}_\odot$, which agrees well with the IR absorption result.

Gear et al. (1986) mapped the 350 μm (857 GHz) emission from the GL 490 cloud using a beam size of 55". They estimated the source size to be 70"$\times$30", similar to the size of the CS cloud found by Kawabe et al. (1984). Using the relations between τ_{350} and n(H$_2$) derived by Hildebrand (1983), they found a hydrogen column density of 3.6×10^{22} cm^{-2}, which gives a mass of 360 $\mathcal{M}_\odot$ using R = 0.4 pc.

Averaging the masses obtained from the three sets of observations above, we find the mass of the molecular cloud to be about 410 $\mathcal{M}_\odot$. The sum of the masses of all clumps in Table 5 amounts to 1.3 $\mathcal{M}_\odot$, which is only about 0.3 percent of the total mass confined within a radius of 0.4 pc. From Mitchell et al. (1992), the mass of the blue outflow lobe is 3.9 $\mathcal{M}_\odot$ and the total outflow mass is 8.7 $\mathcal{M}_\odot$. Hence the most massive clump observed here, at 0.5 $\mathcal{M}_\odot$, is about 13% of the mass of the blue lobe and 6% of the total outflow mass. It therefore appears that the clumps seen are not dynamically significant components.

At a distance of R = 0.15 pc from the source, where the peak of the blue lobe is located (without correcting for projection effects), the escape velocity can be calculated using the Newtonian equation $V_{escape} = (2GM_{0.15}/R)^{1/2}$, where $M_{0.15}$ is the mass of the cloud within 0.15 pc. This last value can be expressed as 37% of the mass within 0.4 pc calculated previously, i.e. 150 $\mathcal{M}_\odot$, under the assumption of a uniform density cloud. The calculated escape velocity is therefore 1.8 km s^{-1}. It is clear that the clumps cannot be gravitationally bound to the parent cloud. If an inclination angle of θ is taken into account, then the radius becomes R(sec θ), which leads to larger true velocities and strengthens the above conclusion.

(C)   HOT QUIESCENT GAS

The analysis in § II(B)b has been applied to the ^{13}CO v = 0 → 1 absorption lines found in the 4.7 μm spectrum of GL 490. If LTE is a valid approximation, then the Boltzmann equation $N_J/(2J+1)$ = constant × exp($-E_J/kT$) can be applied. A plot of $\ln|N_J/(2J+1)|$ versus ($-E_J/k$) should yield a straight line, with the gas temperature being obtained from the inverse of the slope of this line. Figure 20 shows the ^{13}CO column densities in each rotational sublevel as a function of the rotational energy. It is evident that the distribution of points has a break at $-E_J/k \approx 50$ °K. A linear least-squares fit to the low J points gives a rotational temperature of T = 24 °K for J ≤ 4. For higher rotational states, J ≥ 5, a straight line with gas temperature T = 107 °K fits well. From Figure 20, then, it appears that the molecular cloud has both a cooler (T = 24 °K) and a warmer (T = 107 °K) component. The temperature of the T = 24 °K component agrees quite well with the temperature of 20 °K for the molecular cloud found by Plambeck et al. (1983) using ^{12}CO J = 2 → 1 and J = 1 → 0 transitions. Since collisional excitation of the J = 6 level requires gas temperatures of about 116 °K above ground level, and the J = 6 → 5 transition has a critical density of $\sim 10^6$ cm^{-3} in optically thin gas, the detection of ^{12}CO J = 6 → 5 emission in the region of GL 490 is an indication that hot, dense gas exist in the cloud. It is reasonable to assume that the emission seen in the ^{12}CO J = 6 → 5 transition is produced by the 107 °K component of the cloud.

The size of the J = 6 → 5 emitting region can be estimated as follows. For a multi-component beam with Gaussian geometry, the equivalent main beam efficiency (i.e., coupling between beam and source) is given by

$$\frac{T_A^*}{T_R} = \eta_{mb} \cdot \frac{\sum_i a_i \theta_i^2 f_i \omega_i(s)}{\sum_i a_i \theta_i^2}, \tag{46}$$
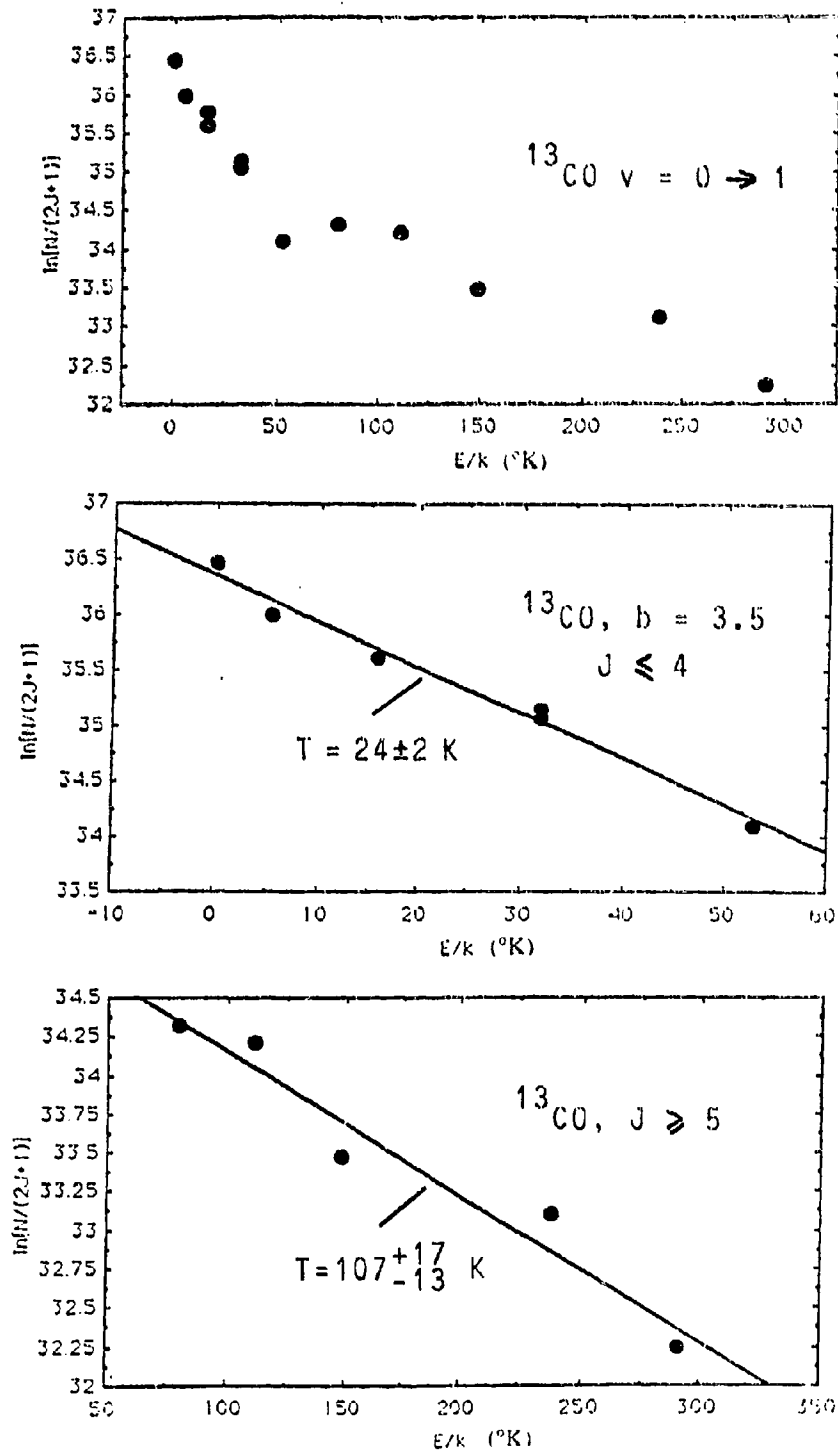
Fig. 20 (a). ^{13}CO column densities in each rotational sublevel are plotted as a function of the rotational energy for the absorption lines at the molecular cloud's velocity $(V_{LSR} = -13.5 \text{ km s}^{-1})$. (b) Shows the same data as in (a) but for rotational energy $E/k < 60$ °K, and (c) shows data for $E/k > 60$ °K.

from equation (20) in A. I. Harris (1990). In the above equation,

T_A^* is the antenna temperature corrected for atmospheric and telescope losses, and sideband imbalance,

T_R is the source radiation temperature,

η_{mb}' is the equivalent main beam efficiency for the composite beam,

a_i is the peak power amplitude of the i'th Gaussian beam,

θ_i is the angular width of the i'th Gaussian beam,

f_i is the geometrical filling factor in the i'th beam,

$\omega_i(s)$ is the off-centre weighting factor normalized so that $\omega_i(s=0) = 1$,

s is the position off-centre from the source in arcseconds.

Since the observed temperature using receiver G is the main beam temperature, T_{mb}, some modifications have to be made to equation (46). The relationship between the source radiation temperature and the main beam temperature can be written as

$$T_{mb} = f' T_R,$$ (47)

Using equation (5), i.e. $T_R = \dfrac{T_A^*}{\eta_B f}$, and equation (47) above, we have

$$\frac{T_{mb}}{T_R} = \frac{\sum_i a_i \theta_i^2 f_i \omega_i(s)}{\sum_i a_i \theta_i^2}.$$ (48)

In equation (48), if we assume the ^{12}CO J = 6 → 5 transition to be optically thick, then T_R is calculated using equation (39), i.e. $T_R = \dfrac{h\nu/k}{e^{h\nu/kT_{ex}} - 1}$. This gives $T_R = 91.3\ ^\circ K$ for T_{ex} = 107 $^\circ K$, the excitation temperature of the warm component found from the IR absorption data.

At the time of these observations, the JCMT beam was well-fit by two components, a 7" main beam (θ_1) and a broader component of 30" width (θ_2). The peak amplitudes of the two components were $a_1 = 0.3$ and $a_2 = 0.7$. The values of f_i and $\omega_i(s)$ are given by equations (22) and (24), respectively, in A. I. Harris (1990). They are

$$f_i = \frac{\theta_s^2}{\theta_s^2 + \theta_i^2} \, , \qquad (49)$$

and

$$\omega_i(s) = \exp\left[-\ln 2 \left(\frac{s^2}{\theta_s^2 + \theta_i^2}\right)\right] , \qquad (50)$$

where θ_s is the FWHM diameter of a Gaussian source.

Values of T_{mb} were calculated with the above equations for $T_R = 90\ °K$ for various source sizes ($\theta_s = 5"$ to 50") at $s = 0"$, 10" and 20" and the results are shown in Table 7. By comparing the observed main beam peak temperature at (0,0), (0,-10) and (0,-20) from the $^{12}CO\ J = 6 \rightarrow 5$ spectra with T_{mb} in Table 7, we found that $T_{mb}(0") = 15.5\ °K$ and $T_{mb}(10") = 14.2\ °K$ for $\theta_s = 13"$ and $T_{mb}(20") = 8.2\ °K$ for $\theta_s = 11"$ fit the observed peak antenna temperatures well. Therefore, we conclude that the region of CO $J = 6 \rightarrow 5$ emission is ~11" - 13" in diameter (FWHM), corresponding to 11,000 to 13,000 AU at a distance of 1 kpc.

If the $J = 6 \rightarrow 5$ transition is optically thin, a similar technique to the one applied above shows that the source size must increase accordingly. For example, if $\tau = 0.5$, then the size is 17" to 20" FWHM, roughly a 50% increase. Also, it is assumed here that this region is spherically symmetric, which is probably not strictly true as it was already

TABLE 7

PREDICTED MAIN BEAM TEMPERATURE

FOR VARIOUS SOURCE SIZES

$a_1 = 0.30$ $a_2 = 0.7$ $\theta_1 = 7''$ $\theta_2 = 30''$ $T_R = 90\ °K$			
θ_s (arcseconds)	$T_{mb}(0'')$ ($°K$)	$T_{mb}(10'')$ ($°K$)	$T_{mb}(20'')$ ($°K$)
5	3.07	2.48	1.78
6	4.25	3.53	2.55
7	5.57	4.73	3.45
8	·7.00	6.06	4.48
9	8.54	7.52	5.63
10	10.17	9.07	6.88
11	11.88	10.71	8.23
12	13.66	12.42	9.67
13	15.50	14.19	11.17
14	17.37	16.00	12.74
15	19.28	17.85	14.36
17	23.13	21.60	17.70
20	28.89	27.22	22.85
25	37.95	36.16	31.31
30	45.92	44.12	39.15
50	66.68	65.32	61.41

mentioned in § III(B) that the peak intensities in the J = 6 → 5 spectra do not drop-off symmetrically.

Knowing the size of the J = 6 → 5 emission region allows us to find the average number density within this warm region. The ^{13}CO column density obtained from IR absorption data for the 107 °K warm component is $N(^{13}CO) = 1.38\times10^{17}$ cm^{-2}. This corresponds to $N(H_2) = 8.3\times10^{22}$ cm^{-2}. The average number density is given by the H_2 column density divided by the radius of the region, which is known from the previous calculation to be 6000 AU (or 9×10^{16} cm). This gives a value of $\bar{n} = 9.2\times10^5$ cm^{-3}. It is natural to seek agreement between this value and the number density obtained directly with the IR absorption data. The number density can be obtained using the IR absorption data by fitting theoretically-calculated rotational CO populations per sublevel with the observed values (e.g. Mitchell et al., 1989). On the assumption that the lines are optically thin, a density for the warm component of n ≥ 10^7 cm^{-3} is implied. This value is larger than that obtained using the size of the warm region. The apparent discordance may be reconciled by the fact that the lines are not completely optically thin (τ is found to be between 0.5 and 1.75), so a lower density will suffice to produce the observed level populations. A more elaborate calculation, including radiation transfer as well as the solution of the statistical equilibrium equations, is needed to verify this.

One possibility of maintaining a high (100 °K) gas temperature is by gas-grain collisions. Infrared radiation from the source heats the dust grains near the core. In a high density cloud like GL 490(~ 10^6 cm^{-3}), collisions between molecules and dust grains occurs frequently, resulting in a high temperature gas.

Takano (1986) derived the relation

$$T_d = 70 \left(\frac{2 \times 10^{17} \text{ cm}}{r} \right)^{2/5} \left(\frac{L}{10^5 L_\odot} \right)^{1/5}$$

by balancing the heat gain from absorption of the full stellar radiation against the radiation from the dust grains. In the above equation, T_d is the dust temperature, r is the distance from the central heat source, and L is the luminosity of the source. The dust temperature in the above equation is an upper limit because the model assumes that no intervening opacity between the central source and the grains. The gas temperature near an infrared source is expected to be lower than the dust temperature in order for energy to be transferred, hence the above equation is also an upper limit for the gas temperature. Using this relation, we find that at 6000 AU (the radius of the warm region), the upper limit of the gas temperature is 40 °K. It should also be noted that the above relation is based on the assumption that the dust cloud is optically thin at all wavelengths. This is clearly unrealistic since the dust opacity is usually high at wavelengths blueward of near-infrared. According to Scoville and Kwan (1976), reradiation from dust grains plays an important role in heating the dust in an optically thick cloud. Our result for the upper limit to the gas temperature, therefore, is not strictly applicable because the estimated radius of the warm region was obtained using the optically thick line core.

Since the upper limit obtained above is less than 40 °K, additional heat sources for the GL 490 cloud may have been overlooked. The possibility of an external heat source is rather unattractive because the intensity of the $J = 6 \rightarrow 5$ emission weakens markedly over distances of 20" from the central source, indicating that no external heat source is in the vicinity.

(D)   THE OUTFLOW COMPONENT SEEN IN ABSORPTION

Figure 11 (p. 37) shows the existence of a strong infrared absorption component blueshifted by 13 km s^{-1} with respect to the quiescent cloud. It is natural to interpret this blueshifted feature as due to outflowing gas. In ^{12}CO absorption, this feature is found to be saturated, so no column density can be obtained. On the other hand, no ^{13}CO absorption is detected for this component so that an upper limit to the density can be found.

The minimum equivalent width, W_{min}, is defined to be

$$W_{min} \text{ (cm}^{-1}) \sim \frac{\text{Resolution (cm}^{-1})}{S/N}.$$

The resolution of the infrared observations is 0.049 cm^{-1}, and the signal-to-noise (S/N) ratio at the 1σ level is 10. Hence $W_{min} = 0.005$ cm^{-1}. The Doppler broadening parameter is b = 3.5 km s^{-1}. From equation (43)

$$F(\tau_0) = \frac{W_\omega}{\omega} \frac{c}{2b}$$

$$= 0.10,$$

where $\omega = 2120$ cm^{-1} is the central frequency of the observed range. This value of $F(\tau_0)$ gives $\tau_0 = 0.12$ from the tables for the curves of growth for a Maxwellian velocity distribution (Spitzer, 1978). Using equation (44), we find

$$N_{J=1} = \frac{b \tau_0}{0.015 \lambda f}$$

$$= 7.7 \times 10^{14} \text{ cm}^{-2}.$$

where $f = 7.614 \times 10^{-6}$ and $1/\lambda = 2103.3$ cm^{-1} for the ^{13}CO v $= 0$-1 R1 line [i.e. the (0,1) to (1,2) transition]. The total column density, N_{tot}, can be found by applying the partition function as described in § II(B)a, and is given by 3.0×10^{15} cm^{-2}, for $T_{ex} = 24$ °K.

Since the ^{13}CO line is not detected, the total column density obtained here is an upper limit. However, because the ^{12}CO line is saturated, the ^{13}CO line is probably on the verge of being detectable. Therefore, it is believed that the above column density for the outflowing gas at -13 km s^{-1} with respect to the velocity of GL 490 may, in fact, be a reasonable estimate, even though it is an upper limit.

Using an abundance ratio of ^{12}CO to ^{13}CO of 60, we find $N(^{12}CO) \le 1.8 \times 10^{17}$ cm^{-2}. The total column density for ^{12}CO can also be obtained from the J $= 3 \to 2$ emission at the position of GL 490. The velocity range used will be based on the observed velocity width of the infrared absorption feature ($\Delta v_{1/2} = 1.667 \times b = 6$ km s^{-1}), centred on the outflow velocity ($V_{LSR} = -26$ km s^{-1}), i.e. the velocity interval of $V_{LSR} = -23$ to -29 km s^{-1}. $N(^{12}CO)$ is found to be 2.6×10^{16} cm^{-2} based on the emission data.

The two column densities derived from the IR absorption and CO emission data are consistent, since we only obtained an upper limit to the IR absorption column density. This consistency is in agreement with the scenario of a large-scale, expanding shell of ambient gas accelerated by a wind, in which case we should expect to obtain a similar column density whether we use either the IR absorption or the millimetre line emission. On the other hand, as mentioned previously, the IR upper limit is probably close to the actual column density of the outflow gas. In this case, the results from the IR absorption and the ^{12}CO emission differ by a factor of up to 7. The amount of outflowing gas seen in absorption, if close to the upper limit of 1.8×10^{17} cm^{-2}, should have been seen as an enhancement to the millimetre emission. The fact that no individual emission spike is

detected at the absorbing outflow velocity implies that the outflowing gas seen in absorption is probably not the same gas that produces the emission lines. Mitchell et al. (1991b) suggested a plausible explanation for the non-detection of the outflow gas in emission, namely that the absorbing gas may be so close to GL 490 that only a small fraction of the 15" beam is filled.

(E) COMPARING OBSERVATIONS WITH EXISTING MODELS

From the velocity channel maps in Figure 14, it is clear that the structure of the GL 490 outflow is clumpy and complex. In the following, we shall argue qualitatively the merits and problems of two possible outflow models for the GL 490 region.

(a) The Momentum-Conserving Shell Model

The model constructed by Shu et al. (1991), which depicts a neutral wind moving into the ambient cloud sweeping up a shell of molecular material, is outlined in § I(C). This particular model has certain attractive attributes when applied to the GL 490 outflow. First, the observed CO velocity ($\sim$30 km s^{-1}) is roughly consistent with the terminal velocity predicted in the model (of the order of 10 km s^{-1}). Second, the distribution of clumps may be explained by the break up of the post-shocked cooling shell if the opening angle of the wind is large. Third, the upper limit to the infrared absorption column density agrees with the CO emission column density. This is consistent with the shell model. It should be noted, however, that if the upper limit of the infrared absorption column density is close to the true column density, then the absorbing gas must be very close to the central source, as described in the previous section. In this case, the shell model cannot be used to explain the observations.

On the other hand, an ionized wind is observed by Simon et al. (1981a) to originate from GL 490. Simon et al. deduced a mass loss rate which is two orders of magnitude lower then that derived from CO emission. This fact implies that the ionized wind cannot be the cause of the outflow. It is possible that neutral gas may be the main constituent of this wind, which would argue in favour of the shell model.

Another argument against the Shu et al. model is that the predicted "Hubble Law", is not observed in the GL 490 flow. The "Hubble law" for the expansion of the shell states that the expansion speed is larger in those directions where the shell has progressed farther. The largest CO linewidth is observed at the position of GL 490 [i.e. at (0,0)], contradicting the prediction that higher velocity gas travels the furthest from the source. Finally, no cavity created by the wind is observed near GL 490, throwing some doubt on the existence of a neutral wind.

If the opening angle of the wind is small so that it is jet-like, the result is an entrained ambient gas scenario. The picture of a fast neutral jet moving into the ambient gas has been applied by Richer et al. (1992) to the Orion B outflow. These authors envisage clumps forming when the dense shell at the working surface and along the side of the jet breaks up. This model predicts a time scale of a few $\times 10^4$ years if the ambient gas density is $10^5 - 10^6$ cm^{-3}. Both of these properties are found in GL 490. However, there is no indication of the existence of a jet, nor is there evidence of a channel created by the jet. In addition, the model predicts a series of clumps more or less aligned close to the flow axis. This is clearly not the case in the GL 490 outflow.

(b)   The Ejected Clumps Model

The idea of the clumps being "bullets" ejected from the immediate vicinity of the central source is outlined in § I(C). One major problem in applying this model to the GL 490 flow is that the expected alignment and pairing of the clumps is not observed.

We now consider whether the clumps in GL 490 will survive without dispersing in their observed lifetimes. The lifetime of a clump is obtained using the simple equation

$$\text{lifetime} = \frac{\text{Distance of clump from GL 490}}{\text{Mean velocity of the clump}} \cdot$$

Using the information in Table 3, we find the lifetimes of the clumps to be $\lesssim 10^4$ years. If we assume that each clump is a spherical body bound only by its own gravity, then the gravitational potential energy is

$$E_{grav} = -\frac{3}{5}\frac{GM^2}{R} \, ,$$

where M and R are the mass and radius of the clump, respectively. We find E_{grav} to be about 6×10^{40} ergs for $M = 0.2 \, \mathcal{M}_\odot$ and $R = 0.15$ pc (the values for clump B1). The bulk internal energy (due to the velocity of the molecules in the clump) is $E_{int} = \frac{1}{2}M\bar{V}^2$, where $\bar{V}$ is the mean molecular speed in the clump. E_{int} is found to be 2×10^{44} ergs for $\bar{V} = 10$ km s^{-1}. Although the calculations made here are over-simplified, the large difference between the two energies leads us to the conclusion that the clumps are probably not stable against dispersion. We can also estimate a dispersion timescale for a clump using the sound crossing time,

$$t_s = \frac{\text{Radius of clump}}{\text{Sound speed}} \cdot$$

If we use the beam size (15") as an estimate of the clump size and a sound speed of 1 km s^{-1}, then t_s is ~ 7×10^4 years. This timescale is almost an order of magnitude longer than the estimated lifetimes of the clumps. Therefore, it is indeed possible for the clumps to survive under these conditions.

The ejected clumps scenario will produce observed blueshifted absorption lines if the absorption originates very near the central source. The circumstellar disk required in this model may exist around GL 490. However, according to Gear et al. (1986), this large disk is incapable of collimating the outflow associated with GL 490.

In conclusion, our observations appear to be fairly consistent with the shell model proposed by Shu et al. (1991). An attempt to detect the required neutral wind would be very useful for constraining the GL 490 outflow to this particular model.

V. Summary

In this thesis, the high-velocity bipolar molecular outflow source GL 490 has been observed in five CO transitions: the ^{12}CO and ^{13}CO J = 2 → 1 and J = 3 → 2 transitions as well as the ^{12}CO J = 6 → 5 transition. Data obtained by IR spectroscopy are also available for analysis. The purpose of this project is to probe the physical environment in the cloud where GL 490 is embedded as well as the nature of the bipolar outflow.

The results of our study can be summarized as follows:

1.   The ^{12}CO J = 3 → 2 spectral line map shows that broad wings to the line profiles occur within 40" of GL 490. In the south-east direction, broad line wings vanish rather abruptly, indicating a sudden change in physical environment in this region. The strong wings in the line profiles display marked changes across the map region. Strong blue wings are found in the south-west while strong red wings are found to the north-east and north-west of GL 490.

2.   An absorption feature at -11 km s^{-1}, seen in all ^{12}CO J = 3 → 2 spectra near GL 490, can be caused by either an unrelated foreground cloud or by the outer and cooler part of the molecular cloud.

3.   Velocity channel maps made from the ^{12}CO J = 3 → 2 spectral line maps show several intensity peaks (clumps). Positions for the most prominent clumps are listed in Table 3. In particular, the main blue clump has a fan-shape and is centred at (-20,-20). The main red emission consists of two equally intense clumps located at (20,20) and (20,-20). The Clump called B2 (see Table 3) appears to move westward with decreasing velocity, possibly indicating a decelerating flow. The location of the centroid of clump R2

appears to trace an arc as the velocity changes. The implication of this movement is not clear presently. The centres of clumps R1 and B1 are symmetrically located on either side of GL 490. This red-blue pair of clumps resembles the well-aligned outflow clumps observed in other sources. However, the other clumps are neither aligned nor have a red/blue counterpart on the other side of GL 490. This misalignment of clumps may be the result of a precessing disk around GL 490.

4. In the ^{13}CO J = 3 → 2 channel maps, the centroid of emission of clump B4 appears to be slightly offset from that in the ^{12}CO map. If real, this could be due to the spatial segregation of the ^{12}CO emitting gas from the ^{13}CO emitting gas.

5. The ^{12}CO J = 6 → 5 spectral lines peak at a velocity of -13.5 km s^{-1}, which agrees with the results found for the lower transition lines. The -11 km s^{-1} absorption feature is also seen in the J = 6 → 5 transition. The peak intensity across the ^{12}CO J = 6 → 5 spectral line map does not drop off monotonically within 20" of GL 490. This indicates that the physical environment is not spherically symmetric about GL 490. At (-20,-20), the strongest blue clump, only a strong blue wing exists in the J = 6 → 5 spectrum. There is little emission from the quiescent gas. This spectral line profile is similar to the profiles of SiO lines seen in the outflow source L1448, in that the quiescent gas does not emit in the J = 6 → 5 transition. According to Bachiller et al. (1991a), this is the signature of strongly shocked gas.

6. Excitation temperatures for the blue wing of the emission at (0,0) are roughly constant at 20 °K, while temperatures decrease with velocity for the red wings of the profiles. At the centroid of the main blue clump, the temperature of the blue wing emission decreases at higher velocities. Excitation temperatures derived for the J = 6 → 5 lines show large scatter due to a low S/N ratio. The average temperature derived for the J = 6 →

5 lines is higher than the average temperature for the J = 3 → 2 lines, indicating that the two different transitions originate in different gas. The excitation temperature dervied for the region near clump B1 appears to be higher for the J = 6 → 5 transition. This high temperature may arise when a wind encounters the ambient gas resulting in a shock. This is fruther evidence that clump B1 may be a shocked clump.

7. The masses of the clumps listed in Table 3 are in the range 0.01 to 0.5 $M_\odot$. These masses are larger than the masses of clumps seen in other outflow sources. The H_2 number density of these clumps are roughly 5 times larger than those derived for the quiescent gas.

8. The total cloud mass within ~0.4 pc of GL 490 is about 410 $M_\odot$. Therefore, the clumps observed are dynamically insignificant. The outflow gas is not gravitationally bound to the parent cloud.

9. The data from Infrared absorption spectroscopy show that the quiescent cloud consists of two components, a cooler (T=24 °K) and a warmer (T=107 °K) component. The IR spectrum of GL 490 also shows the existence of an outflow component blueshifted by 13 km s^{-1} with respect to the quiescent gas.

10. The size of the region emitting in the J = 6 → 5 lines is estimated to be of the order of 11,000 to 13,000 AU.

11. The average number density for the gas within the warm region (based on the estimated size of the region) is found to be less than the number density implied from IR absorption data. This apparent discordance may be removed if the ^{13}CO absorption lines are not optically thin.

12.   The upper limit to the gas column density for the blueshifted component seen in absorption is found to be consistent with the column density obtained from the $J = 3 \rightarrow 2$ emission data. This consistency supports the scenario of a large-scale expanding shell of ambient gas accelerated by a wind. However, if the upper limit is close to the true column density, then the absorbing gas is probably very close to GL 490 in order to remain undetected against the emission lines.

13.   Our observations of the GL 490 outflow appear to be fairly consistent with the momentum-conserving shell model proposed by Shu et al.. However, more observations are needed in order to address some of the problems that arise in attempting to apply this model to the observations reported here.

References

Bachiller, R., Cernicharo, J., Martín-Pintado, J., Tafalla, M., and Lazareff, B. 1990, Astron. Astrophys., **231**, 174.

Bachiller, R., Martín-Pintado, J., and Fuente, A. 1991a, Astron. Astrophys., **243**, L21.

Bachiller, R., Martín-Pintado, J., and Planesas, P. 1991b, Astron. Astrophys., **251**, 639.

Bally, J., and Lada, C. J. 1983, Ap. J., **265**, 824.

Blitz, L., and Thaddeus, P. 1980, Ap. J., **241**, 676.

Campbell, B., Persson, S. E., and McGregor, P. J. 1986, Ap.J., **305**, 336.

Cantó, J., Rodríguez, L. F., and Anglada, G. 1987, Ap. J., **321**, 877.

Castor, J. I., McCray, R., Weaver, R. 1975, Ap. J. Lett., **200**, L107.

Cohen, M. 1975, M.N.R.A.S, **173**, 279.

Dickman, R. L. 1978. Ap. J. Suppl., **37**, 407.

Draine, B. T. 1983, Ap. J., **270**, 519.

Evans, N. J. II, Lada, E. A. 1991, in IAU Symposium No. 147: Fragmentation of Molecular Clouds and Star Formation, eds. Falgarone, E., Boulanger, F., and Duvert, G. (Kluwer Academic Publishers), p. 293.

Fuller, G. A., and Myers, P. C. 1987, in Processes in Interstellar Clouds, eds. Morfill, G. E., and Scholer, M. (Dordrecht: D.Reidel Publishing Company), p.137.

Gear, W. K., Gee, G., Robson, E. I., Ade, P. A. R., and Duncan, W. D. 1986, Mon. Not. R. astr. Soc., **219**, 835.

Genzel, R., and Stutzki, J. 1989, Ann. Rev. Astr. Ap., **27**, 41.

Grasdalen, G. L., Strom, K. M., and Strom, S. E. 1973, Ap.J. Lett., **184**, L53.

Harris, A. I. 1990, in Calibration of Ground-Based, Submillimeter Astronomical Data.

Harvey, P. M., Campbell, M. F., Hoffmann, W. F., Thronson, H. A. Jr. and Gatley, I. 1979, Ap.J., **229**, 990.

Hildebrand, R. H. 1983, Q. Jl R. astr. Soc., **24**, 267.

Ho, P. T. P., Townes, C. H. 1983, Ann. Rev. Astron. Astrophys., 21, 239.

Hodapp, K. W. 1984, Astron. Astrophys., 141, 255.

Kawabe, R., Ogawa, H., Fukui, Y., Takano, T., Fujimoto, Y., Sugitani, K., and Fujimoto, M. 1984, Ap. J. Lett., 282, L73.

Königl, A. 1982, Ap. J., 261, 115.

Lada, C. J. 1985a, in IAU Symposium No. 115: Star Forming Regions, eds. Peimbert, M., and Jugaka, J. (D. Reidel Publishing Company), p.1.

Lada, C. J. 1985b, Ann. Rev. Astron. Astrophys., 23, 267.

Lada, C. J., and Harvey, P. M. 1981,Ap. J., 245, 58.

Lada, C. J., and Wilking, B. A. 1984, Ap. J., 287, 610.

Langer, W. D., and Penzias, A. A. 1990, Ap.J., 357, 477.

Linke, R. A., and Goldsmith, P. F. 1980, Ap. J., 235, 437.

Martín-Pintado, J., Bachiller, R., and Fuente, A. 1992, Astron. Astrophys., 254, 315.

Mitchell, G. F., Allen, M., Beer, R., Dekany, R., Huntress, W., and Maillard, J. P., 1988, Astron. Astrophys., 201, L16.

Mitchell, G. F., Curry, C., Maillard, J.-P., and Allen, M. 1989, Ap.J., 341, 1020.

Mitchell, G. F., and Hasegawa, T. I. 1991a, Ap.J., 371, L33.

Mitchell, G. F., Hasegawa, T. I., and Schella J. 1992, Ap. J., 386, 604.

Mitchell, G. F., Maillard, J. P., and Hasegawa, T. I. 1991b, Ap. J., 371, 342.

Minchin, N. R., Hough, J. H., Burton, M. G. and Yamashita, T. 1991, M.N.R.A.S., 251, 522.

Morris, M., Palmer, P., Turner, B. E., and Zuckerman, B. 1974, Ap.J., 191, 349.

Mozurkewich, D., Schwartz, P. R., and Smith, H. A. 1986, Ap.J., 311, 371.

Myers, P. C., and Benson, P. J. 1983, Ap.J., 266, 309.

Nakamura, A., Kawabe, R., Kitamura, Y., Ishiguro, M., Mruata, Y., and Ohashi, N. 1991, Ap. J. Lett., 383, L81.

Plambeck, R. L., Snell, R. L., and Loren, R. B. 1983, Ap.J., 266, 321.

Pudritz, R. E., and Norman, C. A. 1983, Ap. J., **274**, 677.

Pudritz, R. E. 1985, Ap.J., **293**, 216.

Racine, r. 1968, A.J., **73**, 233.

Richer, J. S., Hills, R. E., and Padman, R. 1992, Mon. Not. R. astr. Soc., **254**, 525.

Schella, J. W. 1991, MSc. Thesis.

Scoville, N. Z., and Kwan, J. 1976, Ap.J., **206**, 718.

Shu, F. H., Ruden, S. P., Lada, C. J., and Lizano, S. 1991, Ap.J., **370**, L31.

Simon, M., Righini-Cohen, G., Felli, M., and Fischer, J. 1981a, Ap.J., **245**, 552

Simon, M., Righini-Cohen, G., Fischer, J., and Cassar, L. 1981b, Ap.J., **251**, 552.

Snell, R. L., Scoville, N. Z., Sanders, D. B., and Erickson, N. R. 1984, Ap.J., **284**, 176.

Spitzer, L., Jr. 1978, Physical Processes in the Interstellar Medium (New York: Wiley).

Steigman, G., Strittmatter, P. A., and Williams, R. E. 1975, Ap. J., **198**, 575.

Stutzki, J., Stacey, G. J., Genzel, R., Harris, A. I., Jaffe, D. T., and Lugten, J. B. 1988, **332**, 379.

Takano, T. 1986, Ap. J., **303**, 349.

Walker, C. K., Lada, C. J., Young, E. T., and Margulis, M. 1988, Ap.J., **332**, 335.

Walker, R. G., and Price, S. D. 1975. AFCRL Infrared Sky survey, Vol. 1. AFCRL-TR-75-0373. Hanscom AFB, MA: Air Force Geophysics Laboratory.

Wilking, B. A., and Lada, C. J. 1983, Ap. J., **274**, 698.

Zuckermann, B., Kuiper, T. B. H., Rodriguez, E. N. 1976, Ap. J. Lett., **209**, L137.

Curriculum Vitae

Name:	Siow-Wang Lee
Birthplace:	Singapore
Birthday:	November 9, 1964

Post-Secondary
Education:

B.Sc. (Mathematics), 1986
National University of Singapore,
Republic of Singapore.

M.Sc. (Astronomy), 1993
Saint Mary's University,
Halifax, N.S., Canada.

Awards:

Saint Mary's University Graduate Fellowship
1990-91 and 1991-92

The John Despard deBlois Scholarship
Saint Mary's University
1990-91

Experience:

Application Softwares Instructor
IBM Singapore Ltd., Republic of Singapore.
1988-89

Observatory Assistant
Burke-Gaffney Observatory, Saint Mary's University.
1989-90

Astronomy Research/Teaching Assistantships
Saint Mary's University
1989-92

Observing run at the 15-m James Clark Maxwell Telescope,
Mauna Kea, Hawaii, 1991.

Presented Paper: "A Multi-transition CO Study of the GL 490 Outflow"
Siow Wang Lee, George F. Mitchell and Henry Matthews,
presented at the 23rd Annual Meeting of the Canadian
Astronomical society - Halifax, Nova Scotia 1992.